Laser-cooling of Neutral Mercury and Laser-spectroscopy of the 1S0-3P0 optical clock transition

Michael Petersen

LABORATOIRE NATIONAL DE MÉTROLOGIE ET D'ESSAIS-SYSTEMES DE RÉFÉRENCE TEMPS-ESPACE

L'OBSERVATOIRE DE PARIS

Systèmes de Référence Temps-Espace

THÈSE DE DOCTORAT DE L'UNIVERSITÉ PIERRE ET MARIE CURIE, PARIS VI
spécialité : Physique quantique expérimentale

ÉCOLE DOCTORALE
Physique de la Région Parisienne, ED 107

présentée par
Michael Petersen

pour obtenir le titre de
Docteur de l'Université Pierre et Marie Curie, Paris VI

sujet de thèse :

Laser-cooling of Neutral Mercury and Laser-spectroscopy of the $^1S_0$-$^3P_0$ optical clock transition

Soutenue le 6 fevrier 2009 devant le jury composé de :

Mme.	Lucile Julien	Président du jury
M.	Jan W. Thomsen	Rapporteur
M.	Laurent Hilico	Rapporteur
M.	Patrick Gill	Examinateur
M.	Philip Tuckey	Directeur de thèse
M.	Sébastien Bize	Directeur de thèse

Acknowledgements

This thesis and the work that it describes has been done at the LNE-SYRTE (Laboratoire National de métrologie et d'Essais-SYstemes de Référence Temps-Espace) at the Observatoire de Paris in Paris, France, and I thank the SYRTE and the directors, Noël Dimarcq and Philip Tuckey for having me here and to Philip also for being willing to be my "directeur de thèse". My thanks go to the LNE-SYRTE and the LNE itself for financing my Ph.D. I thank the thesis jury, Jan W. Thomsen, Laurent Hilico, Lucile Julien and Patrick Gill, for taking the time to read my thesis and come to my Ph.D. defense.

My work here has been done in the mercury lattice clock group under the supervision of Sébastien Bize and my thanks goes to him for giving me the opportunity to work in this potentially high-profile and difficult experiment. I especially thank Seb for having the huge patience with me, my sometimes rather alternative way of doing things and especially my endless line of questions. I hope my work over the years in your laboratory has made up for some of those and the occasional blunders I made.

These have been some tough years for me due to the experiment being of a rather difficult nature and I therefore had trouble keeping the mood up. But in the end the results came and we could publish them before the end of my Ph.D. My thanks for helping me and the experiment through goes to many people, which are too many to be named.

A special thanks goes to the people in my group, who not only contributed to a large part of our achievements, but also helped me making it through when things were difficult and always lend me a hand if necessary. I thank Cipriana Mandache and Daniel Magalhães for always being supporting and nice to me even though I didn't always do the right thing and especially for showing me how to work in a laboratory. My thanks also goes to the postdocs Sam Dawkins and Radu Chicireanu for being equally

supporting, being good pals, helping out in my last half year down in the laboratory and especially for pushing through with the last and maybe most important piece of result while I used my time writing up my thesis. Even though she only joined the project a few months before me leaving it, I will not forget the projects next Ph.D. student Sinda Mejri, whom I have had a lot fun moments and weirdest discussions with, in our mutual office. I especially thank Sinda for always trying to keep me sane (and my mood up) and for always lending a hand with even the most ridiculous things, not to forget my "pot de soutenance". Over the years we have had the pleasure of having a number of "stagiaires" in our group: François, Ludivine, Dustin and Benjamin. You were a lot of fun to work with.

Another special thanks goes to mechanical workshop at l'Observatoire, Jean-Pierre, Laurent et Jean-Jacques, who of course took great care in making, among many other things, the main vacuum chamber of our vacuum assembly, but also always had the time to help me out with minor troubles of mechanical nature such as cutting a rod or finding an unusual type of screw. My thanks also goes to Annie Gérard for inspirational discussions about vacuum parts, glue and acetone and for letting me make a mess around the cleaning station for the vacuum parts.

I have had a lot of trouble getting into the subject of electronics and also due to the nature of my thesis I spent a bit of time doing electronics. I give a special thought and thanks to the electronic group at SYRTE, Michel Lours, Laurent Volodimer and José "Porto" Pinto Fernandes, for putting up with my often sour mood when doing electronics and for always helping out and for inspirational discussions regarding my often questionable electronics.

My thanks also go to all the co-students and post-docs who invited me out to a glass of whatever or just were good friends. Those were among many others Tanja Mehlstäubler for sneaking in and out of movies with me, François Impens for always inviting me to wine-related events including the many wine-tasting sessions here at l'Obs, Amandine Proia for being such a nice and smiling office neighbor, Jacques Millo for not only taking great part in designing our cavity but also always being there with a funny remark, Elizabeth "Liz" English for being a fun bowler, Olga Kozlova for being a great whiskey bowler, Thomas Lévêque for always having the time to come into my office and say hallo, Arnaud Lecallier for being such a nice guy and Quentin Bodart for being the "YES-Man". I also want to mention Clément Lacroute and Friedemann Reinhard as specially good friends who

have given me some good times outside work including some badminton. A special thanks goes to Thierry Botter who was always good in raising my spirits and relentlessly trying to beat a dane in badminton. Another special thank goes to François-Xavier "F-X" Esnault for being the coolest of friends, for being almost better than me at badminton every Sunday and for letting me explain how his miniaturized micro-wave clock should work on a weekly basis. I also want to thank the other Danish Ph.D. student here at SYRTE, Philip "fish" Westergaard, for being a great friend, of course for taking care of my "pot de soutenance" and for letting me invite myself to a selection of guitar, girls and gourmet food at the Danish student house in Cité U. on a number of occasions over the years.

Thanks go to the secretaries and especially Véronique Benayoun and Marine Pailler for helping me out numerous times. Thanks to the support of Pascal Blondé and especially Emmanuel Delor my computer always worked and the LateX used for writing this thesis worked most of the time.

My thanks goes to everyone else at the SYRTE for inspirational discussions, for moral support and for lending me a hand when necessary.

A Thank you goes to my family and friends not already mentioned for the often needed moral support.

Contents

Chapter 1

Introduction

1.1 The standard unit of time - the second

Throughout our history it has been important to have a standardized and precise way of measuring quantities such as weight and length especially for the purpose of trading. Within science and especially physics the definition of the unit of time - the second - has been of outmost importance. To begin with the definition was directly related to the earth's rotation around its own axis, but with the technological and scientific advances of the 20th century, this definition was found to be less stable than time realized by atomic clocks. It was therefore decided to relate the definition of the second to what we still suppose is a constant of nature - namely the frequency corresponding to the transition energy of a well-chosen atomic transition.

The definition of the second of the international system of units (SI)used today, was defined in 1967 as *the duration of 9 192 631 770 periods of the radiation corresponding to the transition between the two hyperfine levels of the ground state of the cesium-133 atom* [CGPM, 1969], [Terrien, 1968]. In terms of frequency this means that the $6^2S_{1/2}(F = 3 \rightarrow F = 4)$ transition of an unperturbed cesium-133 at rest has a transition frequency of 9.192631770 GHz.

Nowadays the second is by far the most accurately realized unit of the international system of units reaching a relative precision of a few parts in 10^{16} [Chapelet et al., 2007]. It is not surprising that other SI units are being related to the second, such as the unit of length (meter) [CGPM, 1984] [Giacomo, 1984].

This more accurate and above all much more stable definition for the

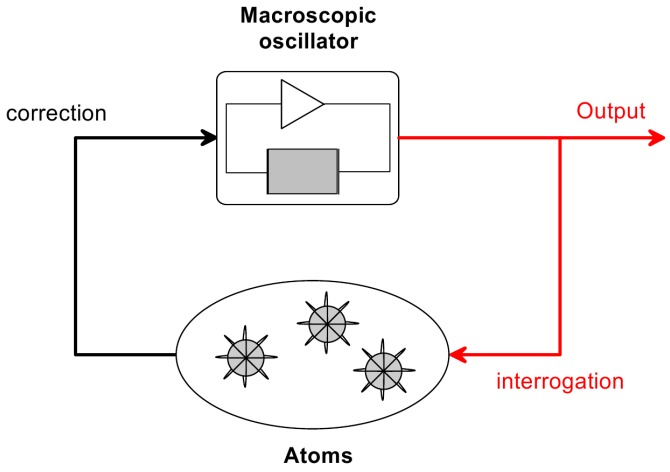

Figure 1.1: The basic principle of an atomic clock.

unit of time and the corresponding atomic frequency standard has made certain newer technologies possible such as the GPS navigation system. But it has especially made a difference for science and in particular physics allowing for baseline interferometric telescopes (such as the The European VLBI Network), testing of relativistic effects [Vessot et al., 1980] [Wolf et al., 2006] [Ashby et al., 2007], stability tests of fundamental constants to test unifying fundamental physics models [Blatt et al., 2008], [Rosenband et al., 2008] [Marion et al.,] not to forget the increased knowledge and understanding of atomic physics both in general and for specific atoms.

When realizing a primary frequency standard the problem is that generally cesium atoms are not at rest and their transition is perturbed by external magnetic and electrical fields not to mention gravitational, collisional and other effects. Methods have been developed to measure, remove or decrease those unwanted perturbations, so the accuracy of the second is now limited by certain properties of the cesium atom such as its sensitivity to thermal radiation, residual first order Doppler effect and the relatively low clock frequency. Advances in quantum optics, laser technology, laser-cooling and spectroscopical techniques within the last couple of decades have made it possible to use atomic transitions that have better properties. One day this might lead to a new improved definition of the second based on such a transition.

1.2 Atomic clocks

In general the device used to observe an atomic transition frequency with high precision for the purpose of delivering a signal with stable frequency is widely known as an atomic clock.[1] It is a method to obtain a coherent sinusoidal signal (RF signal or laser light) with the frequency of the (clock) transition or as is usually the case with a frequency with a well known offset from the clock transition frequency. To realize actual time a frequency counter needs to be added at the output to count cycles of the output signal. As shown in figure 1.1 the basic principle of an atomic clock is to use a signal from a macroscopic oscillator, typically a microwave oscillator, to interrogate carefully prepared atoms for the clock transition. A measurement of the atomic response can then be used to lock the oscillator to the clock transition so as to obtain the clock signal.

An atomic clock is characterized by the accuracy and the stability of its output frequency. The accuracy represents the uncertainty on the knowledge of the systematic effects that offset the clock frequency and the stability is a mean of characterizing temporal fluctuations of the frequency. An atomic clock's output frequency can be written

$$\nu(t) = \nu_0(1 + \epsilon + y(t)), \tag{1.2.1}$$

where ν_0 is the atomic transition frequency for the unperturbed atomic specimen used at rest. ϵ is the offset from the unperturbed clock frequency due to both intentional shifts done for practical reasons (for example done by an applied magnetic field to better measure the clock transition) or unintensional shifts from systematic effects due to environmental effects on the atoms. The latter can be due to, for example, magnetic fields (Zeeman shift), electrical fields (Stark shift), atomic interactions and motional and relativistic effects. It is the uncertainty of these shifts in comparison with the clock frequency that makes up the accuracy of a clock. The measurements of such shifts with the greatest possible accuracy have therefore been the subject of much scrutiny and is one of the key elements when working on the improvement of an atomic clock.

The time-dependent part of (1.2.1), $y(t)$, represents the output frequency fluctuations over time, that is, the stability of the output frequency. A consistent tool of expressing the stability of an atomic clock is by calculating

[1] From hereon I will refer to the transition frequency measured by an atomic clock as the 'clock frequency' and the corresponding transition as the 'clock transition'.

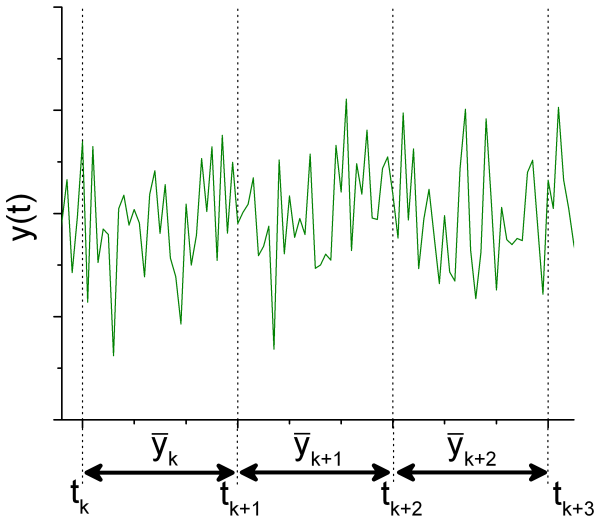

Figure 1.2: Calculating the Allan variance of a random function.

the Allan variance (see for example [Vanier and Audoin, 1989]) of the frequency which is a type of statistical measure well-defined for all types of noise. If τ is the time-interval for which the stability is to be characterized then for each successive intervals of duration τ the average value of the measured quantity $y(t)$ (fractional fluctuation frequency in our case) has to be calculated as shown in figure 1.2 :

$$\bar{y}_k = \frac{1}{\tau}\int_{t_k}^{t_{k+1}} y(t)\ \mathrm{d}t. \tag{1.2.2}$$

The Allan variance $\sigma_y^2(\tau)$ is then defined as half the regular variance of the difference between two successive averages:

$$\sigma_y^2(\tau) = \frac{1}{2}\langle(\bar{y}_{k+1} - \bar{y}_k)^2\rangle = \frac{1}{2}\lim_{n\to\infty}\left(\frac{1}{n}\sum_{k=1}^{n}(\bar{y}_{k+1} - \bar{y}_k)^2\right). \tag{1.2.3}$$

One advantage of using the Allan variance is that it has an easily recognized behavior as a function of the time interval τ for usual types of noise. For instance, a signal dominated by flicker frequency noise[2] has a constant Allan variance as function of τ. The short term frequency noise on atomic clocks

[2]Noise type where the spectral density has a $1/f$ dependency on the Fourier frequency.

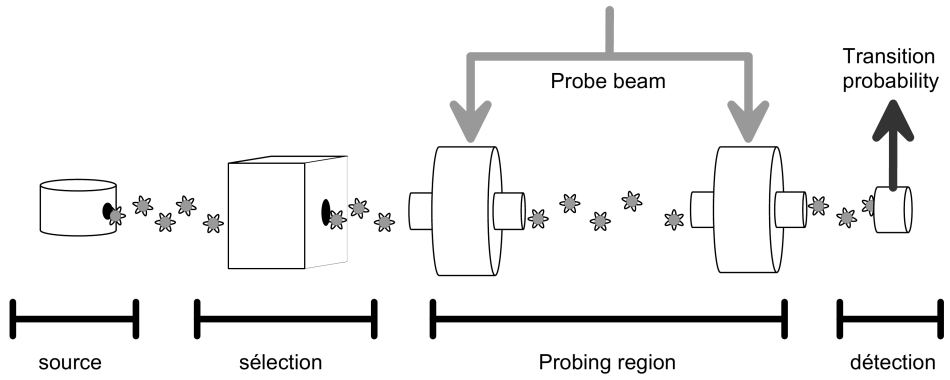

Figure 1.3: The typical (microwave) atomic beam clock using the Ramsey method of separated fields. Edited version of figure in [Bize, 2001].

is often dominated by white frequency noise[3] for a large range of Fourier frequencies. The Allan variance of a signal dominated by white frequency noise has a $1/\tau$ dependency and it can be shown that the frequency Allan deviation or fractional frequency instability, defined as the square-root of the Allan variance, of an atomic clock in general is (see for example [Fisk, 1997])

$$\sigma_y(\tau) = \frac{\eta \cdot \sigma_{\delta p}}{Q}\sqrt{\frac{T_c}{\tau}}, \tag{1.2.4}$$

with T_c being the measurement cycle time and η a constant close to unity depending on the method used for measuring the clock transition. $Q = \nu/\Delta\nu$ is called the atomic quality factor and signifies the inverse relative line width when measuring the clock transition. It is important to notice that compared to microwave frequencies at which the second is defined an optical frequency makes an improvement of five orders of magnitude on the quality factor. $\sigma_{\delta p}$ is the fluctuation of the measured transition probability and it indicates that by having for example a larger atomic sample to measure from we get smaller fluctuations and a better fractional frequency instability. Notice that this also is the case when having a narrower relative line width.

1.2.1 Atomic beam and fountain clocks

From equation (1.2.4) a clock's stability improves with increasing probe time since this improves the measured atomic quality factor. When it comes to

[3]Noise type where the spectral density is constant as a function of Fourier frequency.

the best atomic clocks, the probe time can be improved by either trapping the atoms in a field that has a well-known (or negligible) perturbation of the clock transition or by sending the atoms through a longer interaction region. The later can easier be done by the Ramsey method of separated fields (see for example [Ramsey, 1950], [Ramsey, 1985]), where the subjects under measurement (the atoms) only are probed in two small regions on each side of the probing region. Atomic beam clocks [Essen and Parry, 1957][4] use this method by sending a beam of atoms through a clock transition $\pi/2$-pulse[5], then through an interaction free region before being subjected to a second $\pi/2$-pulse coherent with the first one (figure 1.3). While an atom is travelling between the two pulses it is effectively under measurement and a longer interaction time is obtained without increasing the width of the interaction regions themselves. For optical clock transitions it is necessary to use three or four interaction regions due to the increased momentum transfer from a photon effectively separating the atomic wave of the two atomic states, but the basic principle is the same.

It is common to have beam clocks based on the Cs atom such as [Makdissi and de Clercq, 2001] at SYRTE in Paris, France, [Bauch et al., 1998] at the PTB in Braunschweig, Germany and [Shirley et al., 2001] at the NIST in Boulder, Colorado, USA which have shown accuracies better than $7 \cdot 10^{-15}$ and instabilities down to $3.5 \cdot 10^{-13}$ at 1 s with a distance between interaction zones of about 1 m and an (average) interaction time of a few ms. Other atomic and molecular species have been used in atomic beam clocks such as Ag [Hahn and Radecki, 1987] and methane (CH_4) [Kramer et al., 1988] with two interaction zones and Ca [Morinaga et al., 1989] and SF_6 [Bordé et al., 1984] [Amy-Klein et al., 2005] using four interaction zones due to their optical clock transitions.

Today most primary standard atomic clocks are fountain clocks [Kasevich et al., 1989] [Clairon et al., 1991] based on the same principle as the atomic beam clocks with the atoms being laser-cooled to extend the interaction time. Since gravitational acceleration and thermal expansion of an

[4] As a side note it was this atomic beam clock that was used to relate the clock transition frequency of ^{133}Cs to the ephemeris second based on measurements of the orbital movement of the moon around the earth [Markowitz et al., 1958].

[5] A microwave field with width and power such that on average $\Omega_R \tau = \pi/2$ where Ω_R is the Rabi frequency and τ the time an atom spends in the light beam. To avoid atomic momentum change this is done by retro-reflected beams of the lowest order standing wave mode in a cavity.

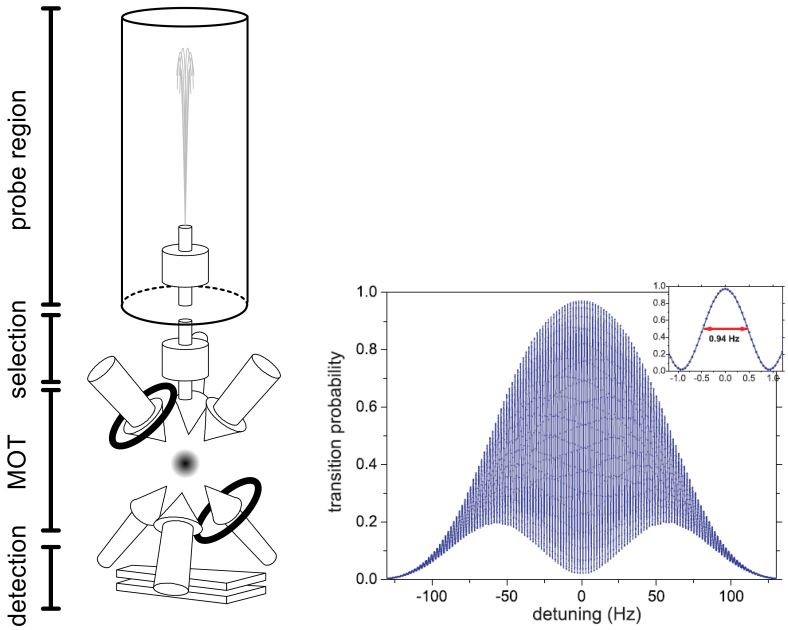

(a) (b)

Figure 1.4: (a) The typical (microwave) atomic fountain clock. Edited version of figure in [Bize, 2001]. (b) Ramsey fringes obtained through the Ramsey method of separated fields. This is the results from a Cs fountain [Bize et al., 2005].

atomic beam can limit the distance or rather the interaction time between the interaction zones, the atoms in a fountain clock are first prepared in a magneto-optical trap (MOT) or optical molasses which cools down the atoms ($\sim \mu$K) and decreases thermal expansion. The ball of trapped atoms is released and shot up vertically through a single interaction region which then is used a second time when the atom falls down again, effectively using the Ramsey method of separated fields with a single field (see figure 1.4(a)). The atomic state is then detected before reaching the bottom of the chamber. The key point of this method is to have atoms that expand much less and travel slower through the probing region while not falling out of the probing region due to gravity.

These types of clocks remains some of the best and most common primary standard clocks in the world and the FO1 and FO2 fountain at SYRTE have achieved accuracies better than $4 \cdot 10^{-16}$ and instabilities at 1 s as low as 10^{-14} using Cs [Chapelet et al., 2007]. Other working Cs fountains are found at NIST in Boulder, Colorado, USA [Jefferts et al., 2007], PTB

in Braunschweig, Germany [Bauch, 2005], NPL in London, England [Szymaniec et al., 2005], INRIM in Torino, Italy [Levi et al., 2004] not to forget the continuous fountain at METAS in Bern Switzerland [Guéna et al., 2007]. The FO2 fountain clock at SYRTE is a double fountain that also uses Rb.

The best fountain clocks are typically limited by imperfections in the interaction region microwave fields (phase gradient in the microwave resonator), the background blackbody radiation shift at room temperature and microwave leaks.

1.2.2 Ion clocks

As mentioned at the beginning of the previous subchapter an atomic clock's probe time can also be increased by trapping the atoms in a field of a kind that does a negligible disturbance of the clock transition. One of the most successful types of clocks are the ion clocks dating back to the 70's using microwave clock transitions and the 80's using optical clock transitions. But only with the invention of the femtosecond laser [Udem et al., 1999](more on this in chapter 5) at the end of the 90's was it practical to make use of an optical clock, making ion clocks comparable to fountain clocks in terms of applications.

In ion clocks a single ion is trapped in a time varying electric field with a zero field center before it being laser-cooled. By making the ion cold enough the ion will effectively not be subjected to the trapping field's Stark shift. If the ion is confined in all directions to a region much smaller than the clock transition wavelength (the Lamb-Dicke regime [Dicke, 1953]) motional effects such as the first order Doppler effect and the recoil shift are suppressed.

The clock transition which typically has an experimental line width of the order of the Hz is usually probed by the method of quantum jumps [Dehmelt, 1982] - a method where atoms or ions are excited on the clock transition and the consequently decrease in ground state population is measured by the fluorescence of a strong ground state transition. In the case of a single ion, there is no fluorescence at all when the ion is in the excited clock state. Some ions such as Al^+ are difficult to laser-cool directly and are sympathetically laser-cooled by laser-cooling a second ion of a different species in the same trap. Due to the Coulomb interaction between the two ions this leads to cooling of the clock ion. In this case the clock transition

is probed by the method of quantum logic spectroscopy [Schmidt et al., 2005], which uses a quantum gate like the one used in quantum information processing to link an easier monitored state in the second ion to the clock ion state.

Ion clocks made at the NIST laboratories in Boulder, Colorado, USA based on single Hg^+ and Al^+ ions have reached accuracies of a few times 10^{-17} and relative instabilities of better than $4 \cdot 10^{-15}$ at 1 s [Rosenband et al., 2008]. The Hg^+ clock's performance would normally be limited by room temperature blackbody radiation but due to a surrounding vacuum chamber being cryogenic cooled by liquid helium this is not an issue. Instead it is the fourth order electric and magnetic shifts due to the trapping field that limits the clock accuracy. The Al^+ clock, which is much less sensitive to blackbody radiation, but has to be sympathetically laser-cooled by a Be^+ ion, is limited by the ion's micro-motion in the trap (motion due to stray fields) and to lesser extend secular motion (harmonic motion in the trap) and blackbody radiation.

A number of other different species of ions are being used in ion clocks such as Yb^+ at the PTB in Braunschweig, Germany [Schneider et al., 2005] and at the NPL in London, England [Hosaka et al., 2005] (on a narrower octopole clock transition), Sr^+ also at NPL [Margolis et al., 2004] and In^+ at the Max-Planck-Institut für Quantenoptik in München, Germany [von Zanthier et al., 2000].

Nonetheless the impressive performances shown by (single) ion clocks, they are fundamentally limited in stability by the quantum limited signal-to-noise ratio due to the measurement on just one particle.

1.2.3 Lattice clocks

Another possibility is to laser-cool and trap a much larger number of neutral atoms. The absence of the strong Coulomb interaction between the atoms makes it possible to use more than a single atom although interatomic collisions might pose a problem at high densities. Most one- and two-electron atoms have a ground-state transition suitable for laser-cooling. The challenge is to trap a large number of neutral particles preferably in the aforementioned Lamb-Dicke regime to suppress first order motional effects with a field that does not perturb the clock transition.

In 2001 H. Katori proposed the idea of lattice clocks in which laser-cooled

neutral atoms are trapped in an off-resonant red-detuned dipole lattice trap at a wavelength - nowadays called *the magic wavelength* - where the Stark shift of the two clock state energies are equal so to cancel out the AC Stark shift of the clock transition [Katori, 2002] [Katori et al., 2003]. The simplest version of the dipole trap is a 1D-lattice obtained by having a focused standing wave. Around the focus point there are interference fringes (effectively potential wells) in which, if the light intensity is high enough, it is possible to trap a number of atoms in each well in the Lamb-Dicke regime. To avoid quantum tunneling between two dipole potential wells which would lead to line broadening and frequency shifts it is beneficial to have the row of lattice traps along vertical so to lift degeneracy between adjacent wells with the gravitational potential [Lemonde and Wolf, 2005].

Lattice clocks are a promising candidate for being the next generation of atomic clocks that could attain the same level of accuracy as the ion clocks with a much better stability. First order motional effects can mostly be removed, second order motional effects can be subdued by cooling atoms down in the lattice trap and collision shifts can be avoided by using a 3D-lattice in which each well does not contain more than one atom. The lattice clocks can reach a possible relative instability level of 10^{-18} with an interrogation time of just one second if the standard quantum limit is achieved. This is only possible if strong improvements are made on laser stabilization. It is also noticeable that neutral alkaline-earth atomic isotopes have a $J = 0 \rightarrow J = 0$ optical transition (J being the electronic momentum) with a sub-Hertz line width, which is a well suited clock transition for reaching a relative uncertainty of less than 10^{-17}. This transition is weakly allowed in the hyperfine interaction due to a non-zero nuclear spin. Alternatively it is possible to quench the clock transition for isotopes with no nuclear spin with an external magnetic field [Taichenachev et al., 2006].

So far experimental work on lattice clocks has been undertaken on three different alkaline-earth atomic species Sr, Yb and lately Hg. Our project is one of the first lattice clocks based on neutral mercury (more on this in the next subchapter).

Atomic lattice clocks based on Sr were the first lattice clocks to be proposed and worked on experimentally and are now the subject of work at SYRTE in Paris, France [Baillard et al., 2007], JILA in Boulder, Colorado, USA [Ludlow et al., 2008], University of Tokyo in Tokyo, Japan [Takamoto et al., 2005], PTB in Braunschweig, Germany [Riehle et al., 2008], NPL in

London, England [Curtis et al., 2008], and at LENS in Firenze, Italy [Poli et al., 2007].

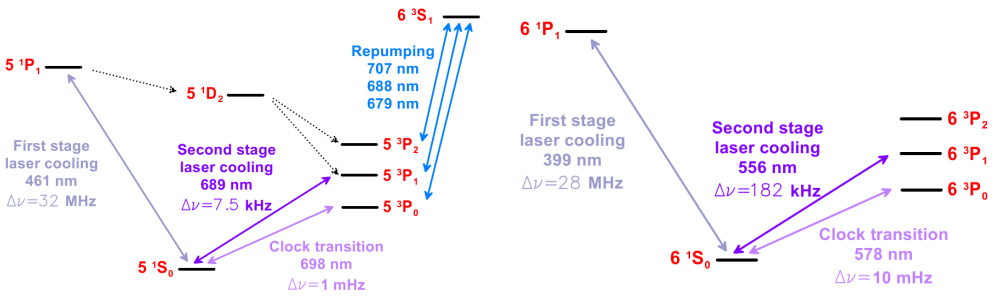

Figure 1.5: (a) The energy levels for strontium used in the lattice clock. Decay from the $^1P_1$ state towards the $^1D_2$ state poses problems with the lifetime of the first stage MOT. (b) The energy levels of ytterbium used for the lattice clock so far.

To efficiently laser cool strontium it is necessary to use a double cooling sequence in which first the strongly allowed transition between the $^1S_0$ ground state and $^1P_1$ at 461 nm is used to trap and cool down the atoms into the mK range and then a second cooling stage is used on the rather narrow transition at 689 nm from the ground state towards the $^3P_1$ state to further cool down the atoms into the μK range (see figure 1.5(a)). For the fermion ^{87}Sr the 698 nm transition between the ground state and $^3P_0$ has a line width of approximately 1 mHz and is used as the clock transition. The clock transition is only allowed for the single fermion isotope with only a 7 % natural abundance. By large the most common isotope is the boson ^{88}Sr with an abundance of almost 83 % which can only be used for a clock by quenching the clock transition with a static magnetic field. Notice that in this case the clock transition is not sensitive to the magnetic field to first order and there is no splitting of the clock states into magnetic substates. A magic wavelength of Sr has been experimentally determined at 813.43 nm [Takamoto et al., 2005], [Ludlow et al., 2006], [Brusch et al., 2006].

The group at JILA has obtained a relative uncertainty of $1.5 \cdot 10^{-16}$ (60 mHz in absolute frequency) and a relative instability at 1 second of about $3 \cdot 10^{-15}$ on a sample of little more than 10^4 ^{87}Sr atoms at a temperature of a few μK trapped in a vertical lattice trap with a peak intensity of 3 kW/cm^2. The atoms are transferred from MOT containing more than 10^5

atoms at 2.5 μK. The clock transition is probed by a diode laser locked to a 250000 finesse ultra-stable cavity. The probe light had a line width of less than 0.5 Hz and a relative stability of around 10^{-15} at 1 second [Ludlow et al., 2007]. The spectroscopic measurement of the clock transition is done via the method of quantum jumps known from the ion clocks although with a twist [Ludlow et al., 2006]. The twist is that the clock transition is probed initially but just afterwards atoms in $^3P_0$ are pumped into $^3S_1$ from which some of them will naturally decay into the meta-stable state $^3P_2$. This sequence is repeated a number of times before the decreasing number of atoms in the ground state is probed by detection of the fluorescence of the strong $^1S_0 -^1 P_1$ transition. By adding a static 20 μT magnetic field it was possible to measure the clock transition free of the first order Zeeman shift (magnetic field shift) by averaging measurements of the transitions on the two extreme magnetic substates. So far, the clock performance is limited by uncertainty in the room temperature blackbody radiation shift and, to lesser extent, the collisional shift. Their clock stability is predominantly limited by laser instabilities.

The group at SYRTE has managed to make an operational lattice clock with both the fermion isotope ^{87}Sr [Baillard et al., 2008] and the boson ^{88}Sr [Baillard et al., 2007]. Here the atoms are also initially cooled in a MOT on the transition between ground state and $^1P_1$ but as opposed to the JILA group the atoms are then pumped into the metastable states $^3P_0$ and $^3P_2$ (through transitions towards $^3P_1$ and then $^3S_1$) to accumulate atoms into the lattice dipole trap. After pumping the atoms back into the ground state the transition between ground state and $^3P_1$ is used to further cool the atoms to reach temperatures near 1 μK and thereby ending up with most of the atoms in the ground state of the dipole trap. For spectroscopy of the clock transition a diode laser locked to a 25000 finesse cavity is used to probe the clock transition. A 0.1 mT static magnetic field is used to split up the magnetic substates to make measurements of the clock transition free of the first order Zeeman effect. Also here the quantum jump method is used by first probing the clock transition and then measure the number of atoms still in the ground state by the fluorescence of the strong transition towards $^1P_1$ when subjected to the cooling laser light. Using ^{87}Sr this clock has shown a relative uncertainty of $2.6 \cdot 10^{-15}$ and a stability of $6 \cdot 10^{-14}$ at 1 second. For dealing with the boson ^{88}Sr an additional 1.7 mT static magnetic field was added during the probe phase. Using the boson the

Clock type	Uncertainty	Instability at 1 s	Reference
Cs jet (9.2 GHz)	$7 \cdot 10^{-15}$	$5 \cdot 10^{-12}$	[Bauch et al., 1998]
Cs jet (9.2 GHz)	$6.4 \cdot 10^{-15}$	$3.5 \cdot 10^{-13}$	[Makdissi and de Clercq, 2001]
Cs fountain (9.2 GHz)	$5 \cdot 10^{-16}$	$3 \cdot 10^{-13}$	[Jefferts et al., 2007]
Cs fountain (9.2 GHz)	$4 \cdot 10^{-16}$	$1.6 \cdot 10^{-14}$	[Chapelet et al., 2007]
Trapped Al^+ ion (267 nm)	$2.3 \cdot 10^{-17}$	$3.9 \cdot 10^{-15}$	[Rosenband et al., 2008]
Trapped Hg^+ ion (282 nm)	$1.9 \cdot 10^{-17}$	$3.9 \cdot 10^{-15}$	[Rosenband et al., 2008]
Sr lattice (698 nm)	$1.5 \cdot 10^{-16}$	$3 \cdot 10^{-15}$	[Ludlow et al., 2008]
Yb lattice (578 nm)	$1.5 \cdot 10^{-15}$	$5.5 \cdot 10^{-15}$	[Poli et al., 2008]

Table 1.1: The present (October, 2008) top performances of different types of atomic clocks as have been reported. The clock transition wavelength is reported in parenthesis next to the clock type. The uncertainty and the instability are both in fraction of the clock frequency.

clock showed a fractional uncertainty of $7 \cdot 10^{-14}$ limited by the collisional shift. The SYRTE ^{87}Sr clock measured against the FO2 fountain clock has demonstrated the best stability between an optical and a microwave clock [Baillard et al., 2008].

Work on Yb in a lattice clock is being done by at NIST in Boulder, Colorado, USA [Poli et al., 2008], NMIJ/AIST in Tokyo, Japan [Yasuda et al., 2007], KRISS in Daejeon, Korea [Park and Yoon, 2003] and at INRIM in Torino, Italy [Calonico et al., 2008].

Ytterbium has seven natural abundant isotopes with two of them being fermions (^{171}Yb and ^{173}Yb) both with an abundance of about 15 %. The most abundant boson isotope is ^{174}Yb with a 32 % abundance. The atomic structure of Yb is very similar to the one of Sr (as can be seen from figure 1.5). Yb also requires double cooling stages but the state $^1D_2$ has a higher energy than $^1P_1$ and does not pose a problem in relation to natural decay from $^1P_1$ as it can do for Sr. A magic wavelength of Yb has been measured at 759.35 nm [Barber et al., 2006].

The only report so far of a working Yb lattice clock is from the NIST group achieving a fractional uncertainty of $1.5 \cdot 10^{-15}$ and a fractional instability of $5.5 \cdot 10^{-15}$ at 1 second. Just as for the lattice clock based on Sr, atoms are laser cooled through two stages on the transitions $^1S_0 - ^1P_1$ and $^1S_0 - ^3P_1$ (see figure 1.5(b)). This group has chosen to work primarily

on the boson ^{174}Yb for which the last cooling stage leaves about 10^5 atoms at an approximative temperature of 40 μK and 10^4 atoms after loading the dipole trap at the magic wavelength. Again since the proposed clock transition is forbidden for the bosons due to a zero nuclear spin an additional static magnetic field of about 1 mT was added during the probing of the clock transition. The probe laser is a frequency sum generation of a YAG laser and a fiber laser stabilized on a vertical high stability cavity. Detection of the clock transition was here also done by the aforementioned method of quantum jumps. So far it is the collisional shift that limits the uncertainty [Poli et al., 2008].

Table 1.1 gives an overview of the best performance so far of different types of atomic clocks. Optical ion clocks have recently surpassed microwave fountain clocks while optical lattice clocks still have a way to go. The lattice clock scheme is still quite recent compared with the several decade long effort on trapped ion clocks.

Mg is another atomic species that could be used in an atomic lattice clock due to a similar electronic structure [Hansen et al., 2008] [Friebe et al., 2008].

1.3 The neutral mercury lattice clock

In 2004 it was independently proposed at Tokyo University [Katori et al., 2004] and at SYRTE in Paris to use mercury in an optical lattice clock, mostly due to its high atomic number making it rather sensitive to relativistic corrections, and due to the mercury clock transition's low sensitivity to black-body radiation. Neutral mercury has an alkaline-earth like electronic structure just as Sr and Yb (see figure 1.6) and it has a magic wavelength at a practicable wavelength making it a candidate for an optical lattice clock. In comparison with Sr and Yb neutral mercury has a transition better adapted for single-stage laser-cooling and a clock transition sensitivity to room-temperature black-body radiation more than ten times lower (see chapter 2 for more details on the advantages and disadvantages of using neutral mercury). The challenges of using mercury are the deep-UV lasers necessary for both laser-cooling and for probing the clock transition not to forget the expected magic wavelength in the near-UV. Therefore until recently neutral mercury had not been considered within the field of laser cooling and quantum optics and neutral mercury was only laser-cooled and

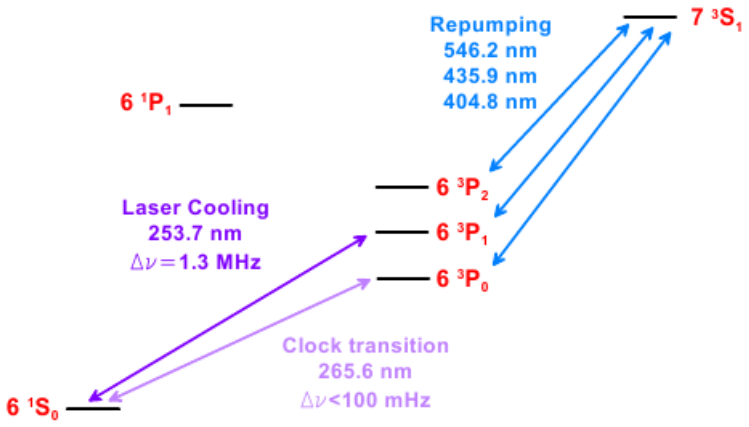

Figure 1.6: The lowest energy levels of neutral mercury.

trapped in a vapour cell MOT in late 2007 [Hachisu et al., 2008] and in a MOT based on 2D-MOT pre-selection in early 2008 [Petersen et al., 2008].

We are working on developing such an optical lattice clock based on neutral mercury. With a clock transition around 266 nm we have developed a clock laser at the quadruple wavelength locked to an ultra-stable high-finesse cavity as the clock macroscopic oscillator. A slave laser is injection locked to this clock light as a mean to amplify and then frequency doubled twice through intra-cavity non-linear crystals before being used for probing the clock transition.

In order to have a good lifetime of the trapped atomic mercury we opted for a solution with a double vacuum chamber as to be able to create good vacuum conditions in one of the chambers. The first vacuum chamber with a source of mercury creating a background vapour and a two-dimensional version of a magneto-optical trap (2D-MOT) for selecting slow atoms of a single isotope [Dieckmann et al., 1998]. The second chamber being the main chamber is where the atoms are first laser-cooled and trapped in a 3D MOT to decrease temperature and increase density before they ultimately will be transferred to a magic wavelength dipole trap and then probed.

For cooling we have developed a high power at 254 nm laser source based on a disc-laser at the quadruple 1015 nm, which light then is frequency doubled twice in yet two other intra-cavity non-linear crystals. This light is stabilized near the cooling transition by saturation spectroscopy through a room-temperature vapour cell. It is the plan to obtain the lattice trap field

at the magic wavelength ($\sim$ 360 nm) by frequency doubling a Ti-Sa laser.

This thesis reports on the first three years of this project which began in 2005. The key achievements has been (as one of the first in the world) to laser-cool and trap neutral mercury in a MOT and to do the first laser spectroscopy of the neutral mercury clock transition.

The next chapter, chapter 2, is a general presentation of the relevant properties of neutral mercury in the context of a lattice clock and it details the advantages and disadvantages of using (neutral) mercury in an optical lattice clock.

Chapter 3 contains the information about how we obtained and stabilized the cooling light while chapter 4 is about the vacuum chamber, computer simulation of mercury atoms in the 2D-MOT and how the MOT was built. Chapter 4 also reports on the measurements of the main features of the MOT.

Chapter 5 deals with the generation of the probe light: namely the ultra-stable cavity and sources of noise, fiber-noise cancellation systems, slave laser and the two frequency doubling systems.

Chapter 6 describes the first laser spectroscopy of the Doppler-free clock transition of mercury in free fall and the link to a microwave reference using a femto-second laser system.

Chapter 2

The potential of using neutral mercury in an optical lattice clock

This chapter gives a detailed overview of the known advantages and disadvantages of choosing neutral mercury for an atomic clock. I will start out with some general properties, then move on to the spectroscopical details of the lower energy levels of neutral mercury. I will then deal with the proposed clock transitions expected sensitivity to magnetic fields and laser light. At last I will look at a magic wavelength of mercury in the optical domain.

2.1 General Properties of Mercury

Mercury has atomic number 80 and average atomic weight of 200.59 atomic mass units. This makes it one of the heaviest atomic species ever laser-cooled.

Mercury has 7 natural isotopes, 5 bosons and 2 fermions (see table 2.1) where the least abundant ^{196}Hg isotope is just too scarce to be considered in the first place. It is an advantage to have several abundant isotopes to work with. If one isotope proves to have a high collision shift, one can consider using others, as it is often the case that the collision shift is very different between isotopes. Due to the Pauli exclusion principle cold fermions in the same quantum state are less prone to collide while a boson clock transition can be quenched [Taichenachev et al., 2006] making magnetic shifts easier

Isotope	Atomic mass	Abundance	Nuclear spin
196 (boson)	195.965807	0.15 %	0
198 (boson)	197.966743	9.97 %	0
199 (fermion)	198.968254	16.87 %	1/2
200 (boson)	199.968300	23.10 %	0
201 (fermion)	200.970277	13.18 %	3/2
202 (boson)	201.970617	29.86 %	0
204 (boson)	203.973467	6.87 %	0

Table 2.1: The natural isotopes of mercury [Lide, 1995].

to control. It also becomes important for comparing (boson) collision shifts in the final dipole trap.

The bosons all have zero nuclear spin while the fermions have a rather low nuclear spin of 1/2 and 3/2 (in units of Planck's constant) which simplifies the clock transition spectrum and quantum optical operations. The proposed clock transition is only allowed for fermions due to their non-zero nuclear spin but as just mentioned it is possible to mimic the hyperfine interaction from a non-zero nuclear spin with a magnetic field (quenching).

A remarkable property of mercury is that its boiling point is at 356.73° C (at 1013.25 Pa) while its melting point is at -38.83° C making it liquid at room temperature. At room temperature (300 K) the vapour pressure of mercury is 0.3 Pa. Figure 2.1 shows that the vapour pressure of mercury is a factor of ∼1000 higher than the corresponding vapour pressure of rubidium and cesium often used in cold atom experiments. Sr and Yb need to be heated to 300-400° C to have any kind of decent vapour pressure.

First and foremost it is therefore not necessary to heat up a source of mercury to several hundred degrees in an oven to release atoms into a vacuum chamber, which can be a rather troublesome source of black-body radiation. Instead a simple way to release the mercury into the vacuum chamber in a controllable way is to use a Peltier element to cool down a drop of mercury as described in further details in subchapter 4.1. The higher vapour pressure also means that a small room temperature vapour cell for saturated absorption is sufficient for frequency locking a laser (more on this

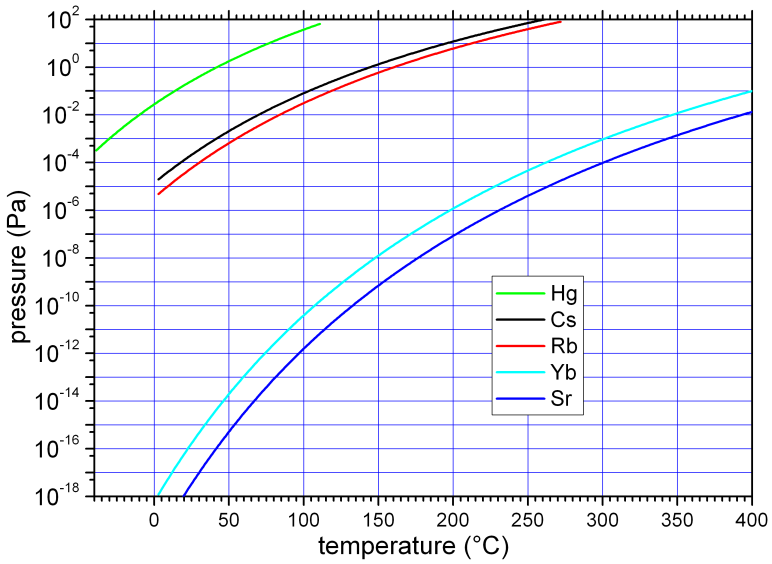

Figure 2.1: The vapour pressure of liquid mercury compared with liquid rubidium and cesium and solid ytterbium and strontium. The graphs are extrapolated from data in [Alcock, 1995].

in subchapter 3.2).

2.2 The mercury spectrum

The electronic structure of (neutral) mercury can in its whole be written $1s^2 2s^2 2p^6 3s^2 3p^6 3d^{10} 4s^2 4p^6 4d^{10} 4f^{14} 5s^2 5p^6 5d^{10} 6s^2$ [Lide, 1995]. This means its outer (6th) shell contains two electrons and that all the inner electron shells are closed. Therefore mercury has the electronic structure of an alkaline-earth having a similar energy level structure as for example magnesium, strontium or ytterbium. This means that the lowest energy levels are the ${}^1S_0$ ground state, a triplet ${}^3P$ state and a singlet ${}^1P$ (figure 1.6 and 2.2). As is the case for Sr (but not for Hg or Yb) the ${}^1D_2$ state can have an energy lower than the ${}^1P$ state.

The ${}^1S_0 \rightarrow {}^3P_1$ intercombination line is a relatively strong transition with a 1.27 MHz natural linewidth and a 125 ns lifetime at a vacuum wavelength of 253.724 nm. The corresponding Doppler temperature $T_D = \hbar\gamma/2k_B$ is 30.6 μK and its recoil temperature $T_R = \hbar^2 k^2/mk_B$ is 1.5 μK. Apart from the challenging wavelength it is a good candidate for cooling transition. The saturation intensity

$$I_s = \frac{\pi hc\gamma}{3\lambda^3} \tag{2.2.1}$$

for the transition is 10.2 mW/cm^2, a value which makes it relatively practicable to obtain saturated absorption with less than 1 mW of power.

The transition from the ground state to the ${}^1P_1$ state is often used as a cooling transition in other alkaline-earth atomic species (for example Sr and Yb). But for mercury this transition has a large 119 MHz natural linewidth and a Doppler temperature of 2.8 mK making it a rather ineffective cooling transition. The 185 nm transition wavelength is also even less practical than the aforementioned 254 nm.

In the fine structure model of the atom the ${}^1S_0 \rightarrow {}^3P_0$ transition is strictly forbidden.[1] But by adding the hyperfine interaction between the

[1]For any kind of multipole transition of order κ with angular momentum $j \rightarrow j'$ it is only allowed if $|j - \kappa| \leq j' \leq j + \kappa$ [Sobelman, 1992]. Since the lowest order transition is with $\kappa = 1$ (dipole transitions) this effectively forbids $j = 0 \mapsto j' = 0$ transitions like the ${}^1S_0 \rightarrow {}^3P_0$ transition within the fine structure model. According to [Santra et al., 2004] for bosons of alkaline-earth like atoms like Sr, Ca and Mg, where the fine structure model is enough to correctly describe the level structure due to their vanishing nuclear spin, this transition is allowed by a two-photon (E1M1) transition although with a lifetime of

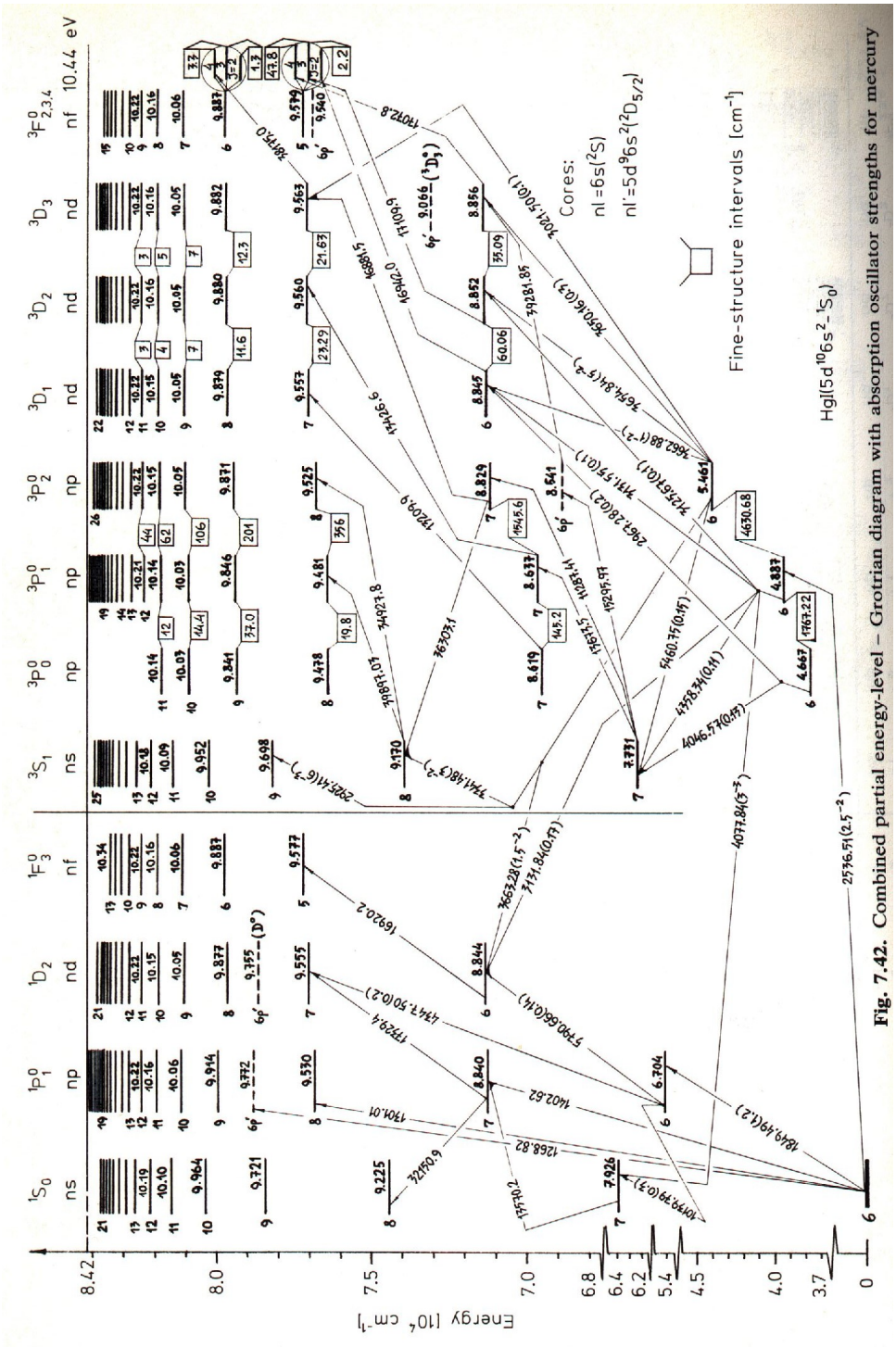

Fig. 7.42. Combined partial energy-level – Grotrian diagram with absorption oscillator strengths for mercury

Figure 2.2: Grotrian diagram for mercury with transition wavelengths in Å. [Radzig and Smirnov, 1985]

magnetic field of a non-zero nuclear spin and the electrons this transition becomes weakly allowed. It is possible from experimental measurements on the stronger transitions in mercury to calculate the decay time of the ${}^1S_0 \rightarrow {}^3P_0$ and thereby its natural linewidth, but this first requires more knowledge about the fine-structure of mercury's P-states.

2.2.1 The P-states in the fine structure model

The (simplest) fine structure model hamiltonian includes[2]

$$H_{fs} = H_c + H_r + H_{LS}. \tag{2.2.2}$$

H_c is the central field hamiltonian describing the average electric field from the nucleus and the electronic cloud and H_r is the repulsion term which describes the repulsion between electrons not covered by the average central field H_c. Since all the inner electrons are in closed (full) shells we can assume that the repulsion term only needs to include the repulsion between the two outer electrons. The important term in the fine structure model is

$$H_{LS} = \xi(\mathbf{r}_1)\mathbf{l}_1 \cdot \mathbf{s}_1 + \xi(\mathbf{r}_2)\mathbf{l}_2 \cdot \mathbf{s}_2 + \eta(\mathbf{r}_1 - \mathbf{r}_2)(\mathbf{l}_1 \cdot \mathbf{s}_2 + \mathbf{l}_2 \cdot \mathbf{s}_1) \tag{2.2.3}$$

that describes the spin-orbit coupling, that is the interaction between an electron's spin and orbital momentum.[3] Again the interaction only includes the two outer electrons.

In the LS-coupling scheme where the spin-orbit term is negligible ($H_r \gg H_{LS}$) both the angular momentum $\mathbf{L}^2$, the spin $\mathbf{S}^2$ and the total angular momentum $\mathbf{J}^2$ are good quantum numbers and we can write the energy eigen states in the classic Russell-Saunders notation $|^{2S+1}L_J\rangle$ (I will call those 'pure LS states') and then treat the spin-orbit term as a perturbation of those. Without the perturbation intercombination transitions ($\Delta S \neq 0$) are not allowed, but the perturbation from the spin-orbit term can mix the pure states such that they are. The other extreme case ($H_r \ll H_{LS}$) is the jj-coupling scheme where not only $\mathbf{J}^2$ is a well-defined property but also the single electrons total angular momentum (j_1, j_2) such that the energy eigen

at least several 1000 years.

[2]See for example [Bransden and Joachain, 1983]. This is what is used by [Bigeon, 1967] in their fine structure and hyperfine structure calculations.

[3]Most text books such as [Bransden and Joachain, 1983] do not include the last term in 2.2.3, but it is included in [Bigeon, 1967] while [Condon and Shortley, 1935] treat it as an afterthought.

states can be written $|j_1, j_2; J\rangle$. Mercury is an intermediate case with a far from negligible spin-orbit coupling, as is indicated by the rather strong ${}^1S_0 \rightarrow {}^3P_1$ intercombination transition, but it is helpful to look at how the pure LS- or jj-states mixes. In most literature the inter-configuration mixing of states, that is the $\mathbf{L}$ (and n) mixing of states, is ignored,[4] so we can consider both the four pure LS-states ($|{}^1P_1\rangle$, $|{}^3P_0\rangle$, $|{}^3P_1\rangle$, $|{}^3P_2\rangle$) and the four pure jj-coupling states $|1/2, 1/2; 0\rangle$, $|1/2, 1/2; 1\rangle$, $|1/2, 3/2; 1\rangle$, $|1/2, 3/2; 2\rangle$ as a basis-set.

While $\mathbf{J}^2$ commutes with the spin-orbit term in the Hamiltonian, $\mathbf{S}^2$ does not. This means that the spin-orbit term mix LS-energy-levels of different S but not of different J. The energy eigen functions $|{}^{2S+1}L'_J\rangle$ for the fine-structure Hamiltonian (2.2.2) will then have the form

$$|{}^1P'_1\rangle = -\beta|{}^3P_1\rangle + \alpha|{}^1P_1\rangle \tag{2.2.4}$$
$$|{}^3P'_1\rangle = \alpha|{}^3P_1\rangle + \beta|{}^1P_1\rangle \tag{2.2.5}$$
$$|{}^3P'_0\rangle = |{}^3P_0\rangle \tag{2.2.6}$$
$$|{}^3P'_2\rangle = |{}^3P_2\rangle, \tag{2.2.7}$$

where the mixing constants are linked to 2.2.3.

The mixing constants α and β can best be estimated from experimental knowledge of the states, such as the lifetime. The (dipole) transition lifetime τ of a state a that decays to a state b is given by [Bransden and Joachain, 1983]

$$\frac{1}{\tau(a)} = \frac{8\pi^2 e^2}{3\epsilon_0 \hbar} \frac{1}{\lambda^3} |\langle b|\mathbf{r}|a\rangle|^2 \tag{2.2.8}$$

where λ is the transition wavelength. We get

$$\frac{1}{\tau({}^1P'_1)} = \frac{8\pi^2 e^2}{3\epsilon_0 \hbar} \frac{1}{\lambda^3_{({}^1S_0 \rightarrow {}^1P'_1)}} \alpha^2 |\langle {}^1S_0|\mathbf{r}|{}^1P_1\rangle|^2 \tag{2.2.9}$$
$$\frac{1}{\tau({}^3P'_1)} = \frac{8\pi^2 e^2}{3\epsilon_0 \hbar} \frac{1}{\lambda^3_{({}^1S_0 \rightarrow {}^3P'_1)}} \beta^2 |\langle {}^1S_0|\mathbf{r}|{}^1P_1\rangle|^2 \tag{2.2.10}$$

and thereby

$$\frac{\alpha^2}{\beta^2} = \left(\frac{\lambda_{({}^1S_0 \rightarrow {}^3P'_1)}}{\lambda_{({}^1S_0 \rightarrow {}^1P'_1)}}\right)^3 \cdot \frac{\tau({}^3P'_1)}{\tau({}^1P'_1)}. \tag{2.2.11}$$

[4]The spin-orbit term does not mix the term of different n-quantum-numbers and it can be shown that in a sl-configuration $\mathbf{L}^2$ commutes with the spin-orbit term (2.2.3) if the $L = 0$ state is not perturbed by the spin-orbit term itself.

		$J=0$	$J=1$	$J=2$
		$6\ ^1S_0$	$6\ ^1P_1$	$6\ ^3P_2$
		$6\ ^3P_0$	$6\ ^3P_1$	
			$7\ ^3S_1$	
$I=\frac{1}{2}$	^{199}Hg	$F=\frac{1}{2}$	$F=\frac{1}{2},\ \frac{3}{2}$	$F=\frac{3}{2},\ \frac{5}{2}$
$I=\frac{3}{2}$	^{201}Hg	$F=\frac{3}{2}$	$F=\frac{1}{2},\ \frac{3}{2},\ \frac{5}{2}$	$F=\frac{1}{2},\ \frac{3}{2},\ \frac{5}{2},\ \frac{7}{2}$

Table 2.2: The possible hyperfine states for the two mercury fermions (given by the F quantum number for the total angular momentum) for the lowest fine-structure states.

With $\alpha^2+\beta^2=1$ and $1/\tau(^3P_1')=8.00\cdot10^6\mathrm{s}^{-1}$ ($\lambda=253.65$ nm), $1/\tau(^1P_1')=7.46\cdot10^8\mathrm{s}^{-1}$ ($\lambda=184.95$ nm) from [Lide, 1995] and [NIST, 2008] we get

$$\alpha = 0.986 \quad (0.9848) \tag{2.2.12}$$

$$\beta = -0.164 \quad (-0.1732) \tag{2.2.13}$$

where the bracketed numbers are the ones obtained in [Bigeon, 1967] (based on measurements of Landé factors), which sign convention is used for the unbracketed numbers.

With the calculations of the fine structure mixing coefficients in place we can now look at the $^3P_0$ state within the context of the hyperfine structure.

2.2.2 The hyperfine structure $^1S_0 \rightarrow {}^3P_0$ transition

In the hyperfine interaction the interaction between the nuclear spin I and the total angular momentum J of the electron cloud is added to the Hamiltonian. This splits the fine structure energy levels up into hyperfine states further characterized by $\mathbf{F}=\mathbf{I}+\mathbf{J}$. Table 2.2 shows the possible hyperfine states (possible F) for each of the lower states for the two mercury isotopes with non-zero nuclear spin (the fermions).

Now even $\mathbf{J}^2$ does not commute with the Hamiltonian and the $J=0$ state $|^3P_0'\rangle$ is mixed with $J=1$ states [Bigeon, 1967]. The hyperfine structure states are treated as a perturbation of the fine structure ones and the perturbation of the state $|^3P_0'\rangle$ can then be written (again neglecting configuration mixing)

$$|^3P_0''\rangle = |^3P_0'\rangle + \alpha_0|^3P_1'\rangle + \beta_0|^1P_1'\rangle, \tag{2.2.14}$$

or as a function of the pure LS-states (using (2.2.4)-(2.2.7))

$$|^3P_0''\rangle = |^3P_0\rangle + (\alpha_0\alpha - \beta_0\beta)|^3P_1\rangle + (\alpha_0\beta + \beta_0\alpha)|^1P_1\rangle. \tag{2.2.15}$$

This state mixing exists only for states of equal F, that is, $F = 1/2$ for ^{199}Hg and $F = 3/2$ for ^{201}Hg (those are the only isotopes with a non-zero nuclear spin) since those are the only possible hyperfine states of $|^3P_0\rangle$.

[Bigeon, 1967] has ascertained the values of the hyperfine structure mixing coefficients α_0 and β_0 for ^{199}Hg from measurements of hyperfine structure constants for different states and have obtained respectively $2.31 \cdot 10^{-4}$ and $-1.21 \cdot 10^{-5}$.

Using (2.2.8) we have[5]

$$\begin{aligned}\frac{1}{\tau(^3P_0'')} &= \frac{8\pi^2e^2}{3\epsilon_0\hbar}\frac{1}{\lambda^3_{(^1S_0\to{}^3P_0'')}}|\langle{}^1S_0|\mathbf{r}|^3P_0''\rangle|^2 \\ &= \frac{8\pi^2e^2}{3\epsilon_0\hbar}\frac{1}{\lambda^3_{(^1S_0\to{}^3P_0'')}}(\alpha_0\beta + \beta_0\alpha)|\langle{}^1S_0|\mathbf{r}|^1P_1\rangle|^2\end{aligned} \tag{2.2.16}$$

where we use that only the $^1S_0 \to {}^1P_1$ transition is allowed between the pure LS-states. By ignoring the hyperfine perturbation of the $^3P_1'$ lifetime we have

$$\frac{\tau(^3P_0'')}{\tau(^3P_1')} = \left(\frac{\lambda_{(^1S_0\to{}^3P_0'')}}{\lambda_{(^1S_0\to{}^3P_1')}}\right)^3 \frac{\beta^2}{\alpha_0\beta + \beta_0\alpha}. \tag{2.2.17}$$

From this a ^{199}Hg $^3P_0''$ lifetime of 1.51 s is obtained.

The $^3P_0$ transition lifetime depends on the isotope through the hyperfine mixing coefficient α_0 and β_0. Both of these are proportional to $\sqrt{I(I+1)}$ [Lurio et al., 1962] and can be written as a linear combination of hyperfine structure constants of the other P-states [Bigeon, 1967]. All hyperfine structure constants are proportional to the nuclear gyromagnetic ratio $\gamma_I = g_I\mu_N/\hbar$ (See for example [Bransden and Joachain, 1983]) and α_0 and β_0 are therefore proportional to γ_I. [Lehmann and Barbé, 1963] reports on the measurements of the relative gyromagnetic ratios of the two odd-numbered mercury isotopes: $\gamma_{I(201)}/\gamma_{I(199)} = -0.369$ which gives us (since

[5] As we ignore configuration mixing the ground state $|^1S_0\rangle$ is unchanged by both the spin-orbit coupling and the nuclear spin, that is $|^1S_0\rangle = |^1S_0'\rangle = |^1S_0''\rangle$.

I(^{199}Hg)= 1/2 and I(^{201}Hg)= 3/2):

$$\tau_{201}(^3P_0) = \tau_{201}(^3P_0) \cdot \frac{1}{5} \cdot \left(\frac{1}{0.369}\right)^2 = 2.22s. \tag{2.2.18}$$

In 1967 [Bigeon, 1967] reported on experiments where they by absorption in a mercury vapour cell in a nitrogen buffer gas measured the lifetime of the $^3P_0$ state for the two fermion isotopes and obtained

$$\tau_{199}(^3P_0) = 1.7 \text{ s}$$
$$\tau_{201}(^3P_0) = 2.4. \text{ s}.$$

The transition life times has independently being calculated in [Hachisu et al., 2008] which results in life times about 45 times longer for both fermions, in disagreement with the above calculations and experimental results.

We can conclude that for the two mercury fermion isotopes the $^1S_0 \rightarrow {}^3P_0$ transition is (weakly) allowed with a lifetime of a few seconds. In comparison the same transition in Yb has a lifetime of about 16 s and for Sr it is more than 150 s. While the natural linewidths of these magnitudes still are not a limiting factor on the lattice kind of clocks it is an advantage to have a stronger transition.

The stronger spin-orbit coupling in mercury allows both a stronger inter-combination $^1S_0 \rightarrow {}^3P_1$ transition, good for initial laser-cooling, and a stronger $^1S_0 \rightarrow {}^3P_0$ transition useable as a clock transition.

2.3 The mercury $^1S_0 \rightarrow {}^3P_0$ transition's sensitivity to electromagnetic fields

2.3.1 Blackbody radiation

The primary reason for choosing mercury as an atomic species for an atomic lattice clock is its clock transition's ($^1S_0 \rightarrow {}^3P_0$) low sensitivity to blackbody radiation. The typical 300 K background blackbody radiation is expected to be one of the main limiting factors of the accuracy and stability of future lattice clocks. The rms values of the electrical and magnetic fields of

blackbody radiation at a temperature T are

$$\langle E^2(t)\rangle = K_E^2\Big(\frac{T}{300}\Big)^4 \tag{2.3.1}$$

$$\langle B^2(t)\rangle = K_B^2\Big(\frac{T}{300}\Big)^4 \tag{2.3.2}$$

with $K_E = 831.9$ V/m and $K_B = 2.775 \cdot 10^{-6}$ T [Itano et al., 1982]. A corresponding frequency shift due to these fields is mostly due the Stark shift and has the form

$$\delta\nu = K_{EE}\Big(\frac{T}{300}\Big)^4. \tag{2.3.3}$$

The actual limiting factor of the frequency shift due to background blackbody radiation is the uncertainty in the absolute radiation temperature. If for example the fractional blackbody shift is of the order of 10^{-15} at 300 K, knowledge of the background radiation temperature better than 0.1 K together with a fractional uncertainty of less than 10^{-3} on the blackbody shift sensitivity is needed to obtain a fractional uncertainty of 10^{-18} of the clock transition due to the blackbody radiation. By having a lower blackbody shift it will relax these requirements. One solution is of course to cryogenically cool the surrounding vacuum chamber, like it is done for [Poitzsch et al., 1996] but this is a rather costly and bothersome affair both in terms of mounting and usage.

Table 2.3 shows theoretically calculated values of the fractional 300 K blackbody radiation shift of the clock transition of the most common atomic species used in atomic clocks including mercury. Notice how the BBR shift of the clock transition of mercury is a factor of respectively 16 and 34 lower than the two other atomic species used for lattice clocks, namely Yb and Sr. By choosing mercury as an atomic species for an atomic clock the sensibility to temperature fluctuations is less by at least a factor of 16. Notice also the even smaller blackbody shift for In^+ and Al^+ ions which are used for ion clocks. When compared with the most common atomic species used for microwave atomic clocks (Cs and Rb) the blackbody shift is on a whole different level.

2.3.2 First-order Zeeman splitting

An external magnetic field will remove the degeneracy of the atom's total angular momentum F in the quantization axis (usually chosen along the magnetic field) denoted by the quantum number M_F. For energy levels

	(Clock) Transition	BBR shift	uncertainty	Ref.
Al^+	$^1S_0 - ^3P_0$ (267 nm)	$-8 \cdot 10^{-18}$	$3 \cdot 10^{-18}$	[Rosenband et al., 2006]
In^+	$^1S_0 - ^3P_0$ (237 nm)	$(< 7 \cdot 10^{-17})$	$8 \cdot 10^{-19}$	[Rosenband et al., 2006]
Hg	$\mathbf{^1S_0 - ^3P_0}$ **(266 nm)**	$\mathbf{-1.6 \cdot 10^{-16}}$	$\mathbf{2 \cdot 10^{-18}}$	**[Hachisu et al., 2008]**
Mg	$^1S_0 - ^3P_0$ (458 nm)	$-3.9 \cdot 10^{-16}$	$1 \cdot 10^{-17}$	[Porsev and Derevianko, 2006]
Sr^+	$4^2S_{1/2} - 3^2D_{5/2}$ (674 nm)	$-5.4 \cdot 10^{-16}$	$(> 7 \cdot 10^{-17})$	[Mitroy et al., 2008]
Ca^+	$4^2S_{1/2} - 3^2D_{5/2}$ (729 nm)	$-9.2 \cdot 10^{-16}$	$2 \cdot 10^{-17}$	[Arora et al., 2007]
Ca	$^1S_0 - ^3P_0$ (660 nm)	$-2.6 \cdot 10^{-15}$	$5 \cdot 10^{-17}$	[Porsev and Derevianko, 2006]
Yb	$^1S_0 - ^3P_0$ (579 nm)	$-2.6 \cdot 10^{-15}$	$3 \cdot 10^{-16}$	[Porsev and Derevianko, 2006]
Sr	$^1S_0 - ^3P_0$ (698 nm)	$-5.5 \cdot 10^{-15}$	$1 \cdot 10^{-16}$	[Porsev and Derevianko, 2006]
Rb	$5S_{1/2}$ F=1 - F=2 (6.8 GHz)	$-1.3 \cdot 10^{-14}$	$2 \cdot 10^{-16}$	[Angstmann et al., 2006]
Cs	$6S_{1/2}$ F=3 - F=4 (9.2 GHz)	$-1.7 \cdot 10^{-14}$	$2 \cdot 10^{-16}$	[Beloy et al., 2006] [Simon et al., 1998]

Table 2.3: The theoretical fractional blackbody radiation shift at 300 K of the clock transition for different atomic species. The uncertainty is for the case where the temperature has an uncertainty of 1 K. The uncertainty for the blackbody radiation shift for Sr^+ is not directly reported in the reference. The uncertainty here refers to the 2-3 % uncertainty of the ground-state polarizability.

where $F \neq 0$ the magnetic field effectively splits the energy level up in $2F + 1$ magnetic sub-states whose energy shift (known as Zeeman shift) to first order in the magnetic field strength B is

$$\Delta E_{Zeeman}(\text{1st order}) = \mathbf{M} \cdot \mathbf{B} = g_F \mu_B M_F \cdot B, \tag{2.3.4}$$

where $\mathbf{M}$ is the atom's magnetic moment, μ_B is the Bohr magneton and g_F the Landé factor of the energy level. The atomic magnetic moment can be decomposed into

$$\mathbf{M} = \frac{\mu_B}{\hbar}(g_L \mathbf{L} + g_s \mathbf{S} - g_I \mathbf{I}), \tag{2.3.5}$$

where $g_L = 1$ is the angular momentum Landé factor, $g_s = 2$ the spin momentum Landé factor and g_I the nuclear Landé factor. For the case of the clock transition ($^1S_0 \rightarrow {}^3P_0$) both energy levels have $F = I$ and they are split up in two ($M_F = -1/2, 1/2$) for ^{199}Hg and in four ($M_F = -3/2, -1/2, 1/2, 3/2$) for ^{201}Hg. Since $\Delta M_F = 0, \pm 1$ for a (E1) transition depending on the polarization of the laser light and the angle between the magnetic field and the laser beam, this leads to a number of possible transitions (some with the same Zeeman shift) between the magnetic sub-states on the clock transition as shown in figure 2.3.

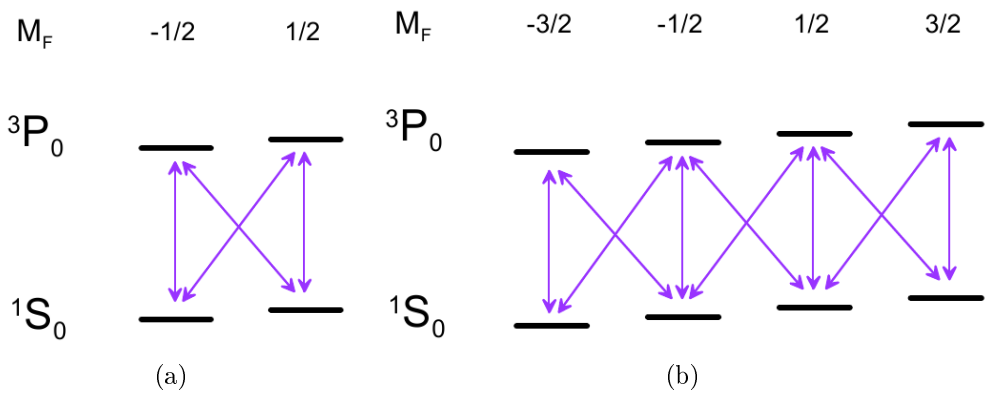

Figure 2.3: The Zeeman splitting of the clock transition levels and the possible transitions in between the sub-states for (a) ^{199}Hg and (b) ^{201}Hg.

Due to the hyperfine mixing of $^3P_0$ with $^3P_1$ and $^1P_1$, in which the atom has a strong (electronic) magnetic moment, the Landé factor is not the same for the two clock levels. As long as we do not consider configuration mixing of states the $^1S_0$ ground state has $\mathbf{L} = 0$ and $\mathbf{S} = 0$ and from the known ground state magnetic moment of mercury (0.5059 and -0.5602 in units of the nuclear magneton μ_N for ^{199}Hg and ^{201}Hg respectively [NIST, 2008]) we have $g_I = -5.51 \cdot 10^{-4}$ for ^{199}Hg and $g_I = 2.03 \cdot 10^{-4}$ for ^{201}Hg.

To estimate the Landé factor of $^3P_0$ we look at the element $\langle {}^3P_0''|\mathbf{M}|{}^3P_0''\rangle$ by using (2.2.15) to write the state $|{}^3P_0''\rangle$ as a sum of pure LS-states. For ^{199}Hg we have $\alpha_0\alpha - \beta_0\beta = 2.26 \cdot 10^{-4}$ and $\alpha_0\beta + \beta_0\alpha = -4.98 \cdot 10^{-5}$ and we therefore ignore terms squared in those. This leaves

$$\begin{aligned}\langle {}^3P_0''|\mathbf{M}|{}^3P_0''\rangle =& \langle {}^3P_0|\mathbf{M}|{}^3P_0\rangle + 2(\alpha_0\alpha - \beta_0\beta)\langle {}^3P_0|\mathbf{M}|{}^3P_1\rangle \\ &+ 2(\alpha_0\beta + \beta_0\alpha)\langle {}^3P_0|\mathbf{M}|{}^1P_1\rangle. \end{aligned} \tag{2.3.6}$$

The first term is equal to the ground state atomic magnetic moment while the last term is zero. The second term has been evaluated in [Boyd et al., 2007] [Lurio et al., 1962]:

$$\langle {}^3P_0|\mathbf{M}|{}^3P_1\rangle = \mu_B M_F \sqrt{\frac{2}{3I(I+1)}}. \tag{2.3.7}$$

For ^{199}Hg the difference between the Landé factors in $^1S_0$ and in $^3P_0$ is then $-4.3 \cdot 10^{-4}$. This can be compared with the calculated result published in [Hachisu et al., 2008] which tells us that $g_F(^1S_0) - g_F(^3P_0)$ is $-4.7 \cdot 10^{-4}$ and

$M_F(^1S_0) \setminus M_F(^3P_0)$	-1/2	1/2
-1/2	-0.33	1.1
1/2	-1.1	0.33

Table 2.4: The Zeeman shift in kHz of the possible transitions between the ^{199}Hg clock state sub-states due to an external magnetic field of 1 G.

$M_F(^1S_0) \setminus M_F(^3P_0)$	-3/2	-1/2	1/2	3/2
-3/2	0.38	-0.16	-	-
-1/2	0.66	0.13	-0.41	-
1/2	-	0.41	-0.13	-0.66
3/2	-	-	0.16	-0.38

Table 2.5: The Zeeman shift in kHz of the possible transitions between the ^{201}Hg clock state sub-states due to an external magnetic field of 1 G.

$1.8 \cdot 10^{-4}$ for ^{199}Hg and ^{201}Hg respectively and for ^{199}Hg the two calculations coincide. For ^{201}Hg the situation is a bit more complicated than for ^{199}Hg since the quadrupole term in the hyperfine structure Hamiltonian might not be negligible which would lead to a mixing between the pure $^3P_0$ and $^3P_2$ states. A reference for the hyperfine structure constant of ^{201}Hg has also not been found.

Table 2.4 and 2.5 shows the result of calculating the shift of the magnetic sub-states due to a 1 G external magnetic field for the two fermions. For ^{199}Hg we see from the table that a magnetic field could split the transition up into four sub-transitions symmetrical around the clock transition frequency. If the magnetic field and the clock beam is such that all those sub-transitions are present a simple average of the $\pm M_F$ transitions should lead to a transition frequency free of the (first order) Zeeman effect. Similarly an external magnetic field on ^{201}Hg atoms would lead to a symmetric magnetic splitting of the clock transition into ten components.

It should also be mentioned that [Hachisu et al., 2008] estimates the second order Zeeman shift constant to be about 24.4 mHz/G^2.

2.3.3 Light shift and the magic wavelength

Laser light in itself will perturb the atom causing a shift in its transition frequencies - specifically the clock transition.

We only consider the stark shift since the electric interaction is much stronger than the magnetic interaction. Following for example [Lide, 1995] the energy shift of an atomic transition between states 1 and 2 due to an external electric field ε is

$$\Delta E_{12} = -\frac{1}{2}(\alpha_2 - \alpha_1)\varepsilon^2, \tag{2.3.8}$$

where the AC polarizability α_i can be written

$$\alpha_i = \frac{e^2 h^2}{4\pi^2 m_e} \sum_j \frac{f_{ij}}{(E_j - E_i)^2 - (h\nu)^2}, \tag{2.3.9}$$

with the sum being across all atomic transitions connected to this the state i. Here m_e and e are the electron's mass and charge respectively, f_{ij} the oscillator strength for the transition between the states i and j and ν the frequency of the light.

Given available experimental data, we can not include the infinite number of transitions in (2.3.9). For dealing with the light shift of the clock transition of mercury we are limited by the knowledge of the transition strengths and we include the transitions from the ground state $^1S_0$ to $^1P_1$ and $^3P_1$ and the transitions from the excited clock state $^3P_0$ to 7 $^1S_0$, $^3D_1$, 7 $^3S_1$ and 8 $^3S_1$. We do not include the clock transition itself since it is extremely weak in comparison.

When considering the clock transition's dependency on laser light we assume that when probing the transition all other light sources than the probe-beam itself and the lattice dipole trap light are turned off or shielded. For instance if the probe beam is a 3 nW 100 μm waist beam (corresponding to a Rabi frequency of $\sim$ 10 Hz) then the above calculations show a $\sim$600 μHz light shift.

We estimate the need of enough laser power to have a trap depth of ten times the recoil frequency that is a maximum field intensity of $\sim$ 60 kW/cm^2. Figure 2.4 shows the calculated light shift of the clock transition as a function of the laser wavelength for such an intensity using the aforementioned method. The sharp peaks are where the laser is closely tuned to one of the transitions and here the calculations are not correct. The key element of the dipole trap is to use a laser at a wavelength where the light shift is close to zero (the magic wavelength) and simultaneously having a small sensitivity to the wavelength. In this vicinity of the clock transition we

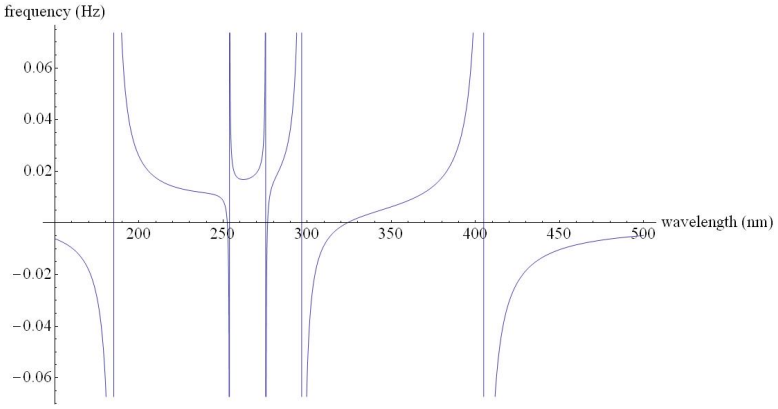

Figure 2.4: Pertubative estimation of the clock transition light shift due to a dipole trapping laser providing a trapping depth of ten times the recoil frequency as a function of the laser wavelength. Notice how the light shift crosses zero near 325 nm.

notice that near 325 nm the light shift crosses zero far from any resonances and we are aiming for this as the magical wavelength.

[Hachisu et al., 2008] reports on more in depth calculations comparing ac polarizabilities of the clock transitions which have given a magic wavelength ranging from 342 nm to 360 nm. In comparison calculations of the magic wavelength for Sr was 800 nm [Katori et al., 2003] with the actual measured value being 813.43 nm [Takamoto et al., 2005], [Ludlow et al., 2006], [Brusch et al., 2006]. For Yb the calculated value was 752 nm [Porsev et al., 2004] with 759.35 nm being the measured value [Barber et al., 2006].

Chapter 3

Laser source for cooling on the neutral mercury $^1\mathbf{S}_0$ - $^3\mathbf{P}_1$ transition

The first stage in our lattice clock will be to laser-cool and trap the atoms in a MOT using the relatively narrow $^1S_0 \rightarrow {}^3P_1$ transition as cooling transition. One of the challenging tasks of using neutral mercury in a lattice clock is to obtain enough CW power for laser-cooling at the 253.7 nm cooling transition in the deep UV with a line width narrow in comparison with the cooling transition's 1.3 MHz natural line width. For us an additional requirement is the need of enough laser power for both a MOT and the atomic pre-selection in a 2D-MOT.

3.1 The source of high power laser light at 253.7 nm

Initially we assumed the need of at least a couple of hundred mW of power for the MOT and the 2D-MOT hoping for more. To create this amount of power at the cooling transition at 253.7 nm, we choose to start with light at the quadruple wavelength and then frequency-double the light twice. A similar setup has been published in [Scheid et al., 2007], where a stable power output of 750 mW at 253.7 nm is reported. As shown in figure 3.1, which shows the optical setup of the laser light, we exclusively use the main output of the second frequency doubling cavity for the MOTs while we use

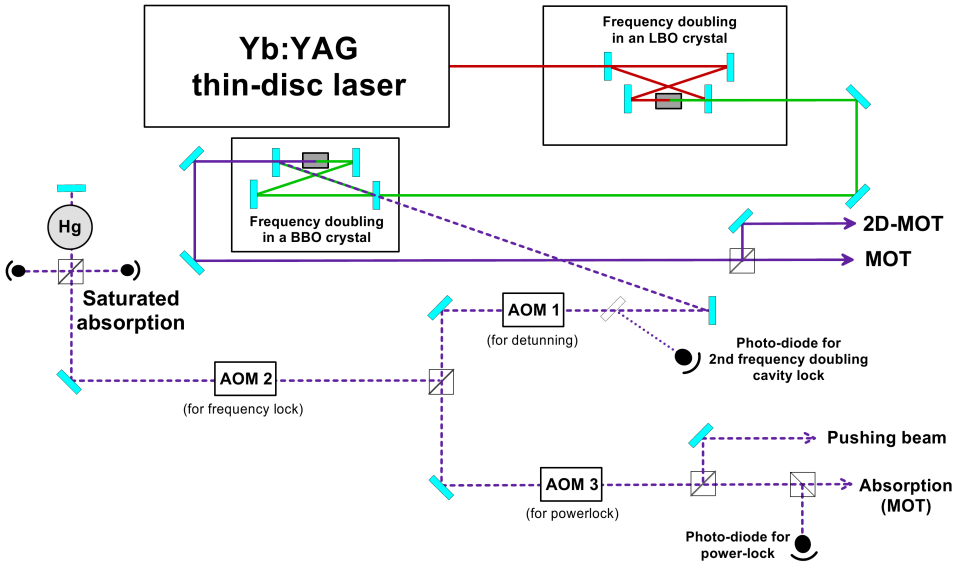

Figure 3.1: The setup for creating the cooling light. The light from the thin-disc laser is frequency doubled twice. The main output of the second frequency doubling is used exclusively for the MOT and the 2D-MOT, while we use a leak from the doubling cavity for all other purposes. The second doubling cavity is locked by side-lock and the laser itself is frequency locked on the saturated absorption signal in a mercury vapour cell. A power stabilized part of the cavity leak is used for absorption measurements and as a possible pushing beam in the 2D-MOT. AOM 1 is used solely for detuning the cooling light's frequency from the mercury transition and to counteract the locking AOM's (AOM 2) 180 MHz frequency shift.

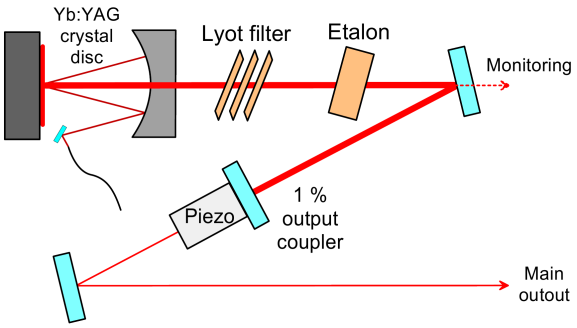

Figure 3.2: The 'Versadisk' Yb:YAG thin-disc laser used as initial laser source for laser cooling. For frequency selection the laser cavity contains an etalon and a Lyot filter, while the output coupler is mounted on a piezo, which is used for frequency locking the laser. The wavelength and the intra-cavity power is monitored through a mirror leak.

a UV leak (a reflection off the output coupler transmitted through the input coupler) from the second frequency doubling cavity as an auxiliary beam for remaining purposes such as laser frequency lock, cavity lock and probing.

Since the cooling light is in the far UV the optics used for it required special attention. All optics used for the UV are made in UV-grade fused silica transparent to UV-light down to 180 nm. For the main output of the frequency doubling cavity and for the MOT and 2D-MOT we used 254 nm AR coated lenses while we mostly could use non-coated lenses on the auxiliary beam since we required much less than the couple of mW of power available. We had to use high-quality high-damage-threshold optically contacted polarizer cubes everywhere since the lower quality ones takes damage very easily at our UV-wavelength. Even a 50 mW focused beam do not seem to have any damaging effect on our high-quality optically contacted cubes. Over time several waveplates in the main output have taken visible damage from the power and are due for replacement.

3.1.1 The Versadisk laser

The initial laser-source is a commercially available Yb:YAG crystal thin-disc ('Versadisk') laser from ELS which in the present configuration delivers up to 8 W at 1014.9 nm with an optimal power output around 1030 nm of up to 50 W.[1] The lasing medium is a 240 μm thick, 10 mm wide disc of Yb-doped

[1] This requires a change of output coupler though.

YAG crystal. The up to 100 W of 938 nm pumping light originating from an array of diode-lasers via optical fiber is reflected internally in the disc 24 times. The disc assembly is water cooled with the chiller (kept outside the lab) at about 20° C. The laser cavity is made of the disc's backside and the 1 % output coupler which is the main output of the laser (see figure 3.2). The output coupler is mounted onto a piezo-electric element and together with a Lyot filter and an etalon is used for frequency selection. We are using a leak through a second internal mirror for monitoring the lasing-power with a photo-diode and for monitoring the wavelength with a WA-1000 wavemeter.[2]

We have now enclosed the laser (and the first doubling cavity) inside a box of about 2 cm thick PVC foam to reduce temperature fluctuations and acoustic noise in the laser. We externally control the angle of the Lyot filter (along one direction) and the angles of the output coupler (both directions) from a PC using picomotors with piezo-driven micrometer screws. With the control of the Lyot filter we have a crude control of the wavelength down to the etalon filter's free spectral range of about 85 pm. The output coupler control is used to optimize intra-cavity (and output) power. By temperature control of the etalon we are able to fine tune the wavelength down to the level of a couple of hundred kHz with a range of more than hundred pm. Unless changing isotope we try to only use the temperature control for fine-tuning in the less-than-a-pm range. The piezo-control is used for finding the cooling transition when within a couple of hundred kHz and for locking the laser's frequency to the saturated absorption (see subchapter 3.3 for more details). Due to the high intra cavity power we often observed a correlation between change of intra-cavity power and wavelength. Often when optimizing the power with for example the output coupler control we could observe a change of wavelength of a few pm.

Since the beginning of this project the disc laser has been one of most trouble-some pieces of equipment. In the first four months of operation there was no external control of the output coupler and unknown to us there was no etalon inside the etalon mount. The laser has a tendency of doing thermal oscillations with an extremely high amplitude when being near a

[2]The wave-meter has a precision of about 1 pm (uncalibrated) with an instability of about 1 pm over some months. The wavemeter has broken down a number of times during this project and each time it lead to a shift of a few pm's (compared with the mercury transition).

mode hop. Due to the lack of external control of the laser we did not pay enough attention to avoid these regions and at the end this probably caused a fissure in the crystal disc. Because of problems related to finding a good replacement crystal it was stuck at the factory for repairs for 10 months. After the return of the laser in the summer of 2007 we have been much more mindful of how we operate and turn on and off the laser. We have included all the aforementioned external controls, which we use to optimize power and frequency and to avoid the regions between modes several times a day.

So far we turn off the laser each night. This is done carefully to decrease thermal constraint on especially the crystal disc. The pump-laser power is decreased in steps of three Amps of a couple of minutes until the lasers threshold is reached. The laser power is turned on again in steps of three Amps of 20 minutes. The lasing threshold is at about 12-13 A of pumping current when turning the laser off in the evening while the threshold in the morning is between 14-18 A. At the present time we are running the pumping array at 24 A. The current factory maximum is at 27 A leaving room for a possible power increase if we solve other limiting factors such as the decreasing efficiency of the second frequency doubling cavity and the negative effect of high power UV-light on the optics.

3.1.2 The frequency doubling cavities

To frequency double the light we do second harmonic generation (SHG) in crystals that have relatively large non-linear (second-order) dielectric polarization coefficients. We want to end up with as much power as possible and since the conversion coefficients of doubling crystals are typically rather low we use them inside build-up cavities.

The first frequency doubling is a commercial system obtained with the thin-disc laser. It is a bow-tie cavity with a 90° phase matched LBO (Lithium triborate) crystal. The temperature of the LBO crystal is stabilized at the phase matching temperature of 210° C. The cavity is locked by an electronic system delivered with the doubling system using the Hänsch-Couillaud locking method [Hänsch and Couillaud, 1980]. With an input of 7 W at 1015 nm, we obtain an output of at least 3 W at 507 nm.

The second frequency doubling is done in a home-made 241 mm long bow-tie cavity (see figure 3.3). Since it is a requirement that the crystal is transparent to the far UV it is necessary to use a BBO (Beta barium

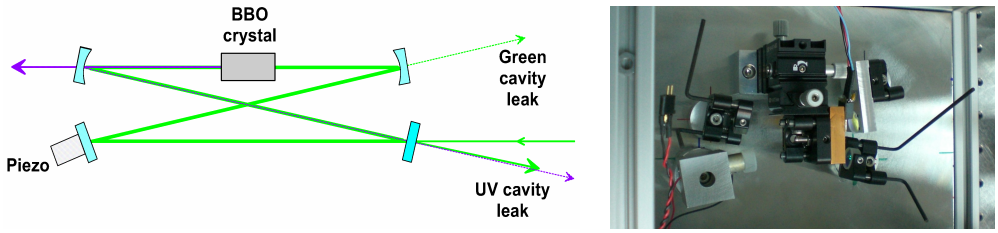

(a) (b)

Figure 3.3: (a) A diagram of the second frequency doubling cavity. The green cavity leak is used for monitoring internal cavity power and initially for locking the cavity. (b) The corresponding picture of the cavity inside the protecting box of PVC foam.

borate) crystal which has a transparency down to 190 nm. The generated SHG light has a non-negligible amount of spatial walk-off (walk-off angle 85 mrad) which distorts the output beam shape. We use a 7 mm long AR coated BBO crystal which should be (type I) phase-matched at an angle of about 51.2°.[3] The copper mount that holds the crystal is being heated up above 30° C to reduce moisture on the crystal. We use a flat input coupler with a reflection of 98.5 %, one flat mirror and two curved mirrors with a 50 mm radius of curvature (see figure 3.3). The curved mirror which acts as an output coupler for the UV light is made of UV-grade fused silica and has a custom coating which reflects 99.8 % at 507 nm and transmits 95 % at 254 nm. The two other mirrors has a reflection of at least 99.8 % at 507 nm. The cavity has a 28 μm waist inside the crystal and the second waist between the two flat mirrors is 100 μm.

By using a (green) leak through one of the mirrors we monitor the intra-cavity power and thereby measured the cavity finesse (see figure 3.4). This was done at low power so to avoid losses due to SHG in the non-linear crystal. With a free spectral range of 1.3 GHz and a FWHM linewidth of 5.6 MHz the cavity had a finesse of about 230.

Initially we used the green leak for locking the cavity to a cavity resonance. The cavity lock is done by side-locking, which is a very simple way of locking on the side of a cavity resonance. The photodiode signal is simply offset to have a zero point on the side of the resonance and then by

[3]We have tried using a non-coated brewster-cut crystal (using an appropriate cavity configuration with the same optics), but it did not show any improvement compared with the present setup, probably due to the less adapted input coupler.

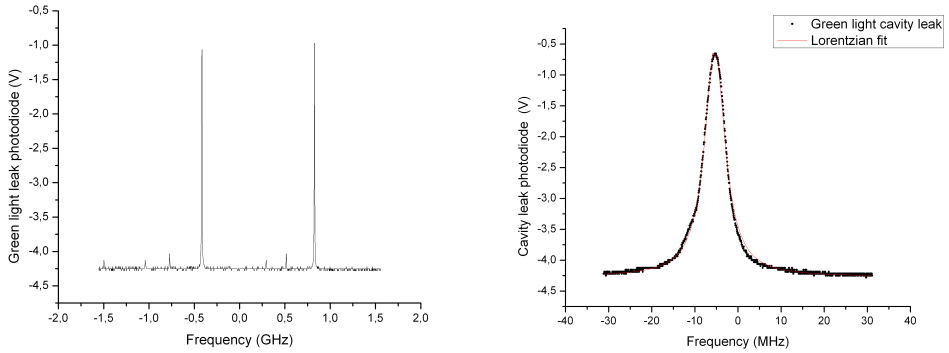

(a) (b)

Figure 3.4: (a) A free-spectral-range of the doubling cavity measured at a cavity leak (measured in the green). (b) A close-up of the cavity resonance and a lorentzian fit giving a FWHM of 5.6 MHz.

single integration the cavity piezo locks the cavity to this point. It is the simplicity of this method that was the main reason for choosing it as the mean of locking the doubling cavity. Using this method we have succeeded in continuously locking the cavity at an output of 800 mW of 254 nm light with an in input of about 3.4 W. We have not been able to reobtain this at a later time and there seem to have been a continuous degradation of the output-power of the cavity. This is partly due to an actual local (both permanent and non-permanent) damage in the crystal which we can avoid by occasionally translating the crystal. But there is also clear evidence of damage to the UV output coupler. We are now locking the UV-light at a lower power and at the moment we are running the experiment with no more than 125 mW of initial UV-light.

The BBO crystal unfortunately induces a large amount of spatial walk-off on the frequency doubled light. More than 10 cm from the BBO crystal the shape of the main output beam becomes that of a double "hamburger" meaning 4 horizontal stripes with the top and the bottom ones being larger than the middle ones. By sending the light through a series of spherical and cylindrical lenses we have managed to create a beam shape where most of the beam power is in a central somewhat circular bulge with smaller fringes on top and bottom which we chop off using knife-edges. About 10 % of the power is lost in the chopping process and even though the beam is a somewhat round shape without fringes it has a non-negligible amount of

astigmatism.[4]

3.1.3 The UV cavity auxiliary beam

To avoid using power from the main beam we use a (UV) leak from the doubling cavity for locking, detection and other purposes that require little power (see figure 3.1). The UV leak overlaps with the cavity reflection and by sending these through a UV-grade fused silica prism we are able to split up the two beams (this is not included in figure 3.1). The UV beam is then reshaped by a series of spherical and cylindrical lenses.

A UV window reflects a small amount of light onto a photo-diode which is used for locking the UV-cavity. By locking on the frequency doubled light (still using the aforementioned method of side locking) instead of the green light we achieve a better power stability.

After passing through two AOM's (using respectively the -1. and the 1. order output) the beam is sent into a saturated absorption setup which in the end is used for frequency locking the thin disc laser (see subchapter 3.3). The second AOM (AOM 2 in figure 3.1) is used for the locking scheme with a frequency offset of about 182.5 MHz while the first one (AOM 1) has a detuning of about 177 MHz to keep the UV-light sent towards the MOT 5.5 MHz below the cooling transition. Between the two AOM's some of the light is split off and send through another 182.5 MHz AOM (1. order) so the following light is at the cooling transition. This light is used as a pushing beam and after a power-stabilization for absorption measurements in the vacuum chamber.

3.2 Doppler-free spectroscopy of the $^1S_0$ - $^3P_1$ transition

To laser-cool atoms it is necessary to stabilize the cooling laser's frequency to better than the cooling transitions natural linewidth. As mentioned in chapter 2 the natural linewidth of the mercury cooling transition is 1.3 MHz while the Doppler width at room temperature is about 800 MHz. This makes it necessary to lock the laser to a saturated absorption signal.

[4]Due to a faulty delivery of UV optics we have not been able to satisfactory compensate for this when we started implementing the MOT.

Saturated absorption measurements is a method to obtain an effectively Doppler-free spectral line of a transition and can be done by double-passing light through a vapour cell. The principle of saturated absorption is to only saturate the transition of atoms whose Doppler shift is small compared to the natural linewidth. A probe beam detuned from the atomic transition will interact with different velocity-classes of atoms on passing and returning through the atoms, but if the probe frequency is within the natural linewidth of the transition it will interact with the same velocity class of atoms, namely atoms at rest or nearly at rest in the direction of the probe. If the probe light has an intensity close to the saturating intensity (10.2 mW/cm^2 for the mercury cooling transition) the transition of atoms at rest will saturate more strongly than for other atoms and a sharp decrease in the absorption can be observed. If the probe frequency is scanned a small inverted peak with the power-broadened natural linewidth of the transition can be seen at the top of the Doppler-broaden absorption feature.

To have the strongest possible signal in a retro-reflected configuration we want to have a strong absorption, while still keeping a non-negligible amount of light left after a one-pass absorption to have non-vanishing signal on the double pass. This is an important point for mercury due to its high vapour pressure at room temperature.

We can estimate the necessary thickness of a vapour cell to be used for saturated absorption by calculating the absorption of light through a vapour of atoms (see subchapter 4.2.1 for further details). 10-50 % absorption on a single pass is optimal.

At room temperature the vapour pressure of mercury is about 0.25 Pa [Alcock, 1995] and by taking into account the 17 % abundance of the most probable candidate for the atomic clock ^{199}Hg we obtain that only 1 mm vapour of ^{199}Hg is enough to absorb 44 % of the light and after half a centimeter less than 6 % of the light is left. Even ^{204}Hg which only has an abundance of 6.9 % absorbs 21 % of the light after 1 mm. For the scarce 0.15 % abundant ^{196}Hg isotope only 0.5 % of the light is absorbed after 1 mm and only after more than 2 cm the absorption exceeds 10 %. For the most abundant (30 %) isotope ^{202}Hg the single pass (non-saturating) absorption is 65 %. This indicates that a 1 mm thick cell will let us do the saturated absorption on all the abundant mercury isotopes. This can be compared with for example cesium or rubidium that requires 10-20 mm wide cells for optimized saturated absorption on the D2-line.

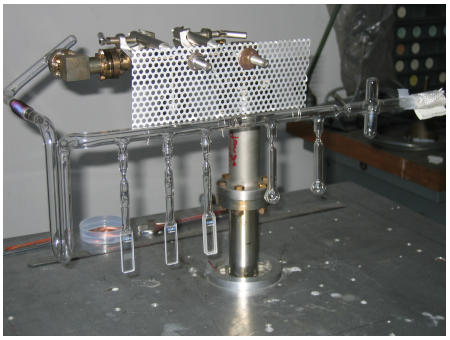

(a)

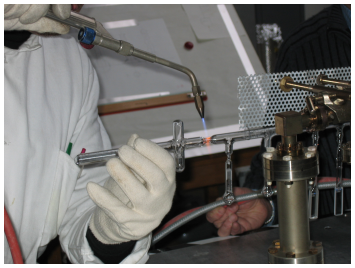

(b)

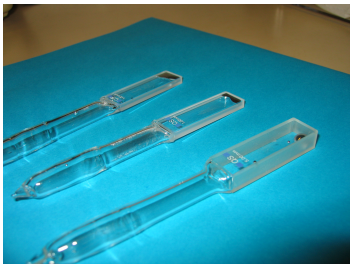

(c)

Figure 3.5: (a) The setup used to distillate the mercury into the vapour cells used for saturated absorption. The setup is kept under vacuum. The right cell is the initial source of (purified) mercury, the middle cells are intermediate cells for doing multi-stage distillation and the cells to the left are the final vapour cells (b) The process in which the different cells are disconnected maintains the vacuum in both the vapour cell and the distillation chamber. (c) The final vapour cells containing mercury. We have two 1 mm cells and one 5 mm cell at our disposal.

We use commercially available 1 mm quartz cells which we have filled with distillated mercury using the system shown in figure 3.5(a). The distillation system was kept under vacuum during the distillation process where we heated up the source cell with a bunsen burner while keeping the target cell(s) submerged in liquid nitrogen or ice water. To obtain a purer mercury this process was repeated several times before ending with the quartz cells. As shown in figure 3.5(b) several parts (including the quartz cells themselves) were disconnected from the distillation system during the process. This was done in a way to maintain the vacuum in both the distillation system and the detached cell.[5]

[5]We thank the glass blower of l'Observatoire de Paris Pierre Bonnay for his assistance

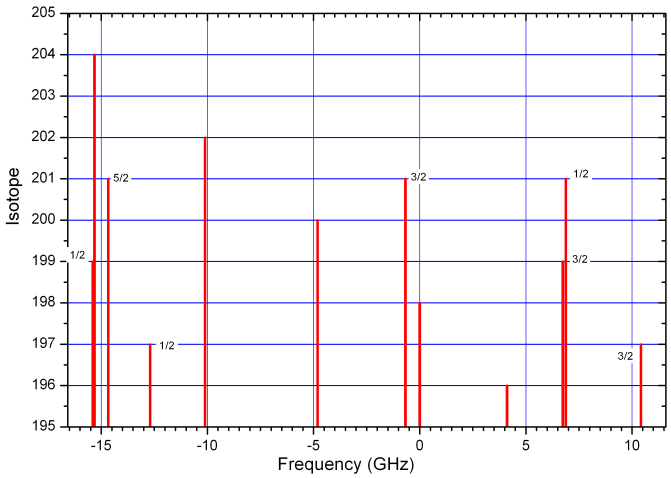

Figure 3.6: These columns shows how the cooling transition frequencies for different isotopes relates to one another [Bitter, 1962]. ^{196}Hg is a rare isotopes where we could only observe the Doppler-profile and ^{197}Hg is an artificial isotope used for medical purposes. Notice the close to linear relationship for the bosonic isotopes.

The saturated absorption is done by sending the appropriate light through the cell then retro-reflecting it back before it being measured with a photo-diode. A reference is being measured before the cell so to subtract amplitude noise from the signal. A $\lambda/4$-waveplate is placed between the cell and the retro-reflecting mirror. A horizontal coil with 200 windings of about 40 mA of current placed around the vapour cell compensates a 1.6 G external vertical magnetic field which had been Zeeman-splitting the saturated absorption signal.

Initially we worked on the ^{202}Hg cooling transition since this is the most abundant isotope. By scanning the laser frequency 20 pm (around 1014.9 nm) it was possible to obtain the saturated absorption signal from all nine possible cooling transitions for the naturally abundant isotopes (see figure 3.7). The ^{196}Hg Doppler profile was only visible in our 5 mm vapour cell. We have not tried to observe the saturated absorption feature of this isotope.

in this process.

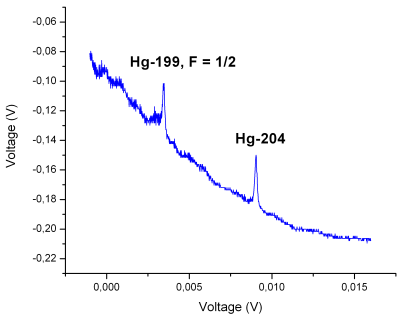

(a)

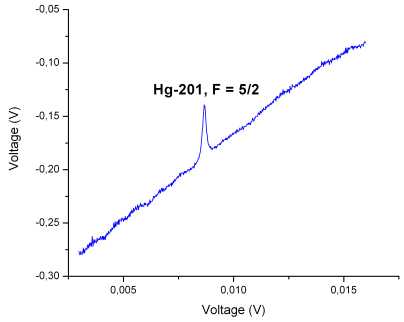

(b)

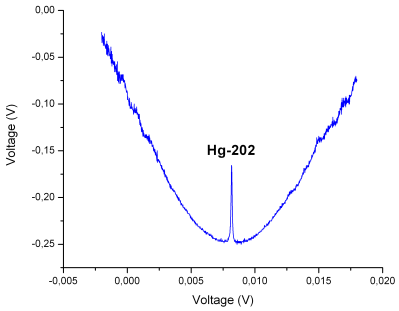

(c)

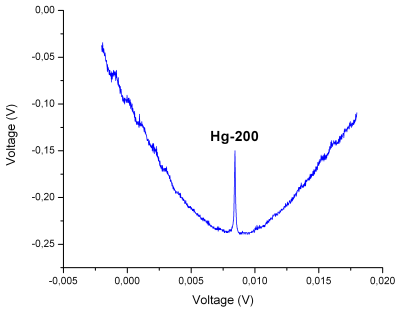

(d)

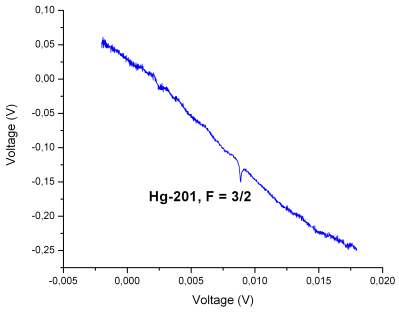

(e)

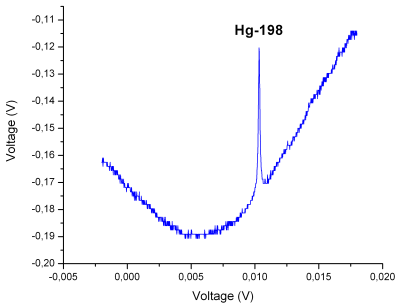

(f)

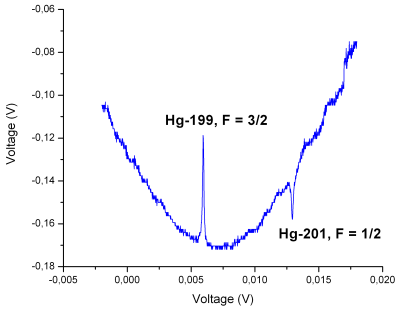

(g)

Figure 3.7: The measured saturated absorption peaks from all the abundant isotopes.

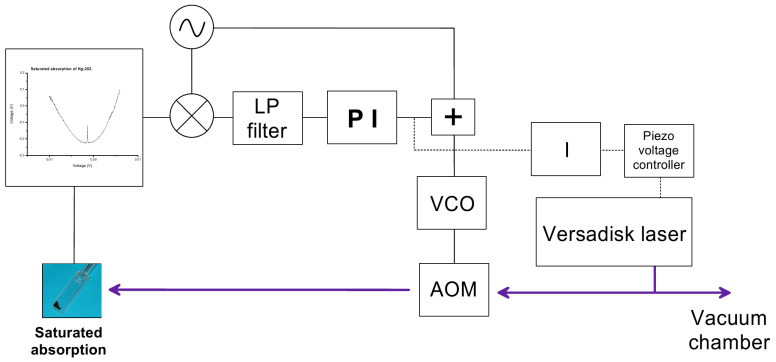

Figure 3.8: The thin-disc laser is frequency locked to the saturated absorption signal by this system of nested loops. First an AOM is locked to the signal by homodyne detection at 300 kHz. The correction signal from this loop is then fed into another integrator and then used to lock the laser itself by controlling the laser cavity piezo.

3.3 Stabilizing the laser source to the saturated absorption signal

To avoid sending too much light through an AOM and to avoid modulating the light sent to the MOT we have chosen not to frequency lock the cooling directly with an AOM. This way we had maximum available power sent towards the MOT when searching for the cold atoms the first time. In all cases a second stabilization of the laser light is needed since an AOM does not have enough dynamic range to compensate for the free-running laser's frequency drift.

We are stabilizing the laser itself to the saturated absorption signal with a double nested loop as shown in figure 3.8. In the inner servo-loop we lock an AOM (AOM 2 in figure 3.1 on the auxiliary beam) to the saturated absorption by the method of homodyne detection with a 300 kHz modulation frequency using a proportional-integrator gain. The outer servo-loop simply takes the correction signal as an input which is integrated upon once more before being used to frequency lock the laser with the cavity piezo.

To accurately test the effectiveness of this locking scheme we measured the saturated absorption signal in a second mercury cell on the actual main beam used for the MOT while the laser being locked on the regular saturated absorption cell on the cavity leak (see figure 3.9). We could then be certain of the effectiveness of the frequency lock on the actual light that would be

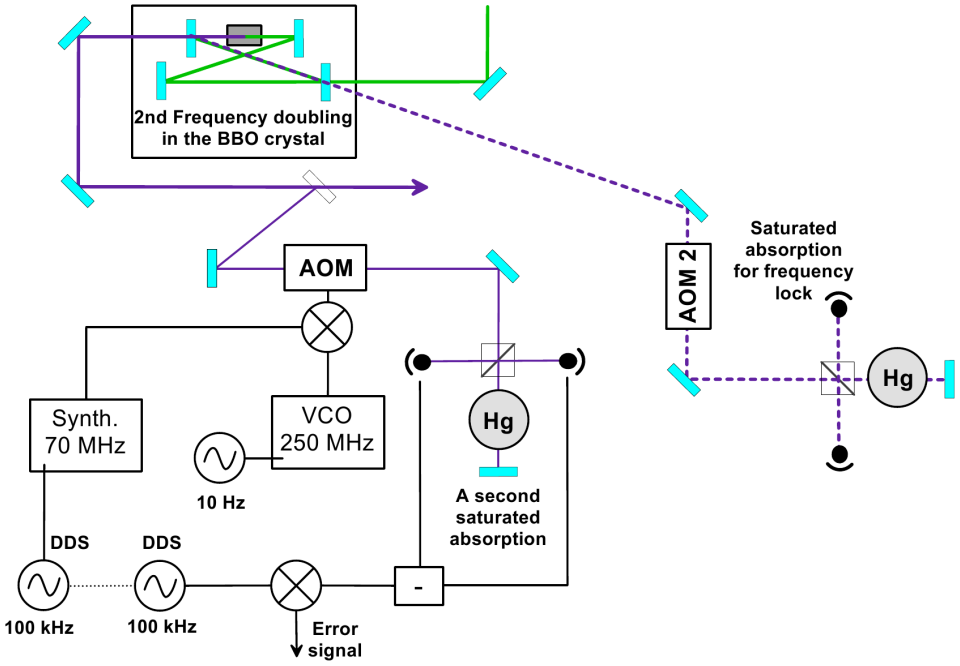

Figure 3.9: A temporary setup for testing the efficiency of the laser frequency lock. While the laser is locked to the saturated absorption signal on a cavity leak, a second saturated absorption signal is obtained from the main cavity output. An error signal is created by a 100 kHz homodyne detection of the signal. The 10 Hz input into the VCO is to scan the signal.

used for creating the MOT and verify that we could lock the light tighter than the natural linewidth of the cooling transition.

To avoid having too much power we used a reflection of a UV-grade fused silica window. We coupled the light through an AOM to be able to scan the saturated absorption signal and to be able to obtain an error signal by yet another homodyne detection. Since this was just a temporary setup we used a 70 MHz synthesizer in which we could input the 100 kHz homodyne frequency to be able to mix the homodyne frequency with the VCO output. We used two different (synchronized) phase-tunable 100 kHz DDS' (Direct Digital Synthesizers) to be able to control the phase shift on the homodyne mixing.

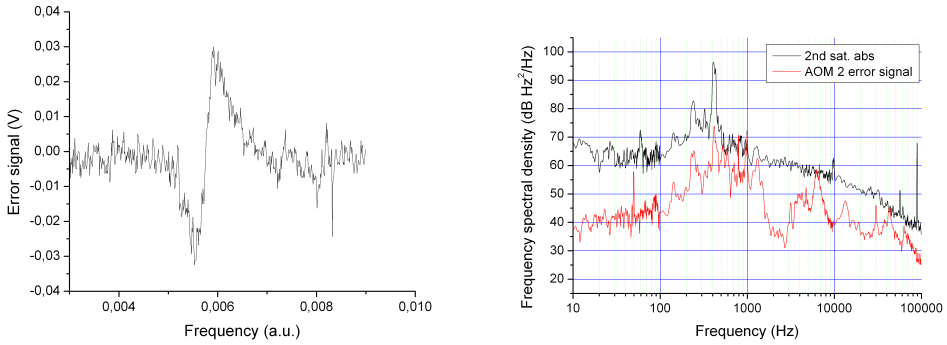

(a) (b)

Figure 3.10: (a) The error signal obtained from the second saturated absorption of a second mercury vapour cell while the laser being locked to the regular saturated absorption signal. The signal is being swept at 10 Hz with an AOM. (b) In black the frequency spectral density of the same error signal while the frequency of the additional AOM was positioned at the zero crossing point without being swept. In red is shown the error signal of AOM 2 of figure 3.1 while the laser is locked to the saturated absorption signal.

Figure 3.10(a) shows a resulting error signal while sweeping the (second saturated absorption) AOM at about 10 Hz. This showed a clear and steady error signal and this was an indication that the laser lock indeed was tighter than the natural linewidth of the transition assuming that the signal was not power-broadened. To better quantify this we stopped sweeping the AOM and positioned the AOM frequency so the error signal was at the zero crossing point. By measuring the error signal positioned around the zero

crossing point with a dynamic signal analyzer we could calculate the relative frequency spectral density as shown in figure 3.10(b) (in black). The graph is shown in comparison with a measurement of the error signal of the locking AOM (AOM 2 in figure 3.1) while the laser is locked at maximum gain to the saturated absorption signal. We estimate that for frequencies higher than 1-2 kHz the noise measurement on the second saturated absorption is limited by noise from the electronics. For lower frequencies we believe it shows the true noise of the laser limited by the noise of the laser piezo. The tightness of the lock made this measurement possible since the non-swept error signal never came close to the error signal turning points. By sweeping the 70 MHz RF synthesizer we could estimate the line width as less than 2 MHz.

The phase noise power spectral density can be obtained using [Vanier and Audoin, 1989]

$$S_f(f) = f^2 S_\phi(f). \tag{3.3.1}$$

From the phase noise spectral density we can then estimate the locked laser linewidth $\Delta\nu$ using the linewidth definition [Halford, 1971]

$$\int_{\frac{\Delta\nu}{2}}^{\infty} S_\phi(f)\mathrm{d}f = \frac{2}{\pi} \tag{3.3.2}$$

assuming the linewidth is somewhat less than two times the limiting 100 kHz at which we could measure the relative frequency spectral density. This definition assumes that the (phase) noise is 'well-behaving' typically meaning that the noise does not contain coherent peaks. After carefully removing the smaller peaks by hand in the part of the spectrum covered by the integral, we estimate from the second saturated absorption measurement the locked laser linewidth to be no more than 64 kHz,[6] which indeed is much smaller than the 1.3 MHz cooling transition natural linewidth. The measurement of the frequency noise of the locking AOM's error signal shows most likely better the true frequency noise of the laser at higher frequencies and a similar calculation of the laser's linewidth using the red graph in figure 3.10(b) give 27 kHz.

[6]For frequencies higher than 10 kHz the phase spectral density of the second saturated absorption measurment follows a $1/f^4$ power law (usually known as 'random walk of frequency') and assuming this behavior continues at higher frequencies it makes the integral (3.3.2) above 100 kHz negligible and makes our estimation valid.

Chapter 4

Magneto-optical trapping of neutral mercury

When starting this project neutral mercury had never been laser-cooled before and only months before we succeeded in making a neutral mercury MOT the world's first neutral mercury MOT was made in a vapour cell [Hachisu et al., 2008]. We were the first ones to attempt to use a 2D-MOT scheme for trapping mercury atoms.

Mercury had rarely been used in a ultra-high vacuum and we did not have prior experience of working with mercury under such conditions. We therefore had to proceed carefully and test parts of the vacuum chamber in advance such as the source, the fused silica windows and how the different pumps would react under a mercury vapour pressure. Even after several preliminary tests it was uncertain how a relative high amount of mercury would react in a vacuum chamber over a period of many months and even now it remains to be seen how the really long-term behavior is.

When working on an atomic clock external magnetic fields is to be controlled to the best of ability. Again this has put a limit on vacuum chamber materials and parts.

Due to the lack of low-loss and reliable UV-fiber optics we did not have the luxury of using fibers to connect and mode-match the frequency doubling cavity output with the MOT. Due both to the nightly turn-off of the laser and the increasingly problematic BBO frequency doubling crystal we had to realign the MOT beam several times during a day. Fortunately by just touching one mirror close to the frequency doubling cavity output it was possible to a reasonable extent to realign the MOT beams and only on rare

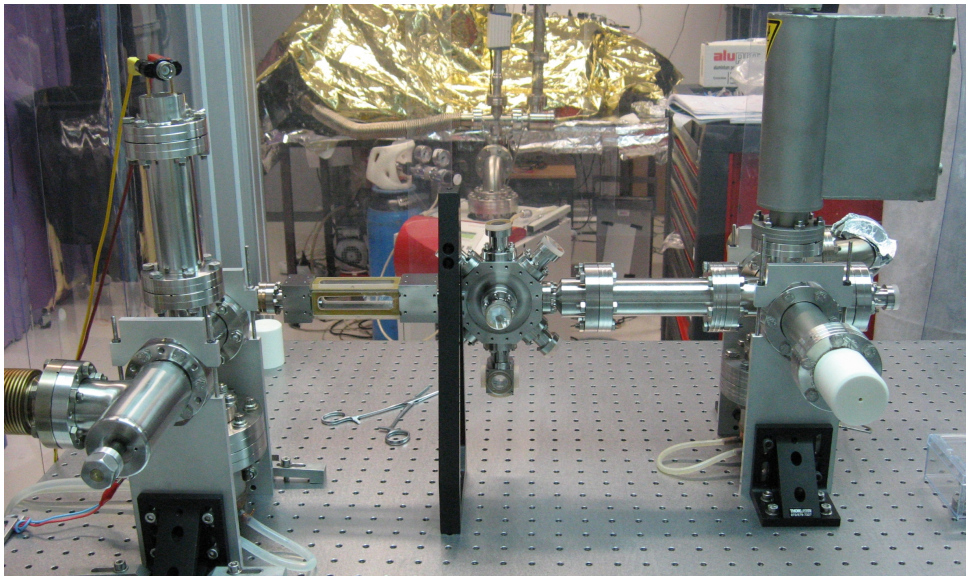

Figure 4.1: The vacuum chamber used for trapping and laser-cooling mercury atoms. To the left the source of mercury together with a getter pump. In the middle the 2D-MOT chamber followed by the actual MOT chamber. To the right a cold point pump, a getter pump and an ion pump.

rare occasions was it necessary to fully re-optimize. On top of this we had to deal with the increasingly damaged UV-optics (especially wave-plates) due to the harsh effect of the far-UV light.

A typical MOT only capture atoms from the tail end of the room-temperature atomic velocity distribution. To have a good clock performance we want both as many trapped atoms as possible and a long MOT lifetime. We therefore need to use a system for pre-selecting slower atoms. We chose to use a 2D-MOT for this both because a 2D-MOT is less cumbersome than a Zeeman-slower and can easier be compressed in size and because 2D-MOTs were already implemented in other labs at SYRTE and we therefore already had (positive) experience working with them. Compared with a Zeeman slower a 2D-MOT makes a much narrower atomic beam making it possible to include differential pumping thereby improving the background pressure of warm mercury atoms near the MOT.

4.1 Vacuum chamber and mercury source

We chose to build a two-part vacuum chamber for laser-cooling mercury (see figure 4.1) with differential pumping between the parts.

One part, the source part, is composed of a source of mercury vapour, the 2D-MOT and a getter pump which takes care of pumping impurities from the released mercury. This part of the vacuum chamber has a relatively high vapour pressure of mercury (typically $10^{-7} - 10^{-6}$ mbar) which loads the 2D-MOT.

The second part of the vacuum chamber is the MOT chamber (this is where all the laser-cooling, trapping and clock measurements will take place) connected with a getter pump, an ion pump and a cold point pump. This part is supposed to have a rather low background pressure so to allow a long MOT and dipole trapping lifetime. The MOT chamber is connected to the pumps through a narrow 16 mm wide about 4 cm long tube followed by a 20 cm long tube with an internal diameter of 4 cm giving an approximative total pumping speed of mercury of about 4 l/s (14 l/s for N_2) in the long thin tube approximation in the molecularly flow regime (See [Ramsey, 1985] for further details).[1] We expect the mercury to be pumped by the cold point pump while it is likely that a high vapour pressure of mercury could damage the ion pump. While the getter pump is included for pumping atomic species such as hydrogen and water typically found in vacuum chambers the ion pump takes care of the rare atomic gases such as helium and argon.

To avoid magnetism we use home-made titanium chambers for the central 2D-MOT and MOT chambers (including the custom-made pieces in between) while we use standard stainless steel vacuum parts for the rest. All windows are AR coated UV grade fused silica windows to allow the passing of the far UV light. Since the windows for the 2D-MOT are custom-made and we want to avoid magnetic components in all the window-assemblies for the MOT chamber we chose to glue the windows ourself using an airtight two-component Epotek H72 glue which degasses very little under vacuum. The glued pieces had to be heated up during the curing process and this could have posed a problem since fused silica has a thermal expansion coefficient of $5.5 \cdot 10^{-7}$ m/(m·K) (average from 20 °C to 320 °C)[2] and titanium[3] has a thermal expansion coefficient of more than a factor 10 higher ($8.5 \cdot 10^{-6}$

[1] This is for a room temperature mercury mean molecularly speed of 175 m/s.

[2] See for example http://www.sciner.com/Opticsland/FS.htm.

[3] All windows are glued onto titanium pieces.

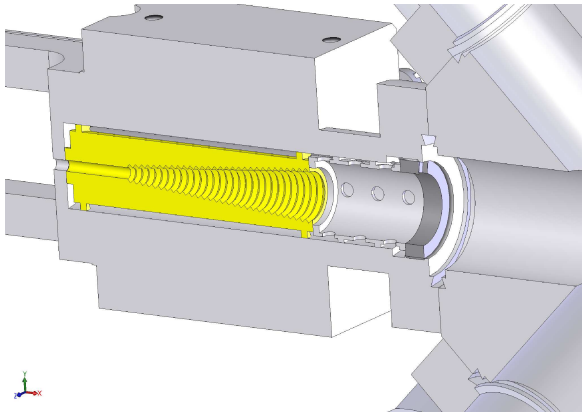

Figure 4.2: Differential pumping section (in yellow) between the 2D-MOT (to the left) and the MOT (to the right). A 1.5 mm wide 12 mm long hole ending in a threaded gold-coated conic output.

m/(m·K) [Lide, 1995]). By extending the heating period (> 24 hours) so we only had to heat the pieces up to 80°C and then let the temperature slowly decrease before opening the furnace, we managed to glue the windows without incidents. Apart from the 2D-MOT windows all windows are glued onto (titanium) pieces that easily can be detached from the rest of the vacuum chamber using regular CF16 flanges. This way in case of a problem with a leaking or damaged window it can easily be replaced and it is possible to easily replace a window with a different type of vacuum chamber part. The small separate detection chamber underneath the MOT chamber with windows on five sides is for detection of time-of-flight but have so far only been used for sending detection/clock beams into the MOT chamber. The top window on the MOT chamber is used for detection while the rest are used for the MOT beams. There are windows at each end of the vacuum chamber used for sending in a pushing beam for the 2D-MOT and for detection of background pressure in the 2D-MOT by absorption (see subchapter 4.2.1).

To be able to have different (background) pressures in the 2D-MOT and the main MOT chamber we installed the differential cooling section shown in figure 4.2 in-between the two chambers. A 1.5 mm wide 12 mm long hole sets a limiting pumping speed of about 15 ml/s (in the long thin tube approximation) for the thermalized background (mercury) atoms in the 2D-MOT chamber while atoms trapped by the 2D-MOT are being lead through the hole (possibly pushed by the pushing beam). The output side of the

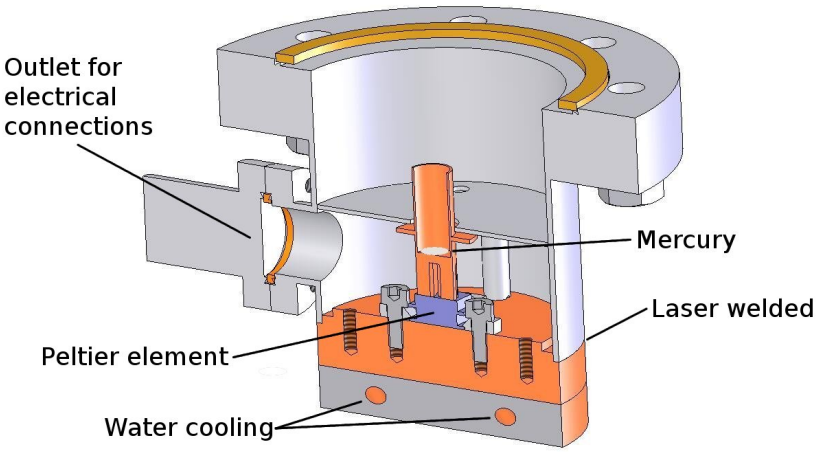

Figure 4.3: Setup for the source of mercury in the vacuum chamber. A few ml of mercury is placed inside the copper bowl which is glued onto a two-stage Peltier element (blue) also placed inside the vacuum chamber but shielded from the immediate vapour of mercury by an aluminium plate. The Peltier element is water cooled through the copper-element which it is fixed to. The small vacuum attachment on the side is for the electrical connection of the Peltier element.

hole is a threaded conical shaped coper piece coated with gold. Since gold and mercury creates an amalgam it is supposed that the mercury atoms will stick to the gold coating just as cesium or rubidium atoms stick to a graphite coating. The idea of the threaded cone is to catch as many fast atoms as possible to decrease the background pressure of mercury in the MOT chamber, while keeping the in-flux of slower atoms. There is a total of 7 cm between the 2D-MOT output and the center of the main MOT chamber.

Due to mercury's rather high vapour pressure ($2 \cdot 10^{-3}$ mbar at room temperature) it is not necessary to heat up the source material in an oven as is usually the case for many atomic species used in laser-cooling. We expect a somewhat lower vapour pressure around $10^{-6} - 10^{-7}$ mbar for optimal loading of the 2D-MOT. To have a controllable source of mercury that can be cooled down we are using the original setup shown in figure 4.3. A few drops of mercury[4] is placed inside a small copper container glued

[4]This mercury was not distillated like the one used for saturated absorption.

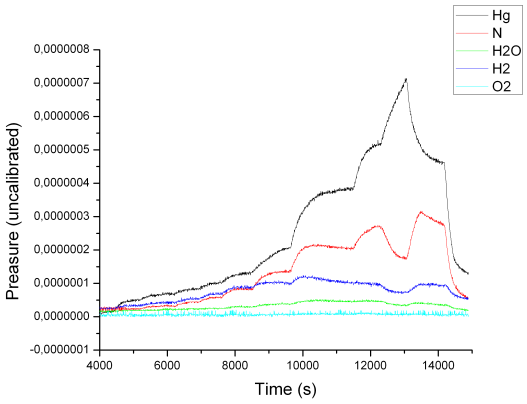

Figure 4.4: A mass spectrum analyzers measurement during a test of the mercury source in a smaller test chamber. These graphs shows the abundance of single isotopes. Due to the many mercury isotopes and the lesser efficiency of the measurements of heavier isotopes it is assumed that mercury is by far the most dominant atomic species. Near the peak of the mercury graph the spectrum analyzer is saturated by the mercury giving rise to the dip in the apparent abundance of the other atomic species.

(using Epotek H72) to the cold side of a two-stage Peltier element which (according to specifications) can produce a temperature difference between top and bottom of up to 80°C. The Peltier is fixed to a copper part water cooled to about 12°C enabling source temperatures down to almost −70°C at which the mercury vapour pressure is around 10^{-8} mbar. The Peltier element itself is inside the vacuum chamber to allow for better cooling but is shielded from the mercury vapour by an aluminium plate. There are holes through the fixing screws to allow pumping from the region underneath the plate. The electric connection of the Peltier is done through a commercial vacuum part. The so-called cold-point pump in the MOT-section of the vacuum chamber is of a similar design but with a 6-stage Peltier element and a larger cold copper part surface. According to specifications the 6-stage Peltier element can produce a temperature difference between top and bottom of up to 130°C.

Before assembling the final vacuum chamber we did a number of tests of the mercury source with a smaller section of the vacuum chamber containing only the mercury source, a getter pump and a (initially closed) valve leading to a turbo pump. The pressure in the chamber was monitored with

a TPG (Total Pressure Gauge) 300 pressure gauge while the atomic and isotopic composition of the gas was monitored with a mass spectrometer. For practical reasons those were connected with a 1 m long 4 cm wide tube (3 l/s of mercury pumping speed, 30 l/s hydrogen pumping speed) so their measurements could only be used as an indication and not as an actual pressure/isotopic abundance close to the source. Figure 4.4 shows a typical result of the tests given by the mass spectrometer. Notice that only one mercury isotope is being monitored. Those graphs are neither calibrated nor are the measurement efficiency of the spectrometer for different masses included. Figure 4.4 shows a situation where the source Peltier was initially driven at its maximum current of 2.11 A after the chamber had been pumped out with the turbo pump. With 5-10 minutes intervals the source current was slowly decreased. Nothing happened on the mass spectrum until reaching about 0.6 A. After this point, where the graph begins, the decrease in source current quickly shows itself as an increase in both mercury pressure and other more common molecular species. The unpurified mercury seems to contain some amount of nitrogen, hydrogen and water. At the top of the graphs where the source current is only 0.1 A the mercury starts saturating the mass spectrometer. Since mercury has several abundant isotopes (unlike hydrogen and others) and the spectrometer only measures one isotope the total mercury signal would be at least five times larger. We consider this sufficient proof that the gas is dominated by mercury. The source current is hereafter quickly re-increased showing an immediate decrease of pressure. These tests showed that the mercury source is working (showing pressures, most likely dominated by mercury, from the 10^{-8} mbar level up to at least $8.5 \cdot 10^{-5}$ mbar.) and apart form a certain amount of hysteresis when decreasing the mercury pressure, which is to be expected in a vacuum chamber, we can control the pressure of mercury in the chamber with this type of source.

4.2 Pre-selection of mercury atoms in a two-dimensional magneto-optical trap

The well known principle of trapping and cooling atoms in a magneto-optical trap (MOT) works on a $F = n \rightarrow F = n+1$ transition. In our case the 253.7 nm $^1S_0$ - $^3P_1$ cooling transition is a $F = 0 \rightarrow F = 1$ for the bosons, a $F =$

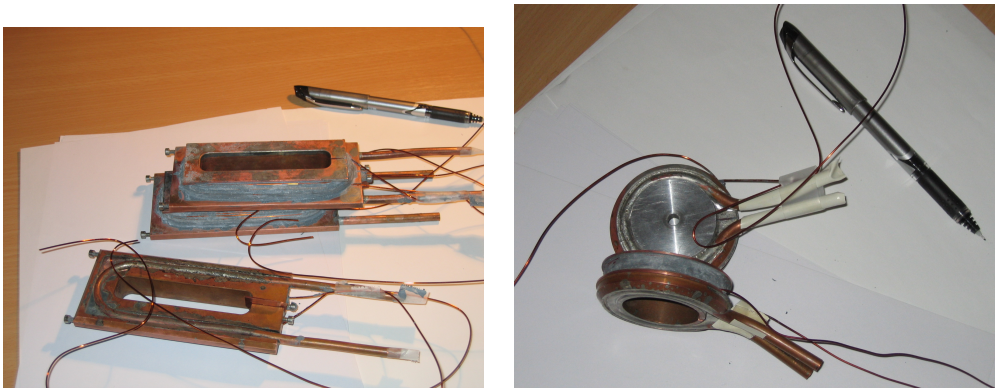

(a) (b)

Figure 4.5: (a) The coils used for the 2D-MOT. (b) The coils used for the 3D-MOT. For both types of coils the coil wires are cemented into a water-cooled copper element using a special cement-silica mixture.

$1/2 \rightarrow F = 3/2$ transition for the ^{199}Hg isotope and a $F = 3/2 \rightarrow F = 5/2$ transition for the ^{201}Hg isotope. In a MOT, each trap axis is composed of a magnetic field having opposite sign on opposite sides of the trap center and two counter-propagating beams having opposite circular polarization and with a frequency below the cooling transition (red-detuned). By choosing the correct sign of the magnetic field the excited state will split up in its Zeeman states such that the transitions to the lower Zeeman sub-states (which differs on each side of the MOT) will be closer to resonance with the inwards beam effectively pushing atoms towards the center and trapping atoms initially slow enough. Furthermore, close to the center where the Zeeman splitting is weak, the two counter-propagating beams laser-cool the atoms. The magneto-optical radiative force in a (one-dimensional) MOT is, to a good approximation, given by [Metcalf and van der Straten, 1999]

$$\vec{F} = \frac{\hbar\vec{k}\gamma}{2}\left(\frac{s_0}{1+s_0+(2\delta_+/\gamma)^2} - \frac{s_0}{1+s_0+(2\delta_-/\gamma)^2}\right) \tag{4.2.1}$$

where $\vec{k}$ is the wavevector of the cooling light, γ the transition natural linewidth (in units of angular frequencies) and $s_0 = I/I_{sat}$ the light intensity (of one beam) divided by the saturated intensity. $\delta_\pm$ is the detuning for each laser:

$$\delta_\pm = \delta \mp \vec{k}\cdot\vec{v} \pm \mu' B/\hbar. \tag{4.2.2}$$

δ is the lasers detuning from the transition frequency, $\vec{v}$ the atomic velocity and B the magnetic field strength. μ' is the cooling transition's effective magnetic moment $\mu' = (g_e M_e - g_g M_g)$ where $g_{e,g}$ is the Landé factor and $M_{e,g}$ is the magnetic quantum number (which designates the Zeeman sub-states) for the excited and ground state.

As mentioned earlier we use a two-dimensional version of a magneto-optical trap (2D-MOT) for pre-selecting slower atoms for the MOT chamber. Faster atoms will simply pass the 2D-MOT trapping region without being significantly slowed down while slower atoms will be trapped along a line centered in the 2D-MOT chamber. Imperfections in the magnetic field and the laser beams typically pushes the atoms either towards or away from the MOT chamber. A (weak) push beam at the cooling transition frequency is sent in along the 2D-MOT to push the atoms towards the MOT chamber. In our case the push beam did not seem to have any effect and we assume that the imperfections in the magnetic field and laser beams already pushes the atoms towards the MOT chamber.

The magnetic field is created by four elongated coils (shown in figure 4.5(a)) mounted along the 2D-MOT chamber which effectively creates a 2D-quadrupole field in the center. Each coil has about 70 windings of isolated 1 mm copper wire cemented into a copper mounting at an approximate distance of 27 mm from the 2D-MOT center. To increase thermal conductivity and electrical isolation we used a 50/50 mixture (by weight) of cement and silicon-carbide powder. The coil mounts are water-cooled (12°C) since we expected the need for a current of almost 10 A although so far the optimum has been much less. The light is lead in through the side and the bottom of the chamber and then retro-reflected by mirrors back through a quarter-wave plate all mounted on a custom-made mounting-plate fixed to the chamber itself (see figure 4.11). The coils are driven at a current of 2.2 A which corresponds to a magnetic field gradient near the center of the 2D-MOT of about 20 G/cm.

Preliminary simulations of a mercury 2D-MOT (see further down) and experience with using other atomic species (such as Rb and Cs) in a 2D-MOT have indicated that it would be optimal to have a beam which is rather elongated along the direction of atomic propagation (along the 2D-MOT chamber). We had planed to use two beams on each side, all having a 2:1 beam waist ratio. But due to problems related to a faulty delivery of cylindrical lenses we have so far been limited to using a single slightly flat

beam ($1/e^2$ beam waist of about 3.9 mm times 5.1 mm) on each side.

The optimization of the 2D-MOT (magnetic field, beam alignment, pushing beam, power ratio between MOT and 2D-MOT and to some extent polarization) was done by measuring the fluorescence of the actual MOT (see subchapter 4.3).

4.2.1 Measuring background mercury pressure by absorption

At times it is important to know the mercury vapour pressure in the 2D-MOT chamber. We obtain this by measuring the absorption of a weak beam (typically a couple of hundred nW) sent horizontally across the whole vacuum chamber. The beam is sent through both the 2D-MOT chamber and the regular MOT chamber and it is assumed that the pressure in the regular MOT chamber is negligible compared with the 2D-MOT chamber. By scanning the laser frequency around the cooling transition of a (known) isotope it was possible to find the absorption at resonance and at a frequency a couple of pm from the resonance. Comparison of the absorption of the beam at those two frequencies gave the relative absorption from presence of atoms in the chamber.

The absorption of a beam of intensity I along a direction z due to atoms of a certain velocity class (along z) is given by [Metcalf and van der Straten, 1999]

$$\frac{\mathrm{d}I}{\mathrm{d}z} = -h\nu\gamma_p n \tag{4.2.3}$$

with ν being the light frequency, n the (homogenous) density of atoms and γ_p the scattering rate of a single atom

$$\gamma_p = \frac{\gamma}{2}\frac{I/I_{sat}}{1 + s_0 + (2\delta/\gamma)^2} \tag{4.2.4}$$

where, in the case of a laser on resonance, δ is the Doppler shift $-k \cdot v_z$ due to the atoms velocity v_z along z. It is assumed that the atoms velocity along the beam direction is distributed according to the Maxwell-Boltzmann distribution:

$$p(v_z) = \sqrt{\frac{m}{2\pi k_B T}} e^{-mv_z^2/2k_B T} \tag{4.2.5}$$

where we assume room temperature $T = 300$ K. It can be assumed that the beam intensity is much lower than the saturation intensity ($I \ll I_{sat}$) and

equation (4.2.3) can then be written as

$$\frac{\mathrm{d}I}{\mathrm{d}z} = -\frac{\sigma}{k_B T} pI \tag{4.2.6}$$

with isotopic pressure $p = nk_BT$ (assuming an ideal gas) and

$$\sigma = h\nu \frac{\gamma}{2I_{sat}} \sqrt{\frac{m}{2\pi k_B T}} \int_{-\infty}^{\infty} \frac{1}{1 + (2k \cdot v_z/\gamma)^2} e^{-mv_z^2/2k_BT} \mathrm{d}v_z \tag{4.2.7}$$

where the integral can be solved numerically. The solution is then

$$I(z) = I_0 e^{-\frac{\sigma}{k_B T} pz} \tag{4.2.8}$$

which may be more useable in the form

$$p = -\frac{\ln(1 - A_r)}{\sigma z}, \tag{4.2.9}$$

where $A_r = 1 - I/I_0$ is the typical measured quantity namely the relative absorption.

In our case σ/k_BT is approximately 13900 $\mathrm{Pa}^{-1}\mathrm{m}^{-1}$ around room temperature and z is 24 cm not counting the MOT part and differential pumping stage in the vacuum chamber due to rather low pressure there (the path travelled by the beam in those low-pressure regions is of comparable length).

Figure 4.6 shows the expected relative absorption of a beam at the most abundant isotopes cooling transitions resonance frequency as a function of the background pressure of mercury through the 24 cm vacuum chamber. The reason for including this is to show the necessary intensity (or power) noise-level needed to measure the pressure. At for example a mercury pressure of 10^{-7} mbar it is necessary to have a relative intensity noise less than 10^{-2} and preferably better than 10^{-3} to make a decent measurement.

The typical level of the relative intensity noise of the cooling light measured with a dynamic signal analyzer was about $10^{-2}/\sqrt{\mathrm{Hz}}$ at 1 Hz sometimes even worse.[5] To achieve a better intensity noise we set up a power-lock using an (182.5 MHz) AOM, a 20 μm pinhole to have a better spatial mode and a reference photodiode. Electronically a DC signal is subtracted from the photo-diode signal to get the signal sufficiently close to zero and after an integrator filter it is fed into the AOM's power control which then stabilizes the beam power level with the AOM. It was possible to tune the

[5]This was only measured on the auxiliary beam used, among other things, for locking the laser. We used a small part of this beam for the purpose of absorption measurements.

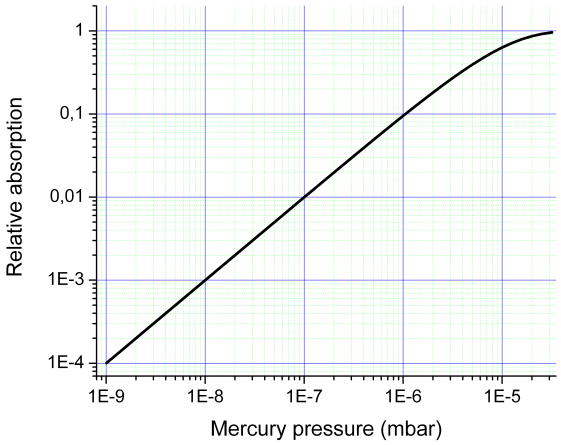

Figure 4.6: Calculated relative absorption of a (weak) beam of light at the ^{202}Hg cooling transition resonance as a function of the total mercury pressure.

AOM's frequency with the VCO. Figure 4.7 shows a measurement of the relative intensity noise of the absorption photo-diode signal. A low-pass filter (not included in the measurement) removes the higher frequency noise. Assuming the need of a slow modulation ($\approx$ 10 Hz) which we don't want to filter we are interested in the noise for frequencies in the 10-100 Hz range. The graphs in figure 4.7 shows that the power lock clearly improves the intensity noise for those frequencies and that we have obtained a relative intensity noise of no more than -70 dB/Hz ($\approx 3 \cdot 10^{-4}/\sqrt{\text{Hz}}$) which gave us the possibility of measuring a background pressure of less then 10^{-8} mbar.

To obtain this level of efficiency it was necessary to pay attention to the noise sources which differentiates the references photo-diode from the absorption photodiode. The background light is an obvious source that was dealt with by gluing metal tubes to the photodiode casings. Another one is obviously noise induced to the beam in-between the two photo-diodes. Therefore it is important to avoid any kind of beam chopping. The biggest problem was the stability of a mirror mounted 18 cm above the table followed by a more than 50 cm trajectory across the vacuum chamber to a photodiode only a couple of mm wide. In the end the mirror was mounted on a several cm thick metal rod screwed directly into the optic table. This is still considered the limiting factor of this power lock.

We chose to start out with a background mercury pressure of about

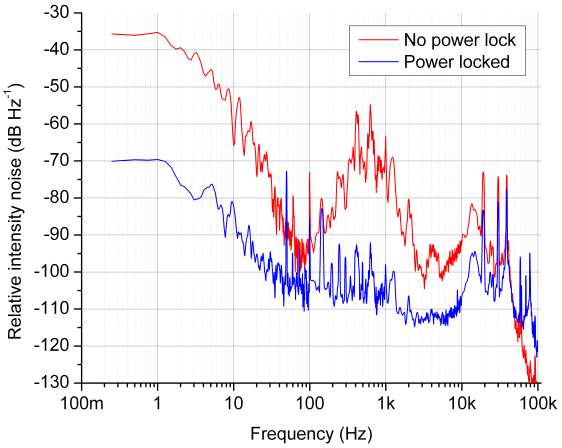

Figure 4.7: The relative intensity noise measured by a dynamic signal analyzer on a photo-diode measuring the absorption through the vacuum chamber. The power lock has a bandwidth of about 20 kHz mostly limited by the photodiode.

$2 \cdot 10^{-7}$ mbar. We have observed the same kind of hysteresis of the mercury vapour pressure as was seen during the preliminary tests of the mercury source.

4.2.2 Modelling the flux of slow atoms from the 2D-MOT

We have used a Monte Carlo simulation of (mercury) atoms in a 2D-MOT similar to the one reported in [Wohlleben et al., 2001] to estimate the atomic output and the optimal requirements for the magnetic field gradient and beam configuration. The simulation finds the trajectories of $10^7 - 10^9$ atoms through the 2D-MOT. Each trajectory is found by solving Newton's equations along the trajectory for a force given by (4.2.1) along two directions plus a constant field of gravity (along one of the aforementioned directions). The simulation uses the embedded fourth order Runge-Kutta method for solving the particle movement in auto-adaptive time steps small enough to give a solution to the equation of motion with a chosen relative error of 10^{-8}.

The initial positions of atoms are randomly picked from the walls of the 2D-MOT chamber (except the end wall in which the atoms exits) as

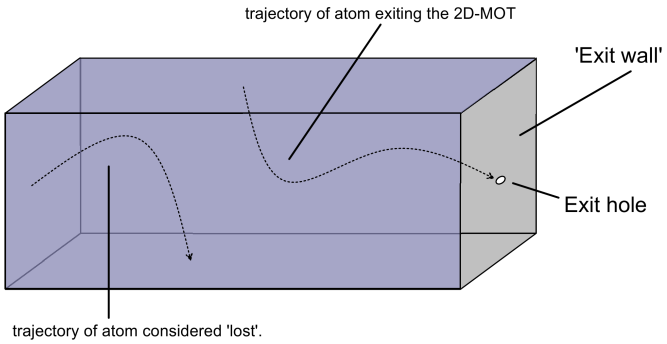

Figure 4.8: Diagram showing the model used for the 2D-MOT simulation. The atoms are randomly picked from the walls (in blue) except the 'exit wall'. If the simulation calculates that a certain atom crosses a wall or the 'exit wall' outside the exit hole the atom is considered lost.

shown in figure 4.8 using a flat distribution function. Their initial velocities parallel to the wall chosen as starting point for the particular atom are randomly picked from a gaussian velocity distribution corresponding to a 300 K Maxwell-Boltzmann distribution:[6]

$$e^{-mv^2/2k_BT}, \tag{4.2.10}$$

where v is the velocity (in one direction), m the atomic mass, k_B Boltzmann's constant and T the temperature.

We wanted to estimate the flux of atoms exiting the 2D-MOT chamber (or which enters the MOT capture region) so for picking the velocity perpendicular to the wall we used the distribution corresponding to the flux of atoms passing through when the atoms velocities are distributed according to the 300 K Maxwell-Boltzmann distribution (see appendix A):

$$\frac{P}{k_BT} v e^{-mv^2/k_BT}. \tag{4.2.11}$$

By calculating enough atomic trajectories through the 2D-MOT the flux of exiting atoms is given by the fraction of trajectories leading out of the 2D-MOT chamber multiplied by a proper normalization factor. The normalization factor is the total incoming flux given by (see appendix A)

$$A \cdot \sqrt{\frac{1}{2\pi m k_BT}}, \tag{4.2.12}$$

[6] There is no normalization constant since we are using the normalized integral function to pick the velocities.

where A is the area of the walls which makes up the initial positions of the atoms.

The reasons we can just pick atoms originating from the walls are the following: the atoms trapped by the 2D-MOT are taken from a room temperature background pressure of mercury in the chamber. It is assumed that only the slowest atoms (the tail end of the velocity distribution) can be trapped and therefore the atoms removed by the 2D-MOT effectively doesn't change the background pressure and there is a constant redistribution of atomic velocities when atoms collide with the walls (and with each other). At the background pressure of $2 \cdot 10^{-7}$ mbar the mean free path[7] is of more than the length of the MOT chamber and we assume that the atoms in the 2D-MOT are in the molecular regime where it is most likely that an atom can travel between two wall collisions without colliding with another atom. This is of course not the case for the slower atoms but we assume that a collision with another atom means that the slow atom is sped up (since most atoms in the chamber are faster) such that it can no longer be considered slow enough to be captured and we consider it a loss in our model. We therefore assume that all atoms that are trapped by the 2D-MOT are atoms which last collision was with a wall and not with another atom and that the collisions between atoms and wall effectively redistribute (or re-thermalize) the atomic velocities to a Maxwell-Boltzmann distribution corresponding to the wall's temperature (~ 300 K).

We consider atoms 'lost' from the 2D-MOT if they either reach a wall, moves away from the exit wall or ends at the exit wall without being within the 1.5 mm wide exit hole. Any atom making it through the exit hole also has to make it through 1 cm of a 1.5 mm wide tube and then make it to the couple of cm wide MOT capture region 6 cm into the MOT chamber in both cases under the influence of just gravity. The movement through those are not simulated using the Runge-Kutta method but simply calculated (again using Newton's second law) since there is only the simple gravitational force to account for. To save computer time we initially remove atoms that we consider too fast to be captured ($|\mathbf{v}| > 40$ m/s).

We introduce collisional losses by multiplying the atomic count (which otherwise would be one for each atom making it through and zero for every other atom) with an exponential function $e^{-t\zeta p}$ where t is the amount of

[7]The average mean free path of air molecules at this pressure is several hundred meters.

time spent in the MOT-chamber[8], p the mercury pressure[9] in the 2D-MOT chamber and ζ is the atomic collision rate between mercury atoms per units of pressure. We have used $\zeta = 4 \cdot 10^6$ $s^{-1}Pa^{-1}$ which is the value obtained from the mercury MOT loss-rate assuming a background pressure of 10^{-9} mbar in the MOT-chamber (see next subchapter for further details).

Initially we tested the model against results obtained on the Rb 2D-MOT on the FO2 fountain experiment here at SYRTE. Those showed that the simulation best copied the experimental results if we bluntly divided the MOT force by three.

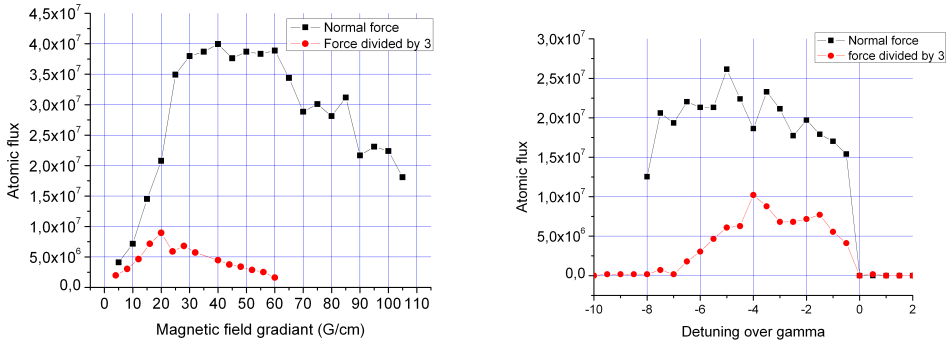

(a) (b)

Figure 4.9: (The flux of atoms in the main MOT chamber as a result of the 2D-MOT simulation when using a single beam region in the present 2D-MOT configuration as a function of (a) the magnetic field gradient and (b) the laser detuning divided by the cooling transition natural line width. Those are for a total laser power of 100 mW shown for both the regular MOT force and the MOT force divided by 3.

In our experiment we can use the number of atoms in the MOT as an approximate measure of the number of atoms getting through the 2D-MOT. Since we so far have used a single 2D-MOT beam (in each direction) in the mercury 2D-MOT we have first modelled this beam configuration approximating the beam shape used. The result of the simulation, using a total laser power of 100 mW, a beam waist of 3.9 mm along the 2D-MOT

[8] We consider the collision possibility in the exit tube and in the regular MOT chamber negligible due to a much lower background pressure.

[9] As earlier tests of the mercury source has indicated we assume the pressure is dominated by the mercury.

and a 5.1 mm beam waist along the two other directions, is shown in figure 4.9 both for the regular MOT force and for the force divided by three. Since for that configuration it seemed that a magnetic field gradient of about 20 G/cm and a detuning of about -6 times the natural line width was optimal it seems that the 'divide by three' model best models the actual results. From loading time and the measured number of atoms in the MOT the flux of atoms should lie in the low 10^6 which also seems best modelled when dividing the force by three.

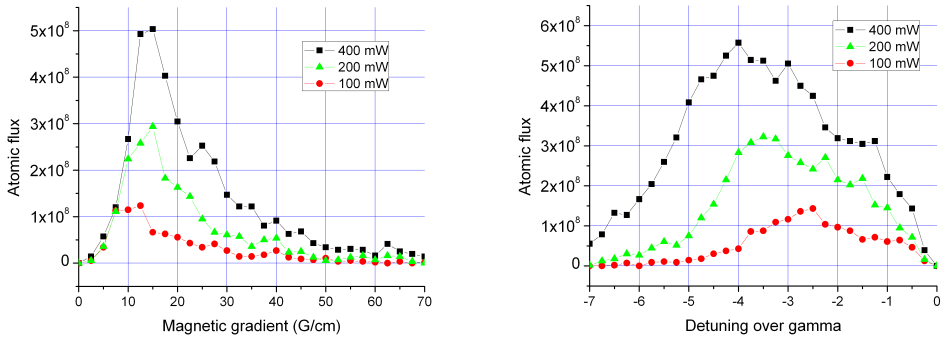

(a) (b)

Figure 4.10: The 2D-MOT simulation result for a 2D-MOT with two capture beam regions for different total laser powers as a function of (a) the magnetic field gradient and (b) the laser detuning divided by the cooling transition natural line width.

Experience with 2D-MOT's on other species and simulations have shown that it is better to spread out the laser power by for example having several 2D-MOT beam regions. Figure 4.10 shows the result of the simulation when using two 2D-MOT beams in both directions using the MOT force divided by three for different total laser powers. Notice that for the same power as in the aforementioned situation there are more atoms getting captured and that the optimal magnetic gradient is strongly dependent on the total lasing power while the detuning is less so. Compared with the single beam region case this double beam region case has both a lower optimal magnetic gradient and lower optimal detuning.

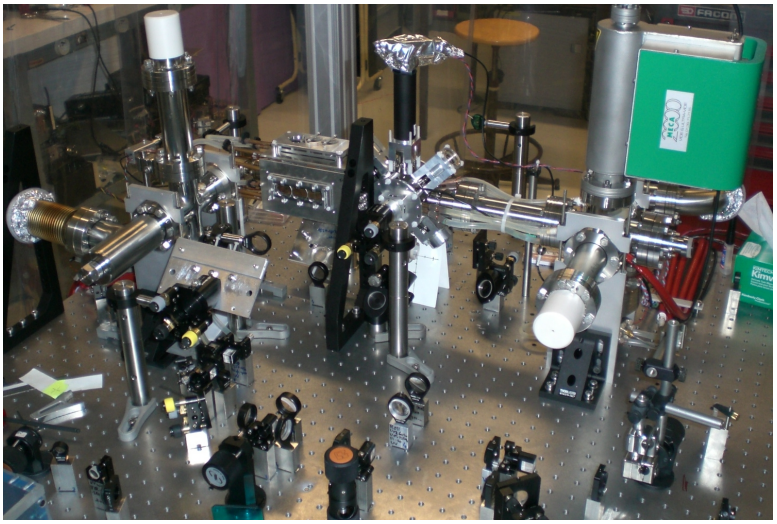

Figure 4.11: The vacuum chamber including coils and optics for 2D-MOT and MOT.

4.3 The magneto-optical trap

As described in a former sub-chapter a MOT requires a circular polarized laser source and a quadrupole magnetic field. Three slightly converging beams with an approximate $(1/e^2)$ waist of 3.3 mm were sent into the 16 mm wide main MOT chamber horizontally and from two 45° angles from below all retro-reflected from external mirrors mounted onto the vacuum chamber itself just as for the 2D-MOT.

Two 63 mm wide[10] coil mounts (shown in figure 4.5(b)) are mounted directly onto the MOT chamber such that there is only about 15.5 mm between the coils and the center of the MOT chamber. The magnetic field from the two coils is effectively a quadrupole field near the center with gradients given by[11]

$$\Delta B_{\text{along coil axis}} \approx 3\mu_0 I \frac{Ra^2}{(a^2+R^2)^{5/2}} \tag{4.3.1}$$

[10] The average diameter of the coils are 52.5 mm.

[11] This is assuming equal counter-propagating currents in the coils. These equations are deduced from the $a^2r^2sin^2\theta/(a^2+r^2)$ expansion of the magnetic field around a circular current loop (in spherical coordinates) close to the midpoint between two loops in the near axis limit (see [Jackson, 1999]). The second equation is also evident from the first one due to $\nabla \cdot \mathbf{B} = 0$ and symmetry.

$$\Delta B_{\text{perpendicular to coil axis}} \approx \frac{3}{2}\mu_0 I \frac{Ra^2}{(a^2+R^2)^{5/2}} \tag{4.3.2}$$

with a being the coil radius, R half the distance between the coils and I the total current around one coil. So far about 1.7 A is the optimized current in the coils which both have 56 windings leading to an approximate field gradient of 15 G/cm along the coil axes and a 7.5 G/cm field gradient in directions perpendicular to the coil axes.

For certain type of measurements (absorption, time-of-flight and clock operation) it is necessary to switch off the MOT so quick that the atoms haven't left the trapping region before the MOT is completely gone and in such a way that the switching process doesn't perturb the atoms. We have chosen to be able to switch both the MOT light and the magnetic field.

For switching the light we use a mirror mounted on a galvo (galvanometer) used on the main beam just after the doubling cavity where the light has a small waist. This switches both the MOT-light and the 2D-MOT light at the same time. Switching off the beam has a delay of 1.06 ms with a switching time-constant of 89 μs, while switching it on has a delay of 1.46 ms with a time-constant of 122 μs.

To be able to switch the magnetic field fast enough we used a (IRFIZ-44N) MOSFET transistor on the coil circuit, which can easily handle 10 A at 30 V (although an effective heat dissipator is needed for that kind of power), to remotely switch the coil current. Switching the current has a time-constant of about 10 μs with a delay of about 30 μs. The corresponding switching time of the magnetic field was measured through the induction of the magnetic field in an external coil and this gave a switching time-constant of about 100 μs.

Initially we used the fluorescence from the MOT for detection and optimization. On top of the main MOT chamber a 50 mm focal length half inch diameter lens placed 100 mm from the center of the chamber focalized 0.08 % of the MOT fluorescence onto a high gain silicon photodiode whose signal afterwards was amplified by a factor of 100. The typical loading curve like the one shown in figure 4.12(a), when switching the MOT's magnetic field, shows the presence of a MOT.

The number of atoms in a MOT N can be described by a standard rate equation [Gibble et al., 1992]:

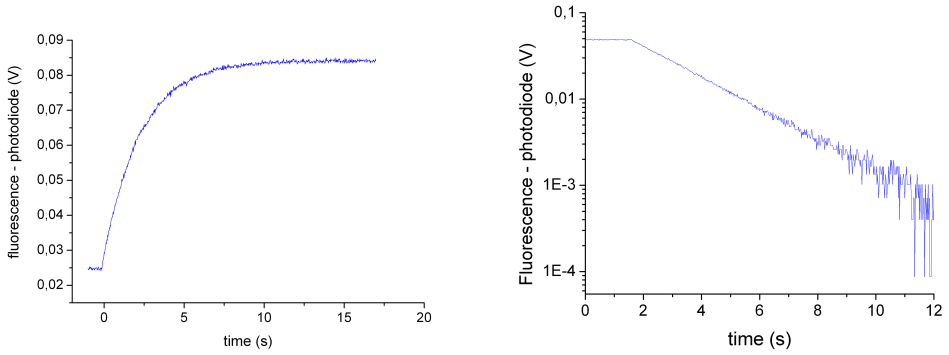

(a) (b)

Figure 4.12: (a) The fluorescence of the ^{202}Hg MOT while being loaded. The graph indicates a typical loading time of about 2.3 s. (b) The fluorescence of the ^{202}Hg MOT while it being unloaded due to the 2D-MOT's magnetic field being turned off. This indicates a typical lifetime of 2.4 s.

$$\frac{\partial N}{\partial t} = R - \Gamma N \tag{4.3.3}$$

where R is the rate at which atoms are being trapped in the MOT and Γ the loss-rate which in the case of a MOT is assumed to be dominated by collisions with non-trapped atoms. The solutions in case of either $N(0) = 0$ or $R = 0$, which corresponds to respectively loading and de-loading of a MOT, are of the form $A(1 - e^{-t/\tau})$ and $Be^{-t/\tau}$. If indeed the loss of atoms in the MOT is due to not only collisions with non-trapped atoms but also partly due to collisions between trapped atoms, the loss-rate will depend on the density in the MOT and an additional term should be added to (4.3.3).

The loading time of our MOT given by the fluorescence graph in figure 4.12(a) is 2.3 s. This is an indication of a rather low background pressure. By measuring the MOT's fluorescence after the magnetic field of the 2D-MOT has been turned off it was possible to measure the fluorescence of the (partial) de-loading of the MOT as can be seen in figure 4.12(b). First and foremost this shows that the 2D-MOT indeed has an effect on the number of atoms and from the linear-scaled graph it was possible to see that in that particular setup at least 80 % of the trapped atoms were due to the 2D-MOT. The decay time (or life-time) is about 2.4 s and as expected is comparable with the loading time. The exponential scaled graph shows a

straight line which indicates that there are negligible loses due to collisions amongst trapped atoms.

Assuming we know the background pressure in the MOT-chamber and that it is mostly composed of mercury, it is possible to estimate the (average) collision cross section between a trapped ^{202}Hg atom and a random non-trapped mercury atom. Under these circumstances the collision rate for the trapped atoms are given by

$$\Gamma_c = n\sigma_c\bar{v} = p\sigma_c\sqrt{\frac{8}{\pi m k_B T}} \tag{4.3.4}$$

with n being the density of background (mercury) atoms, σ_c the collision cross section for collisions where the atom gets ejected from the trap $\bar{v}$ the average speed. Using the 2.4 s life-time and a background pressure of 3-4 times the 10^{-9} mbar measured by the ion pump, we can very roughly estimate an upper bound of the mercury collision rate per unit of pressure $\Gamma = 3 \cdot 10^{-13}$ cm^2, which is used in the aforementioned 2D-MOT simulation. Using this value simulations of the 2D-MOT have shown that collisions is not an issue for the levels of pressures we are working at.

From the MOT fluorescence it is possible to estimate the number of atoms in the MOT which, together with the temperature of the trapped atoms, is one of the important parameters for the future transfer of atoms into the dipole trap and the final lattice clock. The number of atoms in the MOT is calculated by dividing the total flux of fluorescence photons by the (average) scattering rate for the atoms. Assuming an isotropic fluorescence, the photon flux is simply given by our measurement, knowing the spatial angle covered by the capture lens, the photon energy (or frequency) and the photodiodes sensitivity and gain. The scattering rate γ_p is given by [Metcalf and van der Straten, 1999]

$$\gamma_p = \frac{\gamma}{2}\frac{s_0}{1 + s_0 + (2\delta/\gamma)^2}, \tag{4.3.5}$$

where $s_0 = I/I_{sat}$ is the total light intensity in the trap divided by the saturation intensity and δ the laser's detuning from the cooling transition resonance. When doing the MOT represented in figure 4.12 using ^{202}Hg, the isotope we worked on to begin with, we had about 220 mW after the beam shaping with about 128 mW (58 %) being used for the 2D-MOT. The detuning was about -8.5 MHz (-6.5γ) and the magnetic field gradients were about 23 G/cm for the 2D-MOT and 15 G/cm for the MOT (along

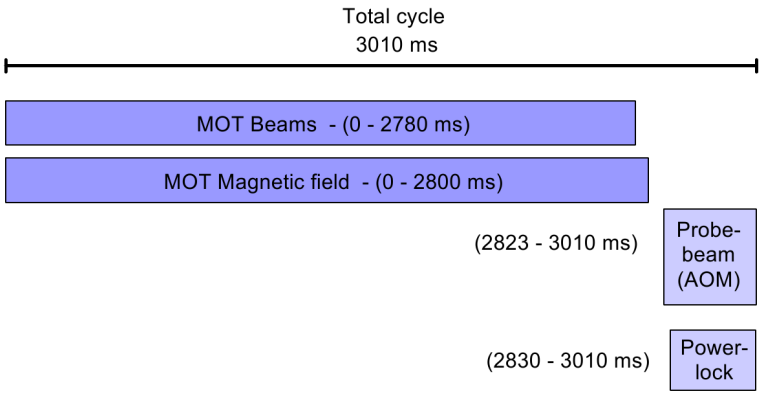

Figure 4.13: The time table for the measurement cycle when measuring the absorption of a probe beam sent through the MOT.

coil axes). The number of atoms were estimated to be about $4.7 \cdot 10^6$. Unfortunately we could not keep using this amount of power (see chapter 3) and we chose to optimize the MOT for a total cooling power of about 110 mW and a detuning of -5.5 MHz.

A second measurement method based on absorption was used to confirm the atom number. To do this we used the power locked probe beam first used for detecting the background pressure in the 2D-MOT chamber. The beam was directed under the main MOT chamber where it was reflected vertically up through the chamber. To begin with a mirror mounted on top of the chamber redirected the light onto a horizontal high gain photodiode. To initially align this probe beam through the MOT we looked directly at the MOT fluorescence with a UV viewer while switching the probe light (with the power lock AOM) to see whether the MOT was slightly pushed to one side due to the probe beam.

While the MOT light is on, the transition gets highly saturated biasing the absorption of the probe beam. To be able to measure the absorption we use a computer-controlled sequence in which the MOT beams are turned off for a short moment while the absorption is measured. The approximately 3.01 s long sequence was controlled by data acquisition cards able to time output signals and data recordings with a precision below 100 μs. We added a home-made board to better distribute the signals and buffer recorded data.

The details of the measurement cycle is shown in figure 4.13. The MOT was on for about 2.8 s so to be sure that a MOT was completely reloaded when turning the MOT fields off since the trapped atoms easily left the

MOT region during the remaining 200 ms. At the same time we let the probe beam off so not to disturb the MOT as could be seen when observing the MOT in a UV viewer when switching the probe beam. The MOT magnetic field was also turned off when the MOT beams were off so not to magnetically push the atoms away and to avoid unnecessary Zeeman shifts. The probe beam was switched with the power-lock AOM and we switched the power-lock integrator so to reset it when the probe beam had been turned on.

Figure 4.14(a) is a good example of what is observed around the time when the MOT is turned off during the measurement sequence. After the probe beam has been turned on there is a clear absorption of light from atoms that have been trapped in the MOT. We also clearly see how the atoms leaves the probe beam which in this situation had a $(1/e^2)$-width of 140 μm and was assumed to be smaller than the MOT. Due to the small size of the beam the atoms are leaving the beam region so fast it is far from clear what the maximum absorption is in this situation. But by estimating the absorption the exact moment the MOT was turned off we can estimate the density of atoms in the central part of the MOT.

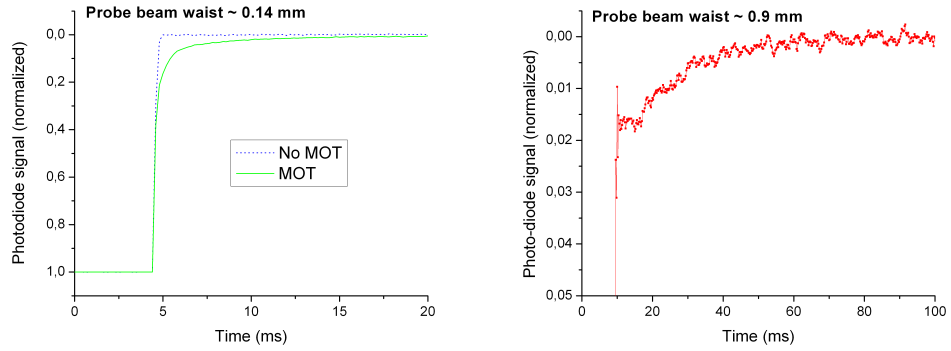

(a) (b)

Figure 4.14: (a) Graphs showing the measurement of the probe beam (smaller than the MOT) sent through the MOT (green) during the switch-off of the MOT in the absorption measurement cycle (see figure 4.13) compared with a situation where the magnetic field of the MOT stayed off and no atoms were trapped (blue). The absorption of formerly trapped atoms falling out of the probe beam is clearly visible. (b) A similar measurement with the probe beam being larger than the MOT. The flat part lasts 7 ms.

The calculation done in sub-chapter 4.2.1 of the absorption of on-resonant light due to the presence of a background pressure is only valid if the atomic (or rather isotopic) density n is homogenous across the beams width. Assuming a probe beam small enough so this is the case we have

$$I = I_0 e^{-\sigma n z}, \tag{4.3.6}$$

where z is the distance in which the light interacts with the atoms, that is the width of the MOT which typically is of the order of 1 mm. σ is still given by (4.2.7) and if $(2k \cdot v_z/\gamma)^2 \ll 1$ for most velocities we have the well-known result

$$\sigma \approx \frac{3\lambda^2}{2\pi}. \tag{4.3.7}$$

In our case this is barely true since $(2k \cdot v_{rms}/\gamma)^2 \approx 0.13$ at the expected Doppler temperature. I will use this anyhow[12] since this is a rough estimate of the atomic density and to avoid dealing with the unknown temperature of the atoms. In all cases we are limited by the unsure estimation of the absorption when dealing with a beam smaller than the MOT.

To estimate the absorption from figure 4.14(a) we can just pick the point where the two measurements starts to be different which is around 0.3 (corresponding to a relative absorption of 30 % due to the normalized scale).

In figure 4.14(b) the beam is larger than the MOT and it takes some time (7 ms) before the atoms starts leaving the region covered by the probe beam and it is therefore much easier to deduce the absorption when the moment MOT was turned off. By having a probe beam such that it encompasses the MOT we can effectively measure the total number of atoms.

The size of the beam was changed by inserting a 200 mm focal lens approximately 475-635 mm from the MOT.[13] This is important to notice since the beam in those cases was not perfectly parallel (although we consider the effect rather small).

We can roughly estimate the number N of atoms covered by the probe beam and consequently, if the beam is wide enough, in the whole MOT from equation (4.3.6) by ignoring how the atoms are distributed in the

[12] At the 31 μK Doppler temperature this gives a 4 % difference.

[13] Beam size measurements were done by reflecting the beam before it entered the vacuum chamber and then do the measurement at a distance comparable with the distance to the MOT.

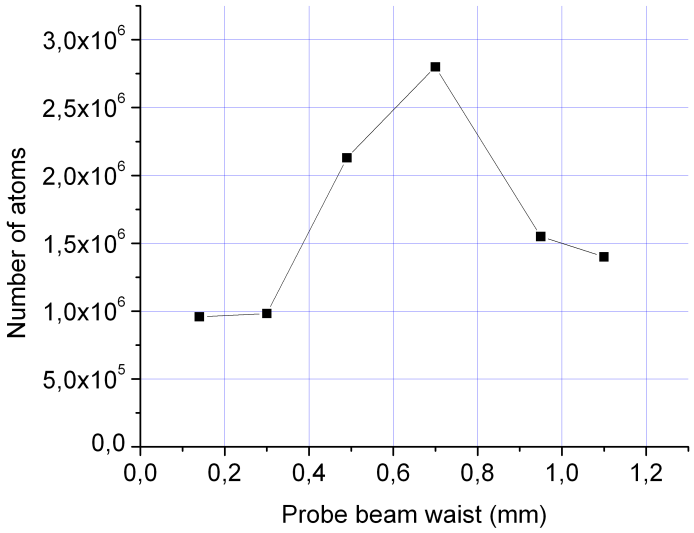

Figure 4.15: The estimated number of MOT atoms within the probe beam width as a function of the beam waist.

MOT (which we do not have the knowledge of):

$$N = -\frac{\ln(1 - A_r)}{\sigma} \cdot (\pi \cdot w^2) \tag{4.3.8}$$

where A_r is the relative absorption measured and w the probe beam's waist. Figure 4.15 shows the estimated number of atoms within the probe beam as a function of the probe beam size. For smaller beam sizes it is expected to have a smaller number of atoms since the probe beam detects less of the atoms and there might be saturation effects. At higher beam waists the measured number of atoms is supposed to stabilize. The most likely reason for the decrease in the number of atoms at higher beam waists might come from the fact that we could not do the measurement under the same lasing conditions and that the MOT itself might not have contained the same number of atoms. Due to the increasingly bad frequency doubling crystal which made us often change the MOT beam alignment and the worsening UV optics (especially the doubling cavity output coupler) we were far from sure to have a MOT with about the same number of atoms. The graph in figure 4.15 seems to indicate that we at have obtained near 3 million atoms in the MOT with a total input power (for both MOT and 2D-MOT) of 125 mW. This can be compared with fluorescence based measurements made at

about the same cooling lasing power giving estimated 1-3 million atoms.

Figure 4.16 shows measurements of the number of atoms as a function of the probe beam detuning obtained by absorption using equation (4.2.7) for obtaining σ. With a probe power of about 720 μW for the measurements with the probe beam waist of 0.3 mm and about half of that for the measurements with the 0.5 mm probe beam waist the probe beam is far below the saturating intensity of the transition. Saturation of the transition does not explain the apparent dip in measured absorption near zero detuning. Measurements made at two different probe beam powers (one half of the other) on the same MOT have also not shown any difference. Notice the difference between the atomic number of the two measurements made on two different MOT's on two different days. A florescence measurement of the number of atoms made a few days earlier gave an atom number of about $1 \cdot 10^6$ atoms. The measurements of the number of atoms by fluorescence and by absorption coincide within a factor of two or three.

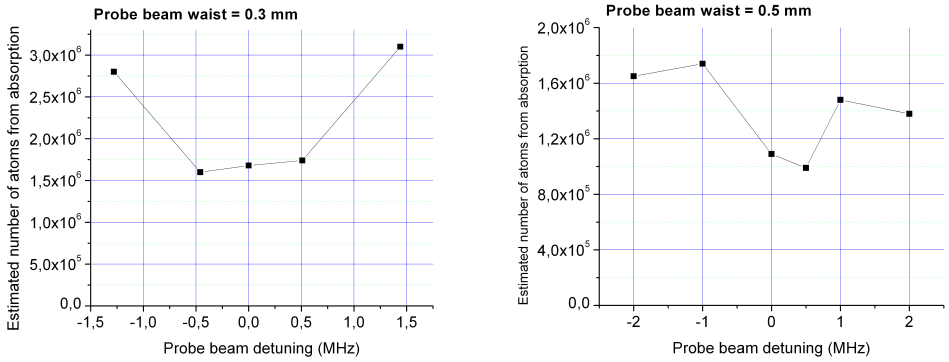

(a) (b)

Figure 4.16: The number of atoms estimated from absorption as a function of the probe beam's detuning for two different probe beam sizes.

The typical diameter of a MOT is about 1 mm and if we use that as the interaction length z then (4.3.6) gives us a peak density in the MOT of $1.2 \cdot 10^{10}$ atoms/cm^3. This is a value typical for a MOT.

Chapter 5

Ultra-stable probe laser at 265.6 nm

As mentioned in chapter 1.2 an atomic clock needs a macroscopic oscillator such as a (stabilized) laser to probe the clock transition. This chapter will deal with our macroscopic oscillator - our clock laser and especially the cavity it is locked to - and how we obtain enough light at 265.6 nm to probe the mercury clock transition.

Figure 5.1 shows an overview of how the probe light is created. Our clock laser is a 1062 nm fiber laser locked to an ultra-stable cavity, whose frequency can be compared with the LNE-SYRTE microwave reference through a femto-second laser comb. To obtain a probe beam with enough power we injection lock a (DFB) slave laser with the stabilized light and then frequency double its light twice to reach the clock frequency.

The DFB laser and the frequency doubling stages were placed on the main optic table with the vacuum chamber for the mercury atoms and the whole cooling setup (cooling laser, frequency doubling stages, saturated absorption,...etc.), while the fiber laser was placed by itself next to a small optic board used as an optical distribution central. The ultra-stable cavity is placed on its own 900 mm x 750 mm optical board placed on an anti-vibration platform inside a sound proof box.

We use single-mode optic fibers to both optically connect the parts of the experiment not on the same optic table and to connect with external experiments such as the femto-second comb. The fibers are all polarization-maintaining with the exception of the fibers used to send light stabilized on the ultra-stable cavity towards the femto-second comb and the OPUS

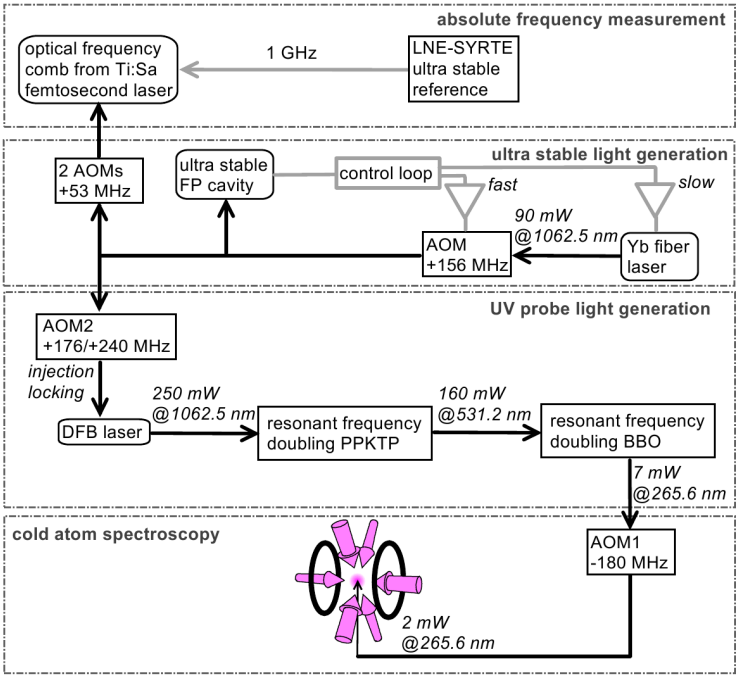

Figure 5.1: Overview of the setup for creating the clock light used to probe the mercury clock transition.

cavity.[1]

5.1 Clock laser and ultra-stable cavity

5.1.1 The fiber laser

Our clock laser is a Koheras 200 mW fiber laser with a temperature controllable wavelength ranging 644 pm ($\sim$ 170 GHz) around 1062.467 nm. Relative intensity noise (RIN) measurements done with a dynamic signal analyzer and a spectrum analyzer on a high bandwidth photo-diode measurement of the laser light at 100 mW is shown in figure 5.2(a). The laser frequency noise was obtained by locking the laser to a 11000 finesse Fabry-Perot cavity (this is not the ultra-stable cavity used generally for locking the laser) by the Pound-Drever-Hall technique with a bandwidth of at least 1 MHz. The 200 MHz AOM signal used to lock the light was then measured

[1] *Oscillateur Photonique Ultra Stable* A cavity of similar design in a neighboring lab used for comparison.

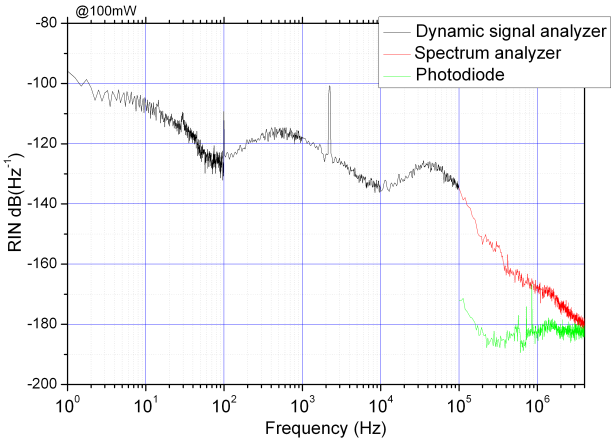

(a)

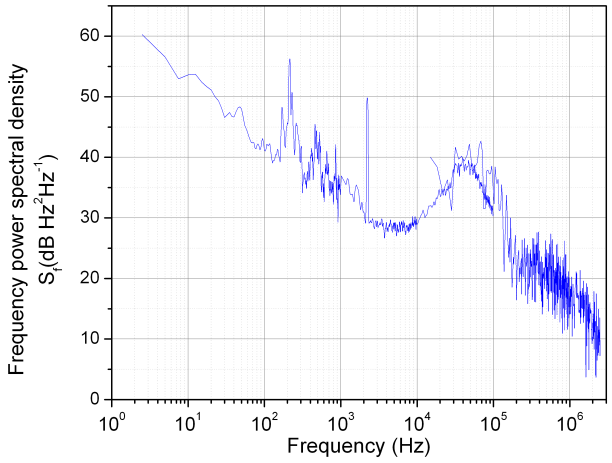

(b)

Figure 5.2: (a) The relative intensity noise and (b) The frequency noise (power spectral density) of the fiber laser at 100 mW output power

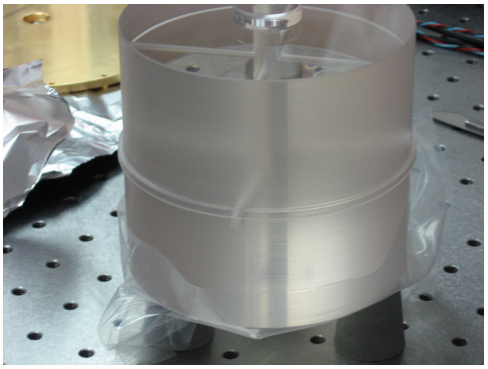

Figure 5.3: The ULE glass ultra-stable cavity.

either directly by a spectrum analyzer[2] or indirectly by a dynamic signal analyzer after a frequency-to-voltage converter. Figure 5.2(b) shows the results. Using (3.3.2) we estimate that the free-running fiber laser has a 3 kHz line width.[3] The laser is kept at 100 mW.

5.1.2 The cavity

To be able to observe a clock transition with a Hertz linewidth we have to stabilize the clock laser even further. This is done by locking the laser to an ultra-stable cavity. After careful considerations, including finite element modelling (see [Millo et al., 2008] for further details) we have chosen a 10 cm long cavity with the spacer being a 11 cm diameter cylinder made of Corning ultra low expansion (ULE) glass weighing in total 2.2 kg (shown in figure 5.3). We use one flat mirror and one mirror with a 500 mm radius of curvature. We use the cavity in a vertical setup while a similar cavity in the lab next door (OPUS) is used in a horizontal setup. The cavity has a protrusion (as can be seen on figure 5.3) which is posed on a ring of invar which again is posed on three points protruding from the innermost heat shield.

We hope and estimate that the thermal noise (the Brownian motion of the molecules due to the material temperature) of the mirrors will end up being what will limit the low frequency noise and stability of the cavity at 1 second. We have therefore chosen to use mirrors of fused silica instead of ULE choosing a lower thermal noise but a higher expansion coefficient. To

[2]see appendix C for details about how the frequency noise was obtained.
[3]The official Koheras specifications indicate a line width of less than 2 kHz.

estimate the possible thermal noise level we use the equations in [Numata et al., 2004] for the power spectrum density of the displacement of each end of a cylindrical spacer (with length L and radius R) of ULE and for each mirror made of fused silica and its coating due to thermal noise:

$$G_{spacer}(f) = \frac{4k_BT}{2\pi f}\frac{L}{3\pi R^2 E}\phi_{sub,spacer} \tag{5.1.1}$$

$$G_{mirror}(f) = \frac{4k_BT}{2\pi f}\frac{1-\sigma^2}{\sqrt{\pi}Ew_0}\phi_{sub,mirror} \tag{5.1.2}$$

$$G_{coating}(f) = G_{mirror}(f)\cdot\frac{2}{\sqrt{\pi}}\frac{1-2\sigma}{1-\sigma}\frac{\phi_{coat}}{\phi_{sub,mirror}}\frac{d}{w_0}, \tag{5.1.3}$$

where w_0 is the beam radius at the mirror (approximately 260 μm and 290 μm respectively)[4]. Notice how the frequency noise has a $1/f$ dependency on the fourier frequency f (flicker frequency noise). The important parameters are Poisson's ratio[5] σ, Young's modulus[6] E and the mechanical loss angle ϕ. For ULE $\sigma = 0.18$, $E = 68$ GPa and $\phi_{sub} = 1.667\cdot 10^{-5}$ while for fused silica $\sigma = 0.17$, $E = 73$ GPa and $\phi_{sub} = 1\cdot 10^{-6}$.[7] A calculation using a $d = 2$ μm coating thickness and $\phi_{coat} = 4\cdot 10^{-4}$ (coating values used in the aforementioned reference) shows that the corresponding relative Allan deviation of the cavity frequency is $1.4\cdot 10^{-16}$ at 1 second for thermal noise exclusively from the mirrors, $2.3\cdot 10^{-16}$ at 1 second for thermal noise exclusively from the mirror coating and $8.1\cdot 10^{-18}$ at 1 second for thermal noise exclusively from the spacer.[8] Even though the spacer material has a

[4]The beam radii are estimated by assuming that the beam is perfectly Gaussian, the wavefront radius of curvature $R(z)$ equals the curved mirrors curvature at that mirror and that the beam has it's waist at the flat mirror and then using that

$$R(z) = z\left(1+\left(\frac{\pi w_0^2}{\lambda z}\right)^2\right)$$

$$w(z) = w_0\sqrt{1+\left(\frac{\lambda z}{\pi w_0^2}\right)^2}$$

for a gaussian beam, where $w(z)$ is the beam radius at the distance z from the waist, w_0 the beam size at the waist and λ the wavelength ($\sim$1062.5 nm).

[5]How much the material expands in the two other directions when compressed in one.

[6]A measure of the stiffness of the material.

[7]The ULE values are all from [Numata et al., 2004] while the fused silica values are from [Rathmann et al., 1968] and [Numata et al., 2004].

[8]To obtain the Allan deviation from the displacement PSD (power spectral density) we first calculate the frequency PSD by using that $\delta L/L = \delta\nu/\nu$ where δL is the square-

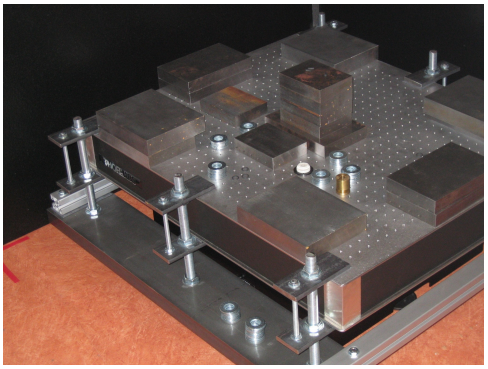

Figure 5.4: The optical breadboard placed on the anti-vibration platform (not visible) with weights attached to the side to reach the nominal weight of the table. Additional smaller weights are placed onto the table since this was for testing purposes before the assembly of the cavity setup.

higher thermal noise it is negligible compared with the thermal noise from the mirrors. Adding the thermal noise for the whole cavity yields a relative Allan standard deviation of $3 \cdot 10^{-16}$ at one second (using ULE mirrors yields $6 \cdot 10^{-16}$ at one second), which serves us as target for Allan deviation over one second on the clock probe. Above a couple of tens of Hz we expect the frequency noise to be limited by white frequency noise from electronic components in either the electronics used for measuring or for locking or due to measurement shot noise. We expect to be able to lock the signal to the atomic clock transition with a $\sim$1 second time constant as in other clocks so far. Ultimately we expect that for longer time periods the clock stability will be limited by the pulsed servo-loop due to the Dick effect [Santarelli et al., 1998], which also would lead to white frequency noise.

But to achieve this kind of noise level we need to address other sources of disturbances and make sure that they have a limited effect on the cavity. These includes mechanical vibrations, acoustic noise and temperature fluctuations.

5.1.3 Protection against vibrations

One key aspect in isolating the cavity from its surrounding environment is to decrease the sensibility to vibrations from the floor. We have placed an optical breadboard with the cavity on a passive anti-vibration platform (650BM-1 Isolator from 'Minus K Technology'). Small rubber rings were positioned in between breadboard and anti-vibration platform both near the edge and near the center. The table has a nominal load between 227 and 318 kg. Initial estimation of the cavity setup's (breadboard, cavity, vacuum chambers, heat shields and small ion pump) weight gave about 200 kg. We have therefore added two large 50 kg steel weights and a number of smaller (3, 6 and 10 kg) weights (see figure 5.4). The two large weights were hanged on the side of the breadboard to lower the center of mass and thereby decrease the importance of pendulum-like movements of the table. The 50 kg weights are long bars and to decrease the sensitivity to vibrational resonances along the bars sheets of lead were placed at each contact point with the table. Additionally we rigidified the bars by connecting the two bar's ends with each other using smaller square aluminum rods. The weight of the whole setup carried by the anti-vibration platform is just above the specified maximal 318 kg.[9] The masses on the table are distributed such that the center of mass is close to the center of the anti-vibration platform in the horizontal directions.

To better characterize and optimize the noise from vibrations onto the cavity we made a number of measurements on the well-balanced board[10] using accelerometers and a seismometer. We used two different sizes of accelerometer-sensors (PCB Piezotronics 626A03/626A04) and in both cases the readings were treated by a PCB Piezotronics signal conditioner before

root of the displacement PSD and $\delta\nu$ the square-root of the frequency PSD. Since thermal noise is flicker noise we use that $\sigma_y^2(\tau = 1\text{ s}) = 2\ln 2 S_y(f = 1\text{ Hz})$ [Vanier and Audoin, 1989] to obtain the Allan deviation.

[9] It is an advantage to have a as heavy load as possible (within the nominal load) since this decreases the horizontal oscillation frequencies for which the anti-vibration platform is providing a better isolating against.

[10] All the vibration measurements were done prior to mounting any experimental equipment on the table. Instead a number of additional weights were carefully added to equilibrate. Be also aware that the measurements were done in the 'atelier 14' lab instead of the current underground lab in the Foucault laboratory basement complex. The difference being that the 'atelier 14' lab is on the ground level and closer to the railway/metro station at 'Denfert-Rochereau' than the Foucault laboratory which is two floors under ground.

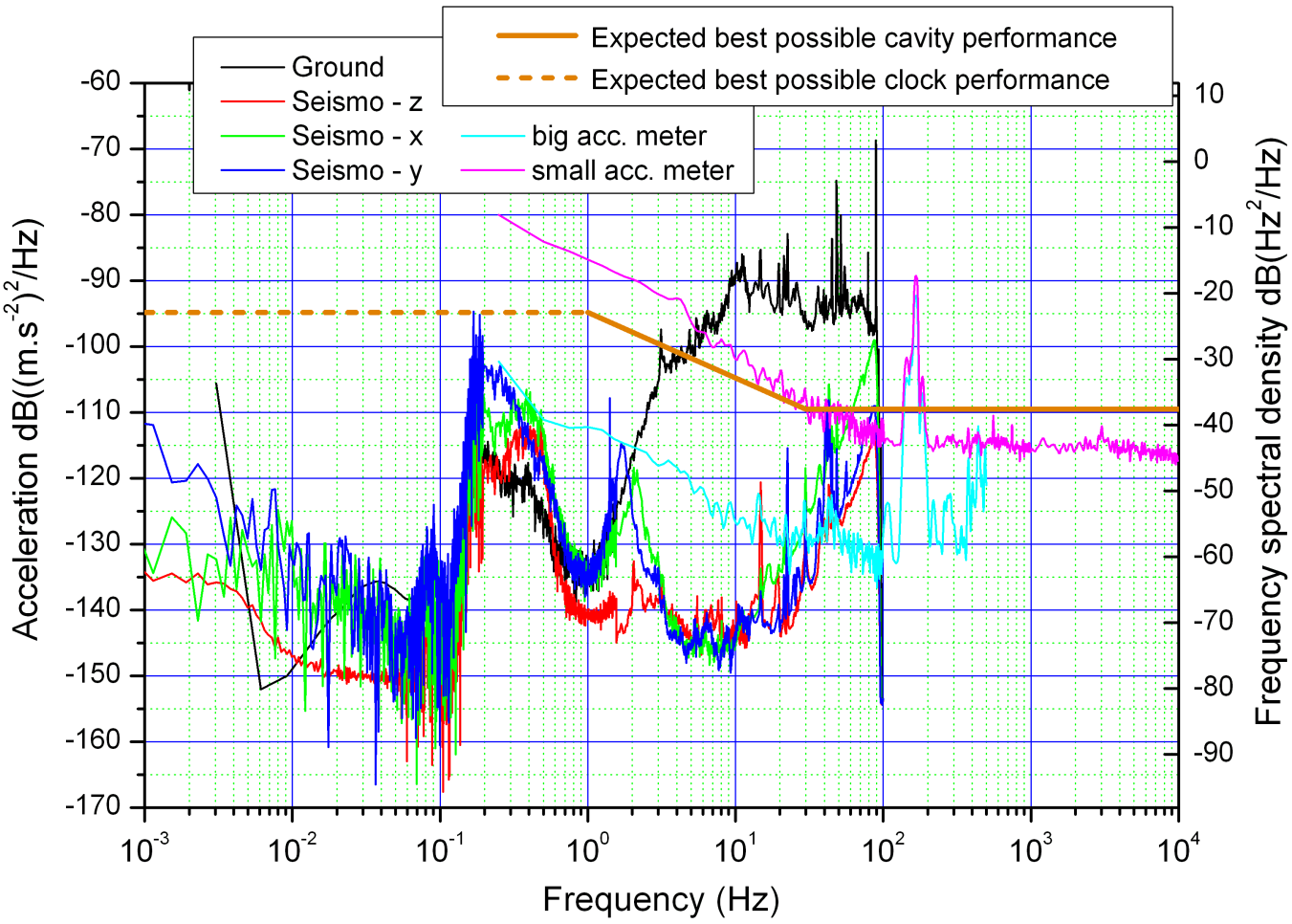

Figure 5.5: Graphs showing vibration measurements measured along different axes ('z' being vertical) by a seismometer and along the vertical by two different sizes of accelerometers. The black graph shows the vertical seismometer measurement on the floor. Be aware that the seismometer measurements were done several days apart. The orange graphs shows an estimate of the best possible performance for the ultra-stable cavity for frequencies above 1 Hz and for the atomic clock for frequencies lower than 1 Hz. The left Y-axis shows the acceleration power spectral density while the right Y-axis shows the conversion into frequency power spectral density (using the conversion factor for vertical response measured at 1.25 Hz).

being analyzed by a dynamic signal analyzer whose output can be seen in figure 5.5. The seismometer was a CMG-3TD from Guralp[11] which output was the velocity of an internal mass. The results of the typical night-long measurements have been converted into power spectral density of the acceleration and is also shown in figure 5.5. This figure compares the vibration measurements with what is expected to be the best possible noise level of the cavity due to thermal noise (as was explained in subchapter 5.1.2). Under 1 Hz it is the expected noise limit of the light locked to the atomic clock transition that is shown. Resent measurements of the cavity fractional frequency response to horizontal vibrations have given $1.4 \cdot 10^{-11}/\mathrm{ms}^{-2}$ at 1.25 Hz ($2.4 \cdot 10^{-12}/\mathrm{ms}^{-2}$ for vertical vibrations). By using this as the conversion coefficient for all frequencies we obtain the scale for the frequency power spectral density shown on the right Y-axis of the graph and this is what is used for placing the expected performance graphs (orange). The frequency response measurement was done by using an electric motor to vibrate the anti-vibration platform with a frequency of 1.25 Hz. An accelerometer was measuring the vibrations next to the cavity while the cavity frequency was monitored.

When first looking at the graphs in figure 5.5 it is noticeable how the two accelerometer measurements neither agree's with each other or the seismometer measurements. It is clear that the pink graph shows the sensor noise of the small accelerometer except for the peak just below 200 Hz also visible on the big accelerometer measurement (cyan). This is most likely a resonance in the table setup. Below 100 Hz the cyan graph shows the sensor noise. The seismometer graphs between 10 and 100 Hz shows a strange increase in the vibration activity but this is also due to sensor noise near the end of its frequency range. Between 1 and 100 Hz it is important to notice the large difference between the seismometer measurements done on the table (red, green, blue) and on the ground (black). This is the frequency range where it really matters since the frequencies are too low for the noise to be removed by averaging when measuring the clock transition and too short a time period to span a whole clock measurement cycle. The peaks around 2 Hz on the horizontal seismometer measurements are due to table pendulum resonances. The anti-vibration platform has a natural resonance around 0.4 Hz barely visible on the graphs. As expected for a passive system the

[11] A thanks to ONERA (Office National d'Études et de Recherches Aerospatiales) for letting us borrow the seismometer.

table has no apparent effect on vibration at lower frequencies. Around 0.2 Hz all seismometer measurements shows a large feature which could pose a problem. This is a feature that both changed (slightly) in frequency and especially in strength from day to day and especially from week to week.[12] It is due to seismic waves excited by waves' movement in the greater oceans around the planet and this is strongly dependent on the weather around the planet and especially in the Atlantic ocean and therefore the season.[13] When comparing with the orange graphs this could pose a problem during a nearby hurricane. Elsewhere the orange graphs seems to indicate that the anti-vibration setup does a good job except for maybe the one resonance near 200 Hz.

5.1.4 Protection against acoustic noise

To avoid or decrease the acoustic noise from surrounding equipment and people we encapsulated the whole cavity setup (including anti-vibration platform) in a sound proof box. This box is a home-made 1.4 x 1.4 x 1.5 m wooden box with removable panels on all sides. The inside of the wooden panels are covered by a 45 mm thick layer of composite Agglobel foam (7 kg/m2) from Tramico. All the cabling is coming in through a hole in the roof which is covered by a foam covered plate. Both this top plate and the removable side panels are secured to each other and the roof of the box by a system of screws. The efficiency of the box is shown in figure 5.6 which shows the power spectral density of microphone measurements with a microphone being placed respectively inside and outside the (closed) sound proof box. The box itself has a resonance around 25 Hz which is a vibrational mode of the panels loaded by the foam.

5.1.5 Temperature stability

To be able to sustain the assumption that we can reach the thermal noise floor of the ultra-stable cavity when considering the low frequency noise of the light locked to the cavity we have to consider the stability of the cavity length due to thermal expansion of the spacer material. The ULE glass

[12] The 'seismo' and the 'ground' measurements here are not done the same day.

[13] Since the seismometer only was borrowed for a couple of months it has not been possible to test the seasonable dependency. All the tests with the seismometer were in the late fall - at the end of hurricane season in the Atlantic ocean.

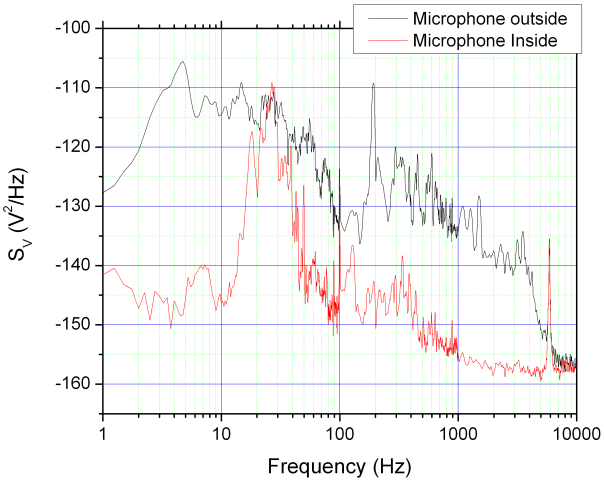

Figure 5.6: The power spectral density of microphone signals.

which makes up the cavity spacer has a vanishing expansion coefficient at a well chosen temperature near 300 K. Due to the mirrors being of fused silica with a different thermal expansion coefficient the mirrors bends when exposed to temperature changes and simulations have shown an impact on the cavity length up to $7 \cdot 10^{-8}$ K^{-1}, and we therefore still need a temperature stability across the spacer of better than a nK at 1 second to have a fractional frequency instability of better than $3 \cdot 10^{-16}$ at one second.[14]. To achieve such a temperature stability it is necessary to do both isolation of the cavity and temperature control of the closest environment.

Apart from the enclosement in the sound proof box we have chosen to enclose the cavity in two vacuum chambers with two additional thermal shields inside the inner chamber as shown in figure 5.7. While the outer vacuum chamber is made of stainless steel, the inner vacuum chamber and the heat shields are aluminium to have better thermal uniformity across the shields. The heat shields are polished and coated with gold so to better reflect heat radiation. The inner vacuum chamber is temperature stabilized by four single-stage Peltier elements each connected to external radiator elements through copper heat rods (shown in figure 5.7(c)). The average of four 5 kΩ Betatherm thermistors placed equidistantly on the outside of the inner vacuum chamber are used for controlling the Peltiers. Another four

[14]Using that $\delta\nu/\nu = \delta L/L$.

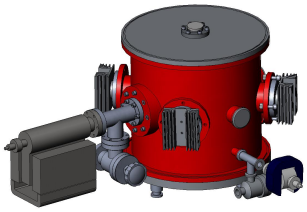

(a)

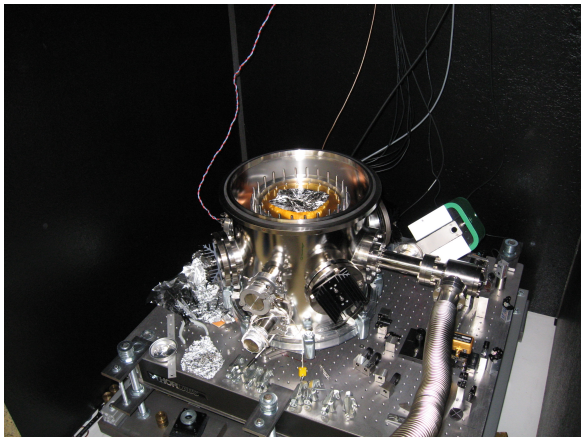

(b)

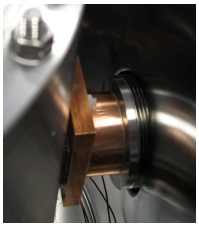

(c)

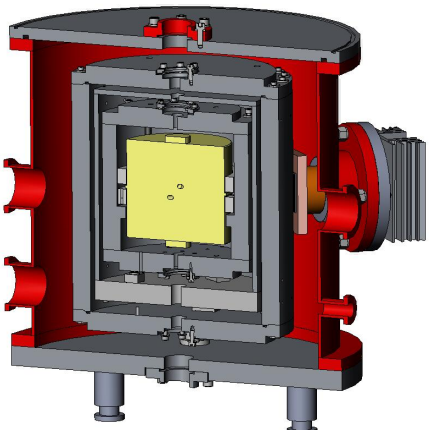

(d)

Figure 5.7: The thermo-mechanical setup around the ultra-stable cavity. (a) Diagram showing the exterior and the ion pumps. (b) Photo of the setup on the anti-vibration platform with the two top lids off. (c) Photo of the Peltier element and the heat tube used for temperature control of the inner vacuum chamber. (d) Cross section showing the interior of the vacuum chambers. The cavity is the yellow part.

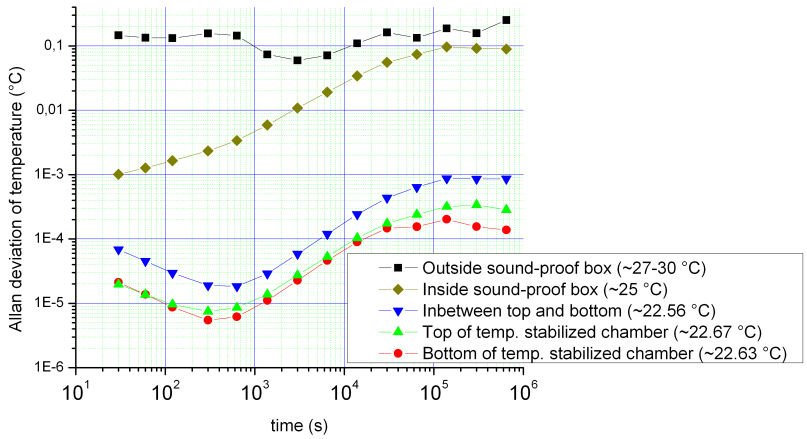

Figure 5.8: The Allan deviation of the measured temperature on the exterior of the temperature stabilized (inner) vacuum chamber over a period of two months during the summer of 2008. One from measurements made completely outside the sound-proof box, one just inside the sound-proof box and the remaining three inside the outer vacuum chamber on the outer side of the temperature controlled vacuum chamber.

thermistors on the same vacuum chamber placed mid between the Peltiers and two thermistors on the top and the bottom of the outer vacuum chamber are used for monitoring. For passing of the light both vacuum chambers and the inner heat shield have BK7 windows which is completely opaque towards heat radiation. They are all tilted with an angle to prevent Fabry-Perot cavity interferometric effects from light reflected off the windows.

The reason for having two vacuum chambers is to insure a good level of vacuum near the cavity. The setup for the temperature control of the inner vacuum chamber includes glue, soldering and wiring which in general can lead to a less good vacuum. Also, we initially wanted to be able to cool down the cavity quite far without having water condensation on the windows so we needed to have the temperature control inside a vacuum. So far the temperature has been kept around room temperature even though the cavity has a thermal expansion turning point 20° below room temperature due to the fused silica mirrors.

Figure 5.8 shows the Allan variation of some of the temperature monitoring sensors around the temperature controlled vacuum chamber measured over a period of about two months. The black and brown/orange graphs

are obtained from sensors placed respectively completely outside the sound proof box and inside the box but outside the vacuum chamber. The three remaining graphs are obtained from the monitoring thermistors mentioned further up. Specifically the blue graph is obtained from the average of the four thermistors placed on the outside of the stabilized vacuum chamber mid between the Peltier elements used for the temperature control. The difference between the measurements made inside and outside the soundproof box seems to indicate that the soundproof box itself filters out temperature instabilities which last less than about 24 hours[15] or in other words that the time constant for temperature propagation through the sound proof box is about 24 hours. The temperature on the temperature controlled vacuum chamber follows the behavior of the temperature fluctuations inside the box but strongly subdued due to the electronic temperature stabilization. Below a couple of hundred seconds we do see a different behavior most likely due to the measurement noise itself or by a lack of short-term correlation between the measurement points and the temperature stabilization. Notice how the temperature near the temperature stabilizing Peltiers is less stable than at the top and at the bottom.

To estimate how the cavity itself behaves due to temperature fluctuations of the vacuum chamber walls we can look at how the cavity frequency has changed due to a significant temperature perturbation. During the summer of 2008[16] the lab climate control broke down for a couple days. The temperature change on the vacuum chamber became too much for the temperature control to handle and consequently the temperature of the vacuum chamber rose by about 2 °C before the climate control was repaired. By looking at the response of the frequency during the following days we estimate a time constant of about 4 days. The model that so far has shown to best emulate the behavior of the cavity frequency due to temperature changes on the (inner) vacuum chamber is a simple double pole low-pass filter (both time constants being 4 days) with a conversion between temperature and fractional frequency for the cavity being $9.9 \cdot 10^{-8}$/K. Figure 5.9 shows the power spectral density (in black) of the aforementioned temperature monitoring on the vacuum chamber surface mid between top and

[15] Which also has been verified by looking at the direct measurements under external temperature fluctuations (for example after climate control mishaps).

[16] Just after the period covered by the measurements which the temperature stability is based upon.

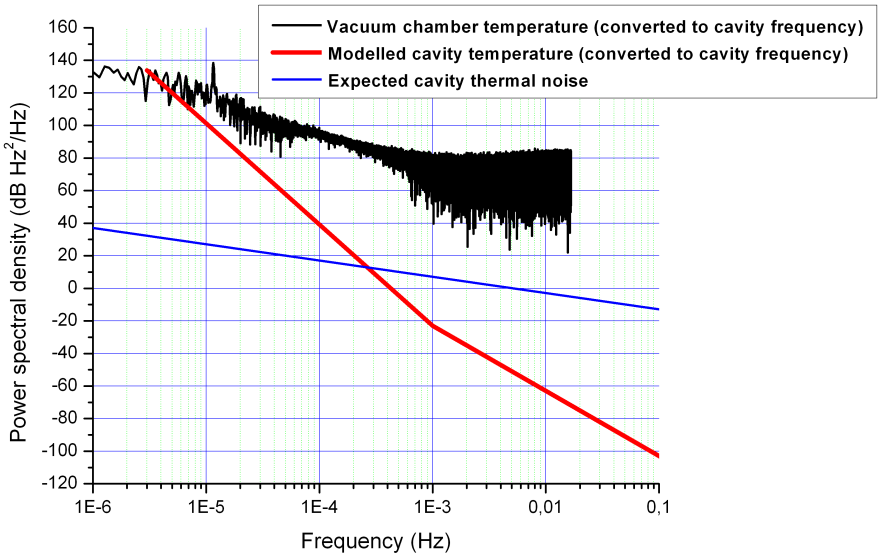

Figure 5.9: In black the power spectral density of temperature measurements made at the midpoint between top and bottom on the inner vacuum chamber. The red graph shows the presumed corresponding temperature behavior at the cavity following a two-pole low-pass filter model, where we assume that for higher frequencies the noise of the vacuum chamber temperature measurements will keep behaving like white frequency noise (flat noise). The blue graph shows the expected level of noise due to thermal noise in the cavity mirrors.

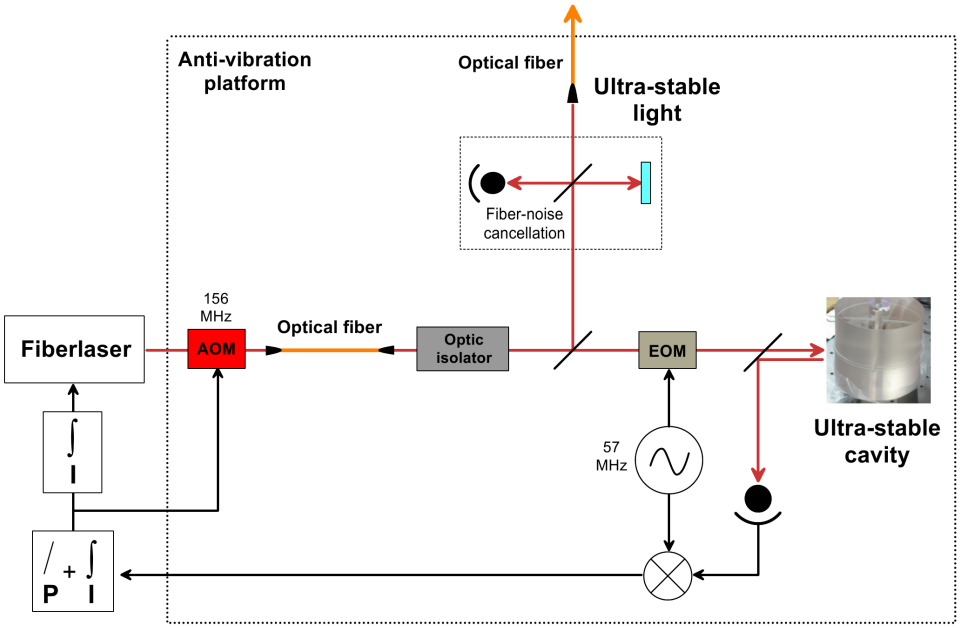

Figure 5.10: The Pound-Drever-Hall servo-loop used for locking the fiber laser to the ultra-stable cavity. Everything shown within the dotted border was placed on the anti-vibration platform.

bottom. The red graph shows the approximate $1/f^4$ improvement of the temperature noise due to a double pole low-pass filter starting at the fourier frequency corresponding to 4 days. The last flat part of the measured noise might be a residue due to measurement noise and not a real picture of the temperature noise. Following the model we see that above $4 \cdot 10^{-4}$ Hz (corresponding to a period of 42 minutes) the power spectral density of the cavity due to temperature fluctuations is smaller than the expected thermal noise of the cavity mirrors (in blue). At least for relatively short amount of time and for normal clock operation we do not expect temperature fluctuations to be an issue.

5.1.6 The cavity lock

Figure 5.10 shows the setup we use for locking the fiber laser onto one of the ultra-stable cavity's resonances to obtain the ultra-stable light. We use the Pound-Drever-Hall stabilization method [Drever et al., 1983][17] where phase-

[17] See also [Black, 2001] for an introduction to the PDH locking method.

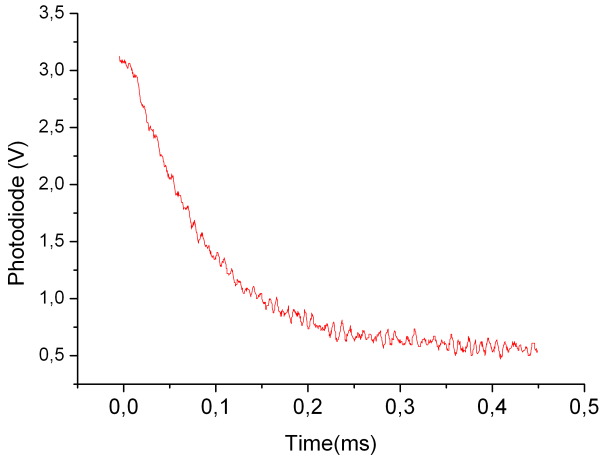

Figure 5.11: The ringdown of the ultra-stable cavity.

modulated light retro reflected off the cavity is measured. An electronic mixer creates the error signal used for locking the laser from the measured signal and the modulation in quadrature.

We use an Electro-Optic Modulator (EOM) at 57 MHz (the oscillation signal being generated by an RF synthesizer) to modulate the phase and a InGaAs photo-diode to measure the light. The obtained error signal is sent through a parallel integrator-proportional gain and then used to lock the light using a 156 MHz AOM. The laser light is led onto the anti-vibration platform through a fiber (not on the figure) and into the AOM before being sent through yet another fiber only 1 meter long. The reason for using the later is to ensure a close to perfect gaussian beam and to avoid the changed angle of the AOM output due to the frequency corrections. The optic isolator is to avoid Fabry-Perot effects between the cavity and the fiber. The correction signal for the AOM is also sent through an additional integrator gain and then used to lock the fiber laser directly through its internal piezo.

Notice that most of the setup is on the anti-vibration platform with the cavity. This is of course to ensure the stability of the lock components itself against vibrations and temperature fluctuations.

Approximately 5 μW are sent to the cavity. By measuring the cavity ringdown (the time it takes for the light to leave the cavity, see figure 5.11) on the light transmitted through the cavity we estimate the cavity to have a

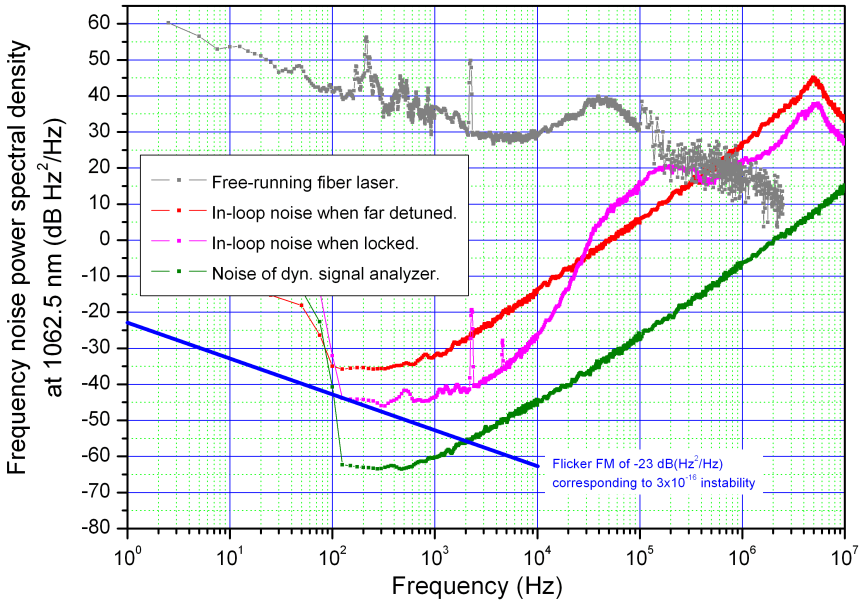

Figure 5.12: The power spectral density of the frequency noise by different aspects of the Pound-Drever-Hall lock of the 1062.5 nm fiber laser. In gray the earlier shown measurement of the free-running fiber laser noise. In red and pink the noise of the PDH error signal obtained by a dynamic signal analyzer and multiplied by a transfer function corresponding to a single pole low-pass filter for respectively when the laser was far detuned from a cavity resonance and the laser was locked to a cavity resonance. The green graph shows the noise of the dynamic signal analyzer when disconnected from the PHD system also multiplied by a transfer function corresponding to a single pole low-pass filter. the blue line shows the expected flicker noise due to thermal noise of the cavity mirrors.

finesse of about 850000 - a great deal larger than the ∼300000 we expected from the manufacturer's specifications. With a free-spectral range of 1.5 GHz the measured finesse corresponds to a cavity line width of 1.8 kHz. Figure 5.12 shows frequency noise of different aspects of the PDH lock. The red and the pink graphs are noise measurements of the PDH error signal multiplied by the transfer function corresponding to a single-pole low-pass filter with the cavity line width being the cutoff frequency (see [Bondu and Debieu, 2007]). The red one is for when the laser was far detuned from a cavity resonance and is a measure of the noise of the electronics and the photo-diode. The pink graph is from when the laser was locked to the cavity and shows the gain limit of the lock. Below the locking bandwidth, which seems to be around 4-500 kHz when comparing with the free-running fiber laser, the actual noise of the locked light is the maximum of the two curves. Notice that for fourier frequencies lower than 500 Hz the noise of the locked light seems to be white frequency noise at a level of -35 dB Hz^2/Hz. If this behavior continues further for lower frequencies then when comparing with the expected noise due to thermal noise of the cavity mirrors (shown in blue) the latter will dominate for frequencies lower than 30 Hz (This has been shown in several graphs in this chapter). This is of course assuming that indeed thermal noise will limit the cavity frequency noise but as have been shown so far in this chapter we are confident that we can obtain that limit.

5.2 Fiber-noise cancellation

The use of optic fibers to send ultra-stable light from one place to another induces additional frequency noise due to vibrations and temperature fluctuations. To minimize this we use the fiber noise cancellation scheme known as Doppler cancellation first presented by [Young et al., 1999b] (see also [Ye et al., 2003]) on the fiber connection between the ultra-stable cavity and the femto-second comb and with the OPUS cavity. We expect to include the fiber noise cancellation setup on all optic fiber connections with ultra-stable light.

The principle of the Doppler cancellation scheme (see figure 5.13) is to make a Michelson interferometer with one arm being a short reference and the other the fiber and an AOM with the AOM's first order being partially reflected back through the fiber (the transmitted signal is the noise reduced

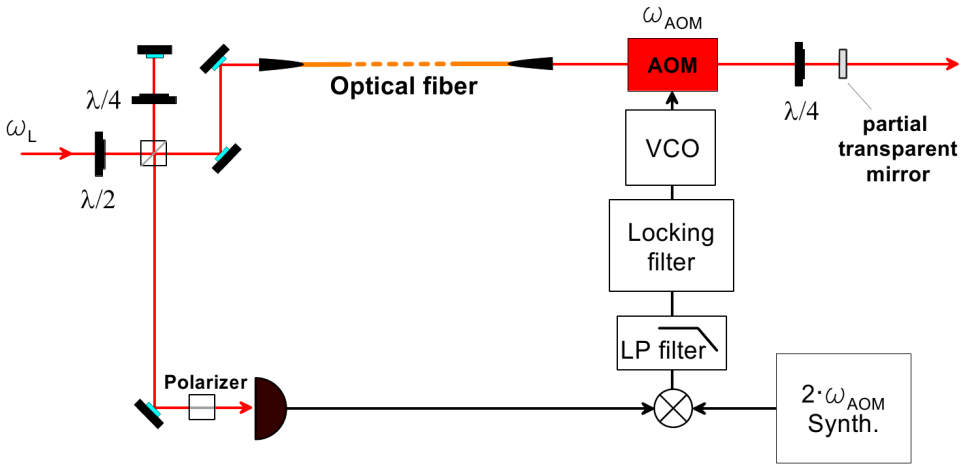

Figure 5.13: The fiber noise (Doppler) cancellation setup. Alternatively the noise correcting AOM can be placed before the fiber.

output). A photodiode detects the beat note between the signals returning from the two arms of the interferometer. If the initial laser signal $s_l(t)$ is of the form

$$s_l(t) = \cos(\omega_L t + \phi_L(t)) \tag{5.2.1}$$

with ω_L being the laser frequency and $\phi_L(t)$ the phase noise of the laser light at time t and if t_0 is the time it takes for the light to pass through the reference arm (single pass) and t_1 the time it takes the light to pass through the fiber once the photodiode measures the signal $s_p(t)$:

$$\begin{aligned} s_p(t) = & \big| \cos\left(\omega_L t - \omega_L 2t_0 + \phi_L(t - 2t_0)\right) \\ & + \cos\left((\omega_L + 2\omega_{AOM})t - \omega_L t_1 - (\omega_L + 2\omega_{AOM})t_1 + \phi_L(t - 2t_1)\right)\big|^2 \end{aligned} \tag{5.2.2}$$

with ω_{AOM} being the AOM frequency. The photodiode removes the optical frequency components leaving:

$$s_p(t) = \frac{1}{2}\cos\left(2\omega_{AOM}t + \omega_L(2t_1 - 2t_0) + 2\omega_{AOM}t_1 + \Delta\phi_L(2t_1, 2t_0)\right). \tag{5.2.3}$$

The two phase terms $\omega_L(2t_1 - 2t_0)$ and $2\omega_{AOM}t_1$ includes fiber length fluctuations through t_1 with the latter being negligible compared with the first. The third phase term $\Delta\phi_L(2t_1, 2t_0) = \phi_L(t - 2t_1) - \phi_L(t - 2t_0)$ is the difference between the induced phase due to a difference in interferometer arm paths and this term contains both the phase noise due to the fiber (and

reference arm) and the laser. By mixing this signal with a reference signal with twice the AOM's frequency we are left with a signal of the form $\cos\left(\omega_L(2t_1-2t_0)+\Delta\phi_L(2t_1,2t_0)\right)$. A servo-loop filter can then easily phase lock the AOM so to remove the noise in the fiber. Of course this will 'copy' any noise on the reference arm of the interferometer onto the output and this can become a limiting factor. To some extent the phase lock also removes the phase noise from the laser.

To test the noise level obtainable by a Doppler cancellation scheme at 1062 nm we mounted a testing setup with a 30 m single-mode optical fiber using the free-running fiber laser as light source. We used a 150 MHz AOM and consequently a 300 MHz synthesizer for the reference signal. The servo-loop filter was a simple parallel integrator/proportional gain with a voltage offset. We used a 80 % reflective mirror for the testing setup. To test the efficiency of the setup we measured the beat note between the output of the fiber noise cancellation system and (a fraction of) the incoming signal. This removed the optical frequency and left a signal of the form $\frac{1}{2}\cos(\omega_{AOM}t+\omega_L t_1+\Delta\phi_L(t_1,0))$ which then is mixed with the synthesizer signal sent through a frequency divider so to divide its frequency by two. Both mixing inputs were additionally frequency divided by $n=16$ to avoid phase noise close to or higher than π. After suitable filtering the signal had the form $\cos(\omega_L t_1/n+\Delta\phi_L(t_1,0)/n+\Delta\phi_{synth})$ where $\Delta\phi_{synth}$ is an arbitrary phase chosen such that $\cos(\omega_L t_1/n+\Delta\phi_L(t_1,0)/n+\Delta\phi_{synth}) = \sin(\omega_L t_1/n+\Delta\phi_L(t_1,0)/n) \sim \omega_L t_1/n+\Delta\phi_L(t_1,0)/n$. The noise of the Doppler cancellation setup could then readily be measured by a dynamic signal analyzer. Figure 5.14 shows the result of the measurement of the frequency noise (corrected for frequency divisions) for the case of a closed and an open servo-loop. In the open loop case we used the synthesizer and a frequency divider to directly stabilize the AOM to 150 MHz since the VCO was too unstable when not being externally controlled. The higher open loop noise required frequency divisions by 128 (instead of 16).

The results (shown in figure 5.14) clearly shows an improvement of the noise by 10-20 dB across the whole range of frequencies. The locking bandwidth was about 100 kHz. We assume that optimally the clock laser's light locked to the ultra-stable cavity will be limited by the (room temperature) thermal noise of the cavity mirrors at low frequencies. This is frequency flicker noise with a relative noise of $3\cdot10^{-16}$ at one second. At higher frequencies (from around a couple of tens of Hz) we would be limited by white

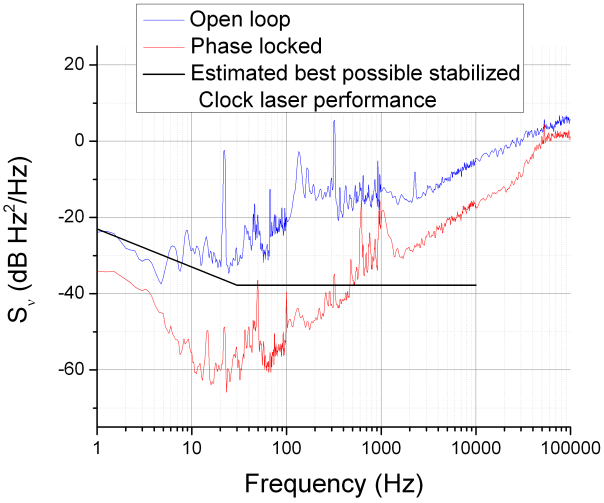

Figure 5.14: The frequency noise from the (test) Doppler cancellation setup in comparison with the expected best possible clock laser light when locked to the ultra-stable cavity. The test was done on the free-running fiber laser at 1062.5 nm. The results are corrected for frequency divisions in the setup.

frequency noise. From figure 5.14 it is clear that up until close to 1 kHz the Doppler cancellation makes sure that noise induced by the fiber won't contribute significantly to the overall noise level. The noise level for higher frequencies is most likely due to the laser's own noise (from the $\Delta\phi_L(t_1, 0)$ term). During the test the laser was not stabilized to a cavity.

To measure the instability induced by the Doppler cancellation we again measured the beat note between the input and output signal of the test setup with a photodiode. The photo-diode signal was then mixed with a second synthesizer at 150.030 MHz[18] that is frequency offset $\delta\omega_{synth}$ by 30 kHz from the AOM frequency. After filtering, the mixed signal had the form $\cos(\delta\omega_{synth}t + \omega_L t_1 + \phi_L(t_1, 0) + \Delta\phi)$ with $\Delta\phi$ being a arbitrary phase. The instability was then measured using an electronic counter. $\omega_L t_1$ and $\Delta\phi$ is then of no importance and the drift or stability of the signal could then be estimated by calculation of the Allan variance of the obtained frequency. Figure 5.15 shows the result compared with the estimated best possible clock behavior, which we estimate to be white frequency noise due to the

[18]This synthesizer's clock was synchronized with the Doppler cancellation synthesizer so to have a correct frequency offset.

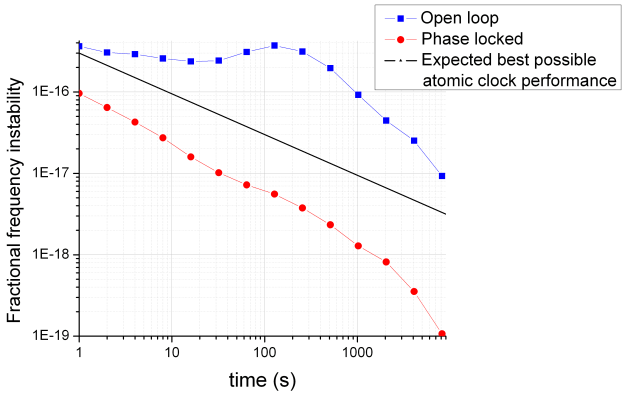

Figure 5.15: The relative stability (The relative Allan frequency standard deviation) of a signal sent through the (test) Doppler cancellation setup. This is compared to the expected best possible

locking of the laser to the atomic clock transition. It seems plausible that measurement of the clock transition can be done with a frequency of about 1 Hz where we are limited by the noise of light 'only' stabilized to the ultra-stable cavity, what we estimate to be $3 \cdot 10^{-16}$ (in fractional frequency). It is clear from figure 5.15 that the Doppler cancellation also stabilizes the signal (at least up until 10 000 s) to the appropriate level for supposed optimal clock operation.

The present noise cancellation setup between the ultra-stable cavity and the femto-second comb uses two AOM's (which totals a shift of 53 MHz), one on the intermediate optical board and the other one on the far end of the fibers. Obviously this system has two optic fiber connections and the noise induced is removed from both fibers. The reason for having AOM's in two different places is to have one close to the electronic/photodiode in our lab and to have one just before the semi-reflecting mirror to avoid that reflections from the (second) fiber does not have the same frequency. The fibers are respectively 5 and 10 m and with only the short one being polarization-maintaining. We use a semi-reflecting mirror with a much smaller reflection (4 %) than for the testing setup.

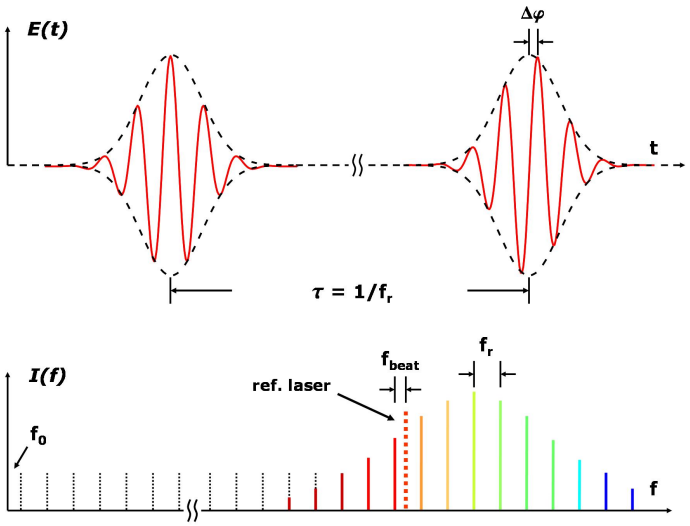

Figure 5.16: The typical shape of a femto-second pulse in the time domain (on top) and in frequency domain (in the bottom). The last is usually called a frequency comb. This figure is from [Brush, 2006].

5.3 Characterization of the stabilized clock light through comparison with external references

To be able to relate our infra-red clock-laser to our local microwave frequency reference we make use of a femto-second laser to create a so-called 'frequency comb' [Hänsch, 2006].

A femto-second laser is a laser that sends out a periodic pulse train with a pulse duration of the order of tens of femto-seconds and in the frequency domain this kind of signal is an infinite row of equidistant narrow peaks - a 'frequency comb' (as shown in figure 5.16). The frequency of the n'th 'comb-line' is typically written

$$f_n = nf_r + f_0, \tag{5.3.1}$$

where f_0 is an offset frequency and $f_r = 1/\tau$ is the interval between two comb-lines where τ here is the pulse repetition rate (when describing the pulse train in the time domain).

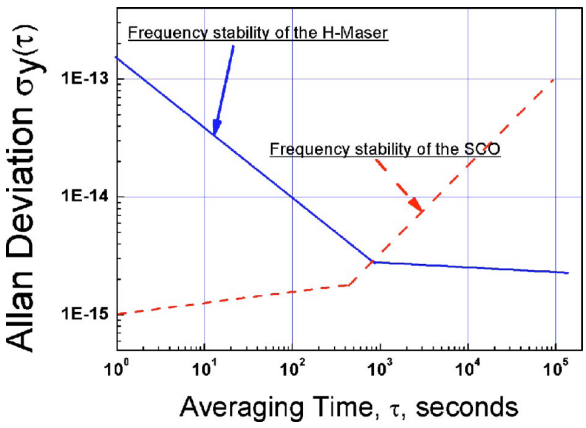

Figure 5.17: Trend lines for the Allan deviation of the hydrogen maser and the cryogenic sapphire oscillator 'CSO' (written SCO here). Graph is from [Chambon et al., 2005].

To compare two signals far apart in frequency a known comb-line can be locked to one of the signals while the other signal is heterodyned with its closest comb-line. Any optical frequency can be determined by the measurement of three RF frequencies (including the measurement of f_0) .

In our case the femto-second laser is a mode-locked Ti:Sa laser with a repetition rate of 765 MHz. The offset frequency f_0 is measured with the standard $f - 2f$ self-reference techniques [Jones et al., 2000]. The beat note between a frequency doubled comb line and the comb line signal at twice the line number was measured. If we chose the k'th comb line its frequency would be $f(k) = f_0 + k \cdot f_r$ and frequency doubled it would then be $2 \cdot f(k) = 2f_0 + 2k \cdot f_r$. The $2 \cdot k$'th comb line would have a frequency $f(2k) = f_0 + 2k \cdot f_r$ and a beat note between those two include a frequency component f_0.

The local reference signal that we use to compare with is a 9.2 GHz signal up-converted from a 1 GHz signal distributed throughout the SYRTE laboratories at l'Observatoire de Paris with an RF optical fiber link. The origin of this signal is a liquid-helium cryogenic sapphire oscillator (CSO) locked to a hydrogen maser. The CSO is again monitored by the primary standard Cs/Rb fountains here at SYRTE. The fractional frequency (in)stability of the distribution signal has been estimated to be about $1 - 2 \cdot 10^{-15}$ up to a 1000 seconds (see fig 5.17) [Chambon et al., 2005]. Notice that the reference signal should have a characteristic minimum in the frequency stability around a 1000 seconds.

To characterize the quality of the ultra-stabilized light we first compared it with the local 9.2 GHz reference from the CSO and then with the horizontal OPUS cavity similar to ours.

The comparison with the CSO was done through the femto-second comb by locking a comb line to the ultra-stable light and then beating the 12th harmonic of the repetition rate with the 9.2 GHz signal from the CSO.[19] The blue graph in figure 5.18 shows the relative frequency instability as an Allan deviation of the beat note with the linear drift having being removed. Up until a couple of tens of seconds it is limited by the RF link and a microwave synthesizer. Notice the extremely good behavior of the cavity above 100 seconds due to the effective temperature stabilization. In comparison with the reference from the CSO we have also established a cavity drift of -50 mHz/s at the 1062.5 nm which is a fractional drift-rate of $-1.8 \cdot 10^{-16}$/s.

The red curve in figure 5.18 shows the comparison (after the removal of noise fitted with a second order polynomial) with OPUS done by making a direct beat note with light stabilized on the OPUS cavity. This shows a remarkable relative instability level of $7 \cdot 10^{-16}$ at a few seconds of integration when comparing with the estimated addition of the constant relative instability level of the two cavities giving $\sqrt{2} \cdot 3 \cdot 10^{-16} = 4 \cdot 10^{-16}$ when being limited by the thermal noise of the mirrors.[20] The drift being seen after 4 seconds of integration is due to the lack of active temperature stabilization of the OPUS cavity at the time of this measurement. But even below this point we do not clearly see the expected flicker noise (constant Allan deviation/variance) due to thermal noise. Further measurements with active temperature stabilization on both cavities will be done to clearly identify the thermal limit of the cavities.

Notice that both the light sent towards the femto-second comb for comparison with the CSO and the light sent towards the OPUS cavity was sent through an optical fiber with a Doppler cancellation setup.

5.4 The clock probe at 265.6 nm

To probe the clock transition at 265.6 nm we had to convert the 1062 nm light by two frequency doubling stages similar to the ones used for the

[19] Chapter 6 contains more detailed accounts of how we used the femto-laser to make comparisons with the CSO although with some differences from what was used here.

[20] The noise of the two cavities being added quadratically.

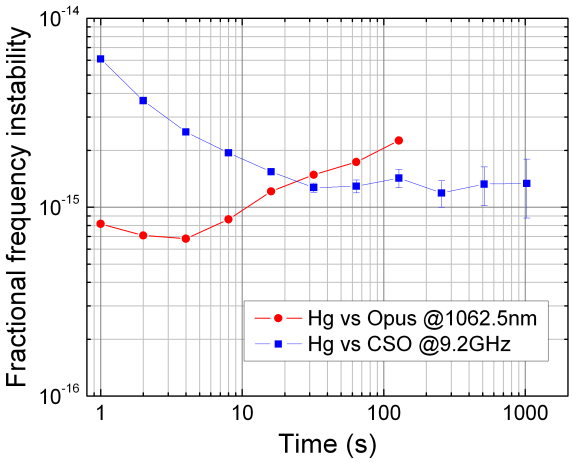

Figure 5.18: The Allan deviation w hen comparing our (Hg) ultra-stable cavity with the SYRTE RF reference from the CSO and when comparing with the similar horizontal ultra-stable cavity OPUS. For the blue graph linear drift has been removed while for the red graph noise fitted with a second order polynomial has been removed.

cooling light. But in this situation we only saw the need for 5 mW of power (at 265.6 nm). Since the clock laser itself has a maximum power output of 200 mW and we had to take into account losses in fibers, AOM's and for light sent towards others purposes such as the femto-second laser plus the fact that we wanted to avoid using the laser at its limit we chose to use a slave laser injection locked to the clock laser.

5.4.1 Injection lock

We use a DFB (Distributed Feed-Back) semi-conductor diode laser as slave laser. It has a maximal output power of almost 400 mW (when using it at a current of 2 A) but we have restrained ourself to using it at the safer 1.5 A at which the laser can output 360 mW. The laser light is badly shaped at the output and the reshaping of the beam plus two optical isolators decreases the actual power to about 250 mW (at 1.5 A). The wavelength can be adjusted through the temperature control for coarse control or through small adjustments of the current for fine tuning. Typically the diode temperature is kept at a temperature below -10° C which is obtained by the use of

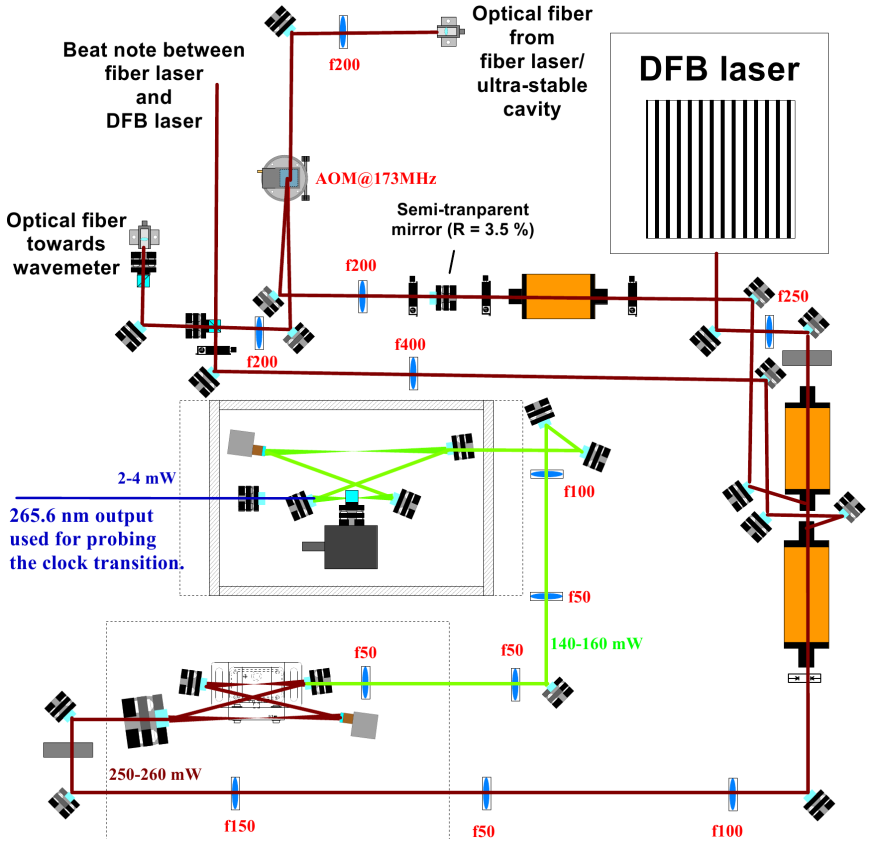

Figure 5.19: The setup used to create the clock transition probing beam and for testing the injection noise.

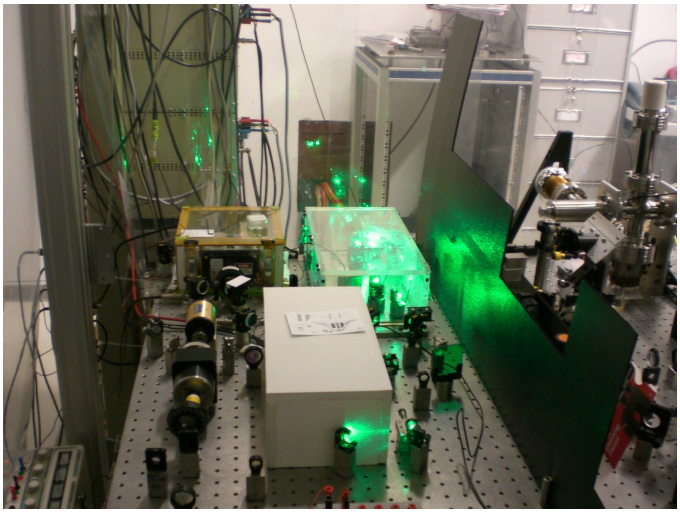

Figure 5.20: A photo of the actual system of doubling cavities used for creating the probe light at 265.6 nm. To the far left the DFB-laser, in the middle the first stage doubling cavity and to the far right the second stage frequency doubling cavity.

a water-cooled Peltier element where the water (containing anti-freeze) is kept at -6 ° C by a chiller.[21]

To avoid having reflections from the first doubling cavity (and intermediate optics) possibly damaging the laser we use two optical isolators. We inject the clock light into the laser by superposing it with a leak from a polarizing cube in the first optical isolator (as shown in figure 5.19).

Figure 5.21 shows the measurement of the phase power spectral density[22] of the injection (in red) to compare with an estimation of best possible noise of our ultra-stable cavity (shown in black). We expect that at low frequencies (< 100 Hz) the ultra-stable cavity will be limited by the thermal noise of the cavity mirrors typically frequency flicker type noise which we estimate to be about $3 \cdot 10^{-16}$ in relative instability at one second. At higher frequencies we expect to reach a white frequency noise limit due to the electronics. The measurement of noise induced by the injection was done by measuring the beat note between the clock signal used to inject with and the DFB laser output. We used a reflection from one of the isolator polarization cubes for the laser output. For frequencies below 100 kHz the beat note signal was measured with a dynamic signal analyzer while

[21] The DFB diode was initially bought for use at 1065.5 nm at room temperature.

[22] The graphs are composed of several segments measured in slightly different ways.

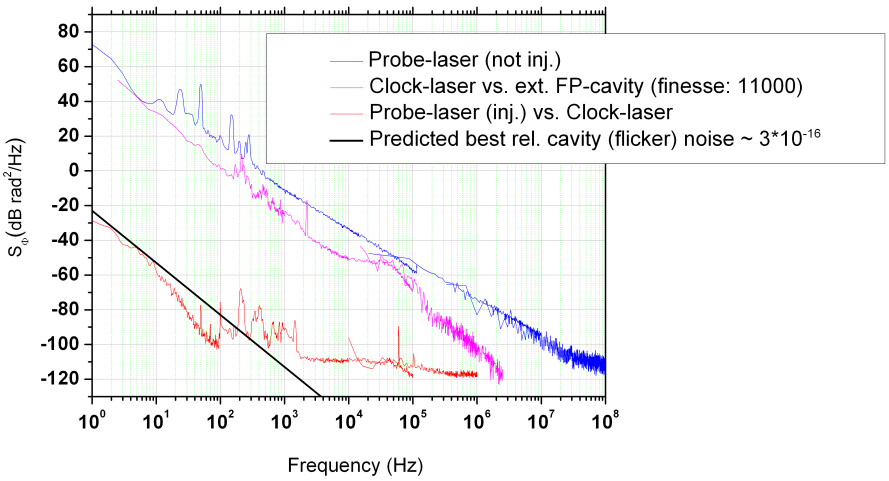

Figure 5.21: The phase power spectral density of the probe laser at 1062.5 nm. Blue shows the noise for the free-running DFB laser measured against the fiber laser (clock laser) and in red the same measurement with the DFB being injection-locked by the clock laser itself. In pink we have the noise of the (free-running) clock laser measured against a high-finesse fabry-pérot (not the ultra-stable cavity). For comparison I have included the prediction of the best possible relative flicker noise ($3 \cdot 10^{-16}$) of our ultra-stable cavity.

for frequencies higher than 10 kHz (there was an overlap between the two measurements) we used a spectrum analyzer and then obtained the phase power spectral density using (C.0.9) in appendix C. Up to around 1 kHz the measured noise induced by the injection lock is due to air movement and vibrations on paths uncompensated by the Doppler-cancellation such as the trajectory after the semi-transparent mirror. At some point this might become an issue which could partly be solved by covering the light paths. Beyond 1 kHz it becomes white phase noise due to the measurement electronics.

We have also included the same measurement done without the DFB laser being injection locked (in blue) effectively showing how well the injection lock is working. The pink graph shows the phase noise of the free-running fiber laser (clock laser) effectively showing that the fiber laser's noise isn't the limiting factor of the measurement shown in blue (see subchapter 5.1.1).

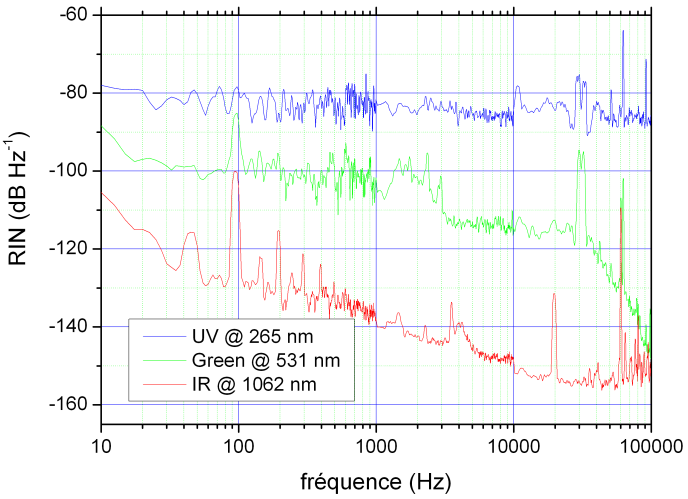

Figure 5.22: The relative intensity noise of the probe/clock beam before frequency doubling (IR), after the first frequency doubling (Green) and at 265.6 nm after the second frequency doubling (UV).

5.4.2 The frequency quadrupling.

Both frequency doubling stages are non-linear crystals inside folded bow-tie cavities. The first frequency doubling is done by a PPKTP (Periodically Poled Potassium Titanyl Phosphate) crystal chosen for its relatively high doubling efficiency and is effectively free of walk-off. The quasi phase match condition temperature is found near 40° C. The input coupler has a 92 % reflection rate while the three other mirrors has a 99.5 % reflection rate. With an (injection-locked) input power of 250 mW at 1062 nm we have obtained approximately 160 mW (64 %) of light at 531 nm.

The second frequency doubling is done by a BBO (beta barium borate) crystal with its phase matching condition being adjusted by angle tuning. With the much lower efficiency of the BBO crystal compared with the PPKTP crystal the input coupler has a higher reflection of 98.4 % with the rest of the mirrors having a 99.5 % reflection rate. The BBO is kept at an approximative temperature of 35° so to decrease moisture on the crystal. An input of 160 mW of 532 nm light led to 5 mw (3 %) of light at 265.6 nm.

In both cavities one of the mirrors is mounted on a piezo-electric el-

ement used for locking the cavity. For each cavity a photodiode behind one of the cavity mirrors detects a cavity leak which amounts to detecting the intra-cavity power. The photodiode signals are both used to lock the cavities to cavity resonances by homodyne detection (see appendix B) with the modulation being applied directly to the cavity piezo's and with both cavities being modulated by the same 31.5 kHz oscillator.

Figure 5.22 shows the RIN (Relative Intensity Noise) of the light at the different stages of the frequency quadrupling. The injection locked DFB laser has a very low intensity noise of -120 - -140 dB corresponding to a relative noise of $10^{-7} - 10^{-6}$ in a 1 Hz bandwidth. The two doubling stages add a significant amount of intensity noise but in the end a relative intensity noise of -80 dB (10^{-4}) should not pose any problems regarding measurements of the clock transition. The 31.5 kHz homodyne detection modulation is clearly visible but does not seem to add significantly to the overall RIN of the UV light compared with the noise at lower frequencies. The green light's strong decrease in noise above 30 kHz is due to a filtering photo-diode. To avoid the 31.5 kHz it might be necessary to lock the doubling cavities with the Hänsch-Couillaud method [Hänsch and Couillaud, 1980] when reaching for a high performance optical lattice clock.

To conclude this chapter we show figure 5.23 which shows the *expected* frequency noise level of the clock beam at 1062.5 nm in a best case scenario in which the cavity noise is limited by thermal flicker noise around 1 Hz at the level earlier calculated corresponding to an instability of $3{\cdot}10^{-16}$ (in red), in which we can lock the clock signal to the atomic clock transition every second (in black) and in which we are not limited by additional noise except for the measured Pound-Drever-Hall servo-loop electronic noise. This shows that for frequencies higher than $\sim$ 17 Hz we are limited by the servo-loop noise (in blue) until the locking bandwidth around 600 kHz after which the frequency noise would be limited by the laser noise which seems to be of flicker type noise at this point (in green). Using that [Vanier and Audoin, 1989]

$$\sigma_y^2(\tau) = \int_0^\infty S_y(f)|H(f)|^2 \mathrm{d}f \tag{5.4.1}$$

with $H(f)$ given by

$$|H(f)|^2 = 2\frac{\sin^4(\pi f\tau)}{(\pi f\tau)^2}, \tag{5.4.2}$$

we estimate the corresponding expected instability to be as shown in figure 5.24. This shows a relative instability of less than $2 \cdot 10^{-16}$, but recall that this is just an expected noise level for the clock beam in the infrared in an optimistic scenario.

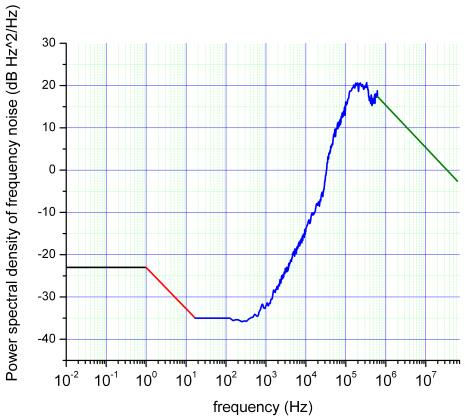

Figure 5.23: The expected frequency noise of the clock beam at 1062.5 nm in an optimistic scenario.

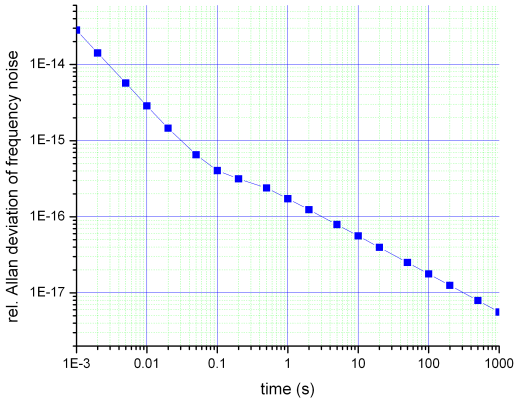

Figure 5.24: The expected instability of the clock beam at 1062.5 nm in an optimistic scenario.

Chapter 6

Probing the clock transition

6.1 Searching for the clock transition

The first step in doing a preliminary measurement of the clock transition frequency was to narrow down the clock frequency so to better optimize the setup used for a more precise measurement and ease the search for the transition on trapped atoms.

Earlier spectroscopic measurements of mercury have indirectly given an estimate for the $^3P_0$ state energy of mercury and thereby the transition frequency. The compilation made by [Saloman, 2006] gave a "natural-isotopic-mixture" energy level which corresponds to a transition frequency of 1.1285681 PHz while an earlier made compilation [Burns and Adams, 1952] estimated energy levels for ^{199}Hg and ^{201}Hg to be 1.1285751 PHz and 1.1285694 PHz respectively. These last values were used as a starting point for the search and we estimated a region to search of ± 1 GHz in the UV or ± 250 MHz in the IR.

The scanning range of a typical IR AOM is at most 100 MHz and for the UV versions it is even lower. We did not have enough AOM's to cover the whole range and since the output angle of an AOM output depends on the frequency it would easily become cumbersome to use a number of AOM's in serial to scan the frequency. Another solution would have been to phaselock the DFB (probe) laser to the clock laser instead of using injection locking and then sweep the frequency by offset of the phase lock. But due to insufficient bandwidth due to the DFB laser itself we could not get the line width below 50 kHz which would have meant a line width of more than 800 kHz in the UV due to the noise observed being white frequency noise.

To gain enough sweeping range we opted for the solution of locking the fiber laser itself directly to one of the femto laser frequency comb lines and then sweep the comb line frequency by controlling the comb line interval as shown in figure 6.1. This way we could do a continuous sweep of more than a GHz (in the IR) and by changing comb-line we would have an almost infinite frequency range (limited by the injection lock of the DFB probe laser and the frequency range of the fiber laser).[1] The line width in this case is the one of the fiber laser.

To lock the fiber laser to a comb line we measured the beat note between the laser and the closest comb line on a photo-diode. The beat note signal was then mixed with the carrier envelop offset frequency of the femto laser so to remove the signal frequency's dependency on it. Yet another multiplication was done with a 277 MHz DDS (Direct Digital Synthesis)[2] signal so to create a (precisely known) frequency offset between the laser and the comb line frequency. A frequency division (not shown in figure 6.1) preceded a frequency-to-voltage converter. The following integrator circuit locked the laser frequency by control of the fiber lasers piezo to the comb line frequency offset by the DDS frequency and with a bandwidth of about 100 Hz.

We measured the comb line interval f_r by measuring the beat note of two neighboring comb lines on a photodiode, which, as mentioned earlier, gave $f_r \approx 765$ MHz. We furthermore used the 12th harmonic's beat note with the 9.2 GHz microwave reference from the CSO and a PC-controlled 56 MHz DDS to phaselock the repetition rate, to have a link with a known frequency reference and to control f_r from a PC.

The fiber laser light, now locked to a frequency comb line, was injected directly into the DFB probe laser via an AOM later used for doing the more precise measurements (see next subchapter). The twice frequency doubled probe light was sent with a small angle with the vertical up through the MOT in the vacuum chamber (as shown in figure 6.2). To align the clock beam with the MOT we aligned it with the probe beam used for absorption measurements (see chapter 4.3).

During this search phase (done on ^{199}Hg) we had continuously trapped

[1] In this scheme we could change comb-line by manually changing the fiber laser temperature.

[2] All DDS's in this setup and the setup described in the next sub-chapter are referenced to the 1 GHz reference from the CSO.

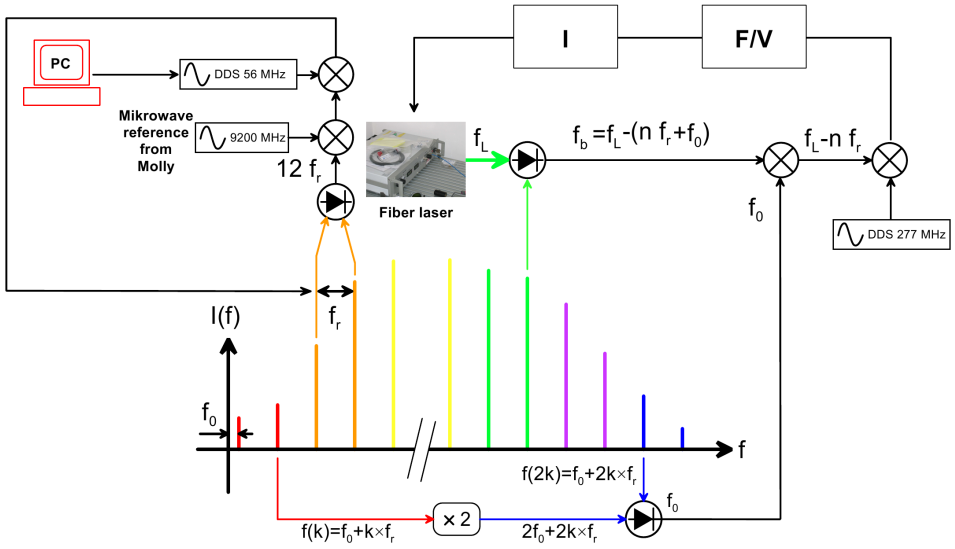

Figure 6.1: This shows how the femto-second frequency comb was used to enhance the searching range while searching for the clock transition. The fiber laser was directly locked to a comb-line, whose frequency was controlled by locking the comb-line interval f_r to a PC-controlled DDS. The actual frequency is obtained since the 12th harmonic of the comb interval is beat against the 9.2 GHz microwave reference from CSO. Notice how the offset frequency is directly subtracted from the fiber laser/comb-line beat note so the knowledge of the frequency can be obtained.

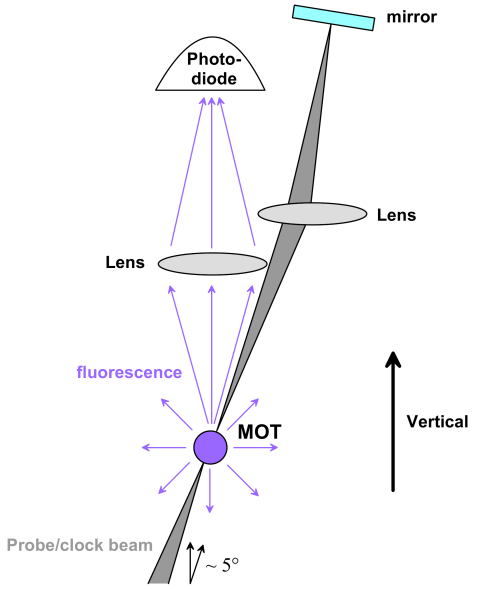

Figure 6.2: The setup for probing and detecting the clock transition. The mirror was added when doing more precise measurements (see subchapter 6.2.2.)

atoms in the MOT.

This phase of the search for the clock frequency was done by measuring on atoms trapped in the MOT. It was done on ^{199}Hg. Assuming that the clock transition lifetime for ^{199}Hg is 2.22 s (as measured by [Bigeon, 1967]) and a probe beam power of about 2 mW (beam waist $\sim$ 0.120 x 0.600 mm) the clock transition Rabi frequency was about 3 kHz, that is a Rabi cycling time of 330 μs. Due to the gravitational field atoms might not make a full rabi cycle on the clock transition. An atom in the $^3P_0$ state is not under influence of the cooling transition and falls freely under gravity. If estimating that an atom spends half its Rabi cycle in the excited state an atom would be in the $^3P_0$ state for 165 μs. During this time-period it does not have the time to move out of the trapping region but since its velocity along the gravitational field changes and since we probe along this, the atom's resonance frequency is Doppler shifted. This Doppler shift due to the gravitational acceleration is

$$\Delta\nu_g = \Delta v/\lambda = gt/\lambda, \tag{6.1.1}$$

where $g = 9.81$ m/s^2 is the gravitational acceleration, λ the transition wavelength and t the time spent in free fall and we get a shift of about 37 MHz/s and 6 kHz for our atom. The clock transition's natural line width

is strongly saturated and the transition is therefore power broadened such that the effective line width for the transition is

$$\gamma' = \gamma\sqrt{1 + I/I_{sat}} \simeq \sqrt{2}\Omega_R. \tag{6.1.2}$$

In the situation presented here the power broadened line width was about 4.3 kHz.

Since the Doppler shift due to gravitational acceleration is estimated to be of the same order of magnitude as the power broadened line width it can be assumed that a large fraction of atoms gets so much out of resonance with the transition when in $^3P_0$ that they effectively stop Rabi cycling and falls out of the MOT trap region [Courtillot et al., 2003].[3] So if the probe beam is at the clock transition frequency it is assumed that it would deplete atoms from the MOT due to (some) atoms stop Rabi cycling when in $^3P_0$ as they are Doppler shifted by gravitational acceleration.

After rigorous searching, the clock transition was found at about 1128.557 THz (see figure 6.3). Of course this value was not very precise due to among others light shift from the cooling light, Doppler broadening and saturation effects due to a complete depletion of the MOT.

6.2 Doppler-free measurement of the clock transition frequency

Now that we had found an approximate clock frequency one of the first things to change was the way we linked to the microwave reference to CSO and how we measured the frequency so to have a more reliable and accurate determination of the fiber laser frequency.

6.2.1 Frequency comparison

Instead of locking the fiber laser to a (controllable) comb line we now locked it to the ultra stable cavity as described in subchapter 5.1.6. Since the preliminary clock frequency was within 120 MHz of a cavity mode only a single 176 MHz AOM in the IR was used to reach the ^{199}Hg clock frequency

[3] The natural lifetime of the clock transition is of the order of 2 s, in which, an atom can fall almost 20 m, so there is a very small probability that the atom will naturally decay back to the ground state before it is out of the trap region.

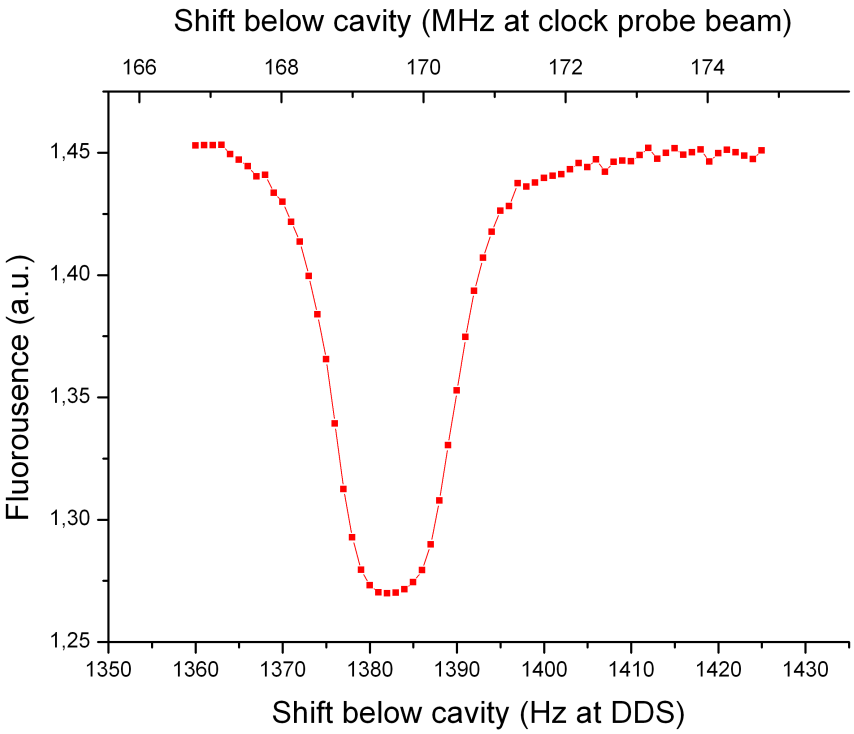

Figure 6.3: The first laser spectroscopic measurement of the neutral mercury clock transition. The lower x-axis is the PC-controlled DDS frequency in units of Hz with zero being the ultra-stable cavity resonance. The upper x-axis shows the conversion into the corresponding clock frequency (still with zero being the cavity resonance).

(for ^{201}Hg we used a 240 MHz AOM), which also was used to scan the frequency around the transition. This was in addition to the -180 MHz UV AOM used for switching the probe beam placed right before entering the vacuum chamber. The AOM frequency is controlled by a RF synthesizer referenced to the 1 GHz reference from the CSO. Since the cavity has a rather low and stable drift of 6 kHz/day (in the IR) and has shown a stable and predictable behavior within the present uncertainty ($\sim$5 kHz), we can use the clock without using the femto-second frequency comb to link with the microwave reference even on a daily basis. By locking to the ultra-stable cavity we also probe with a laser with a very narrow line width ($\sim$Hz) compared with the 3.3 kHz line width (in the IR) when locking to the frequency comb.

To measure the actual frequency and to monitor the drift of our ultra-stable cavity we still had to link to the microwave reference once in a while. This was done using the setup shown in figure 6.4. The beat note between the fiber laser locked to a cavity mode and a frequency comb line is measured on a photo-diode. Just as in the search phase we subtract the carrier envelope offset frequency (obtained the same way) and a 320 MHz DDS signal. The resulting signal is used to lock the comb line to the laser frequency (minus the DDS and offset frequency) by control of the comb repetition rate. The 12th harmonic of the repetition rate is detected by a photo-diode and then mixed with the 9.2 GHz microwave reference and a 56 MHz DDS signal. The 275 kHz signal was then multiplied by 200 so to attain the frequency range of the frequency counter used to measure the frequency. This measurement process has a short term stability of $\sim 5 \cdot 10^{-15}$ over one second.

6.2.2 The measurement cycle

We wanted to first of all remove the light shift from the MOT by making measurements of atoms in free fall instead of atoms continuously trapped in a MOT. This was done by introducing a measurement cycle, not unlike the one used for measuring the number of trapped atoms by absorption. The MOT gets turned off before the clock beam used to excite atoms on the clock transition is turned on for a short period and then finally the MOT is turned on again to recapture non-excited atoms which fluorescence is used as a measure of the clock transition. A good example of the measured

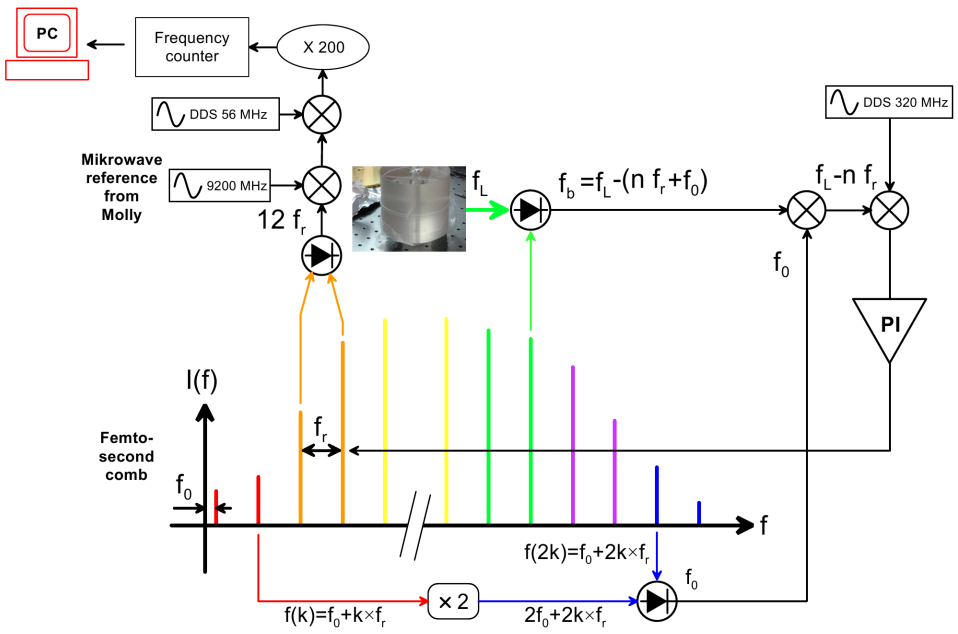

Figure 6.4: The setup for using the femto-second comb to measure the clock frequency precisely by linking the ultrastable cavity at 1062 nm to the 9.2 GHz microwave reference from CSO. A comb-line was locked to the ultra-stable cavity by control of the repetition rate f_r. The repetition rate itself is measured by beating its 12th harmonic with the 9.2 GHz microwave reference and a DDS with a well-known frequency and then measure the final beat-note with a frequency counter.

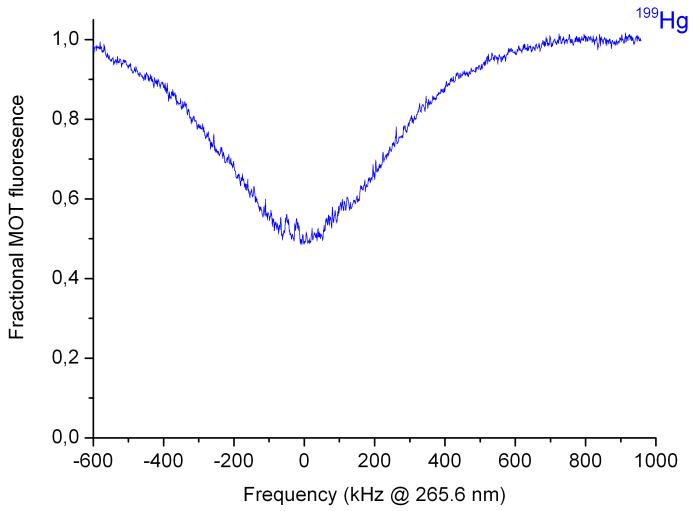

Figure 6.5: The MOT-free Doppler profile of the 265.6 nm clock transition of ^{199}Hg. In the bottom of the 580 kHz wide profile it is possible to ascertain the Doppler-free recoil doublet.

MOT-free Doppler profile of the ^{199}Hg clock transition is shown in figure 6.5. From observed Doppler widths (FWHM) between 360 kHz and 550 kHz (on single pass of the probe beam) we have estimated the temperature of the MOT to be between 36 μK and 84 μK. This can be compared with the cooling transition's Doppler temperature of 31 μK.

The MOT is switched by switching both the cooling light (with the galva driven shutter) and the magnetic field. The MOT is on for 20 - 50 ms and off for 5 ms. In the present configuration (the one described in chapter 4.3) the MOT and the 2D-MOT are both switched at the same time. While the MOT is off the atoms only fall 123 μm, their cooling transition (along the vertical direction) is detuned by 185 kHz (much smaller than the 1.3 MHz natural line width of the cooling transition) and even at the highest observed MOT temperature of 84 μK the RMS velocity is 10.2 cm/s and the atomic cloud will expand 513 μm.[4] When turning on the MOT again after 5 ms most atoms would therefore be re-captured. In practice this cycle was run one after another so a steady state of number of atoms in the MOT

[4]This expansion is given in terms of the three-dimensional RMS expansion. The one-dimensional RMS expansion is 296 μm. The conclusion is the same.

was reached and it is the average fluorescence over about one second that is measured.

0.2 ms into the 5 ms, during which the MOT is turned off, the probe light gets turned on for 0.5 ms. The probe beam is switched by the aforementioned -180 MHz UV AOM placed just after the frequency doubling cavities. In the 0.7 ms that an atom falls freely before the clock beam is turned off the transition frequency along the vertical is Doppler shifted due to the gravitational acceleration by about 25 kHz.

We retro-reflected the clock beam back into the MOT (as shown in figure 6.2) so to interact on the clock transition with two counter-propagating beams. The aforementioned shift would show up as two Doppler profiles both distanced from the true transition frequency by the gravitational accelerated Doppler shift but with opposite signs. The clock transition could then be deduced from the average of the two Doppler broadened transition profiles.

But more importantly the double-passing of the clock beam allows for the presence of a Doppler-free saturation absorption recoil doublet [Hall et al., 1976]. To be able to see Doppler-free features we decreased the size of the probe beam to a 0.7 x 0.12 mm waist. Notice that the beam size is smaller than the estimated MOT size.

6.2.3 The recoil doublet

The gravitational accelerated Doppler shift is rather small compared to the width of the Doppler widen absorption peak ($\gtrsim 360$ kHz) and we therefore only observe a single peak with double the depth on a double pass of the clock laser compared with a single pass.

Due to the recoil of an atom when absorbing or emitting a photon the excitation and stimulated emission is resonant at a slightly shifted frequency compared with the one given by the energy difference between the two transition energy levels. If an atom with momentum $p = mv$ along the beam direction absorbs a photon of frequency ν it will gain the photons momentum $\hbar k$ with $k = 2\pi\nu/c$ being the wave number (see figure 6.6). The energy of the photon must cover both the internal atomic energy shift

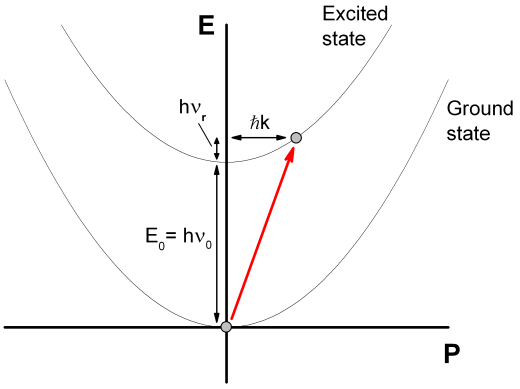

Figure 6.6: The (one-dimensional) momentum-energy diagram of a two-level atom at rest interacting with a single beam of light at the recoil shifted resonance frequency $\nu = \nu_0 + \nu_r$ of a transition. The red arrow symbolizes the absorption of a photon.

$E_0 = h\nu_0$ and the change in kinetic energy due to the recoil:

$$\begin{aligned} E_{photon} = h\nu &= h\nu_0 + \frac{(p+\hbar k)^2}{2m} - \frac{p^2}{2m} \\ &= h\nu_0 + \frac{\hbar k p}{m} + \frac{\hbar^2 k^2}{2m} \\ &= h\nu_0 + \hbar k v + \frac{h^2\nu^2}{2mc^2}. \end{aligned} \tag{6.2.1}$$

The second term is the Doppler shift while the third term is the recoil shift:[5]

$$\nu_r = \frac{h}{2mc^2}\nu^2 = \frac{h}{2mc^2}(\nu_0 + \nu_r)^2 \approx \frac{h}{2mc^2}\nu_0^2. \tag{6.2.2}$$

For stimulated emission it is the atom's transition energy that has to cover both the change in velocity and the photon energy:

$$E_0 = h\nu_0 = h\nu + \frac{(p+\hbar k)^2}{2m} - \frac{p^2}{2m}. \tag{6.2.3}$$

This means that the recoil shift from stimulated emission has a changed sign compared with the recoil shift from absorption.

[5] We can use the approximation $(\nu_r + \nu_0)^2 \approx \nu_0^2$ since we know that the recoil shift is of the order of kHz and this approximation therefore has a relative error of -24 order of magnitudes, which means in the order of nHz.

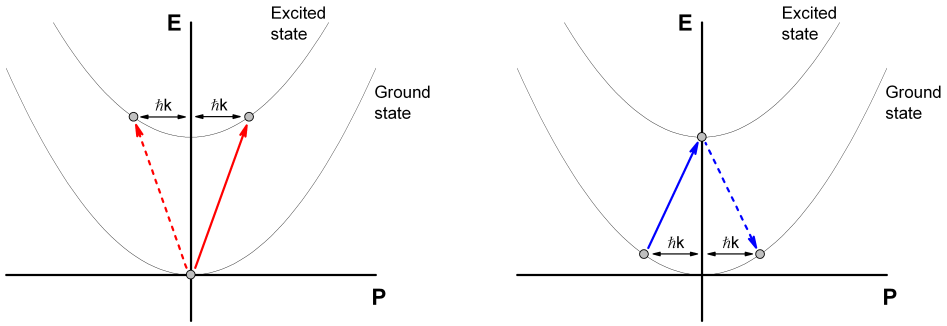

Figure 6.7: (One-dimensional) momentum-energy diagrams when two counter-propagating beams interacts with a two-level atom. The dashed line shows the interaction with the return beam. In two situations can the two beams (having the same frequency) interact with the same velocity class of atoms and therefore make saturated absorption possible: (a) The frequency is $\nu_0 + \nu_r$. Both beams are interacting with ground-state atoms at rest (along the beam direction). The red arrows symbolizes the possible absorptions of a single photon (b) The frequency is $\nu_0 - \nu_r$. The blue arrows symbolizes the mechanic in which atoms are less prone to end up in the excited state due to the two beams interacting with the same (excited) velocity class of atoms. The atoms absorbs a photon from one beam and stimulate emits a photon into the other beam.

Since we use two counter-propagating beams the situation is a bit more complicated. For most frequencies the two counter-propagating clock beams interacts with different velocity classes of atoms. But in two situations (shown in figure 6.7) it is not the case. In the case where the clock laser frequency is in resonance with the recoil shifted transition frequency (figure 6.7(a)) both beams address ground state atoms at rest (along beam direction). If the beams were not addressing the same class of atoms they could each excite from their separate pools each of N atoms. But in this case they have to share the same pool of N ground state atoms so instead of having a total pool of $2N$ ground state atoms addressed by the beams there is only N atoms and consequently less atoms ends up in the exited state. By scanning the frequency we expect to observe a saturated absorption type peak free of the Doppler effect at the recoil shifted transition frequency. If the clock laser frequency instead is recoil shifted the opposite way from the transition frequency (see figure 6.7(b)) the two beams address the same velocity class

of excited atoms - also atoms at rest (along beam direction). By having the beams address the same velocity class of exited atoms, atoms can now be excited by one of the beams and then stimulate emit photons into the other beam. Again less atoms would end up in the exited state and we expect a saturated absorption type peak at the transition frequency minus the recoil shift. Since this doublet is at frequencies $\nu_0 + \nu_r$ and $\nu_0 - \nu_r$ an average of the two peak centers would give the recoil-free atomic transition frequency.

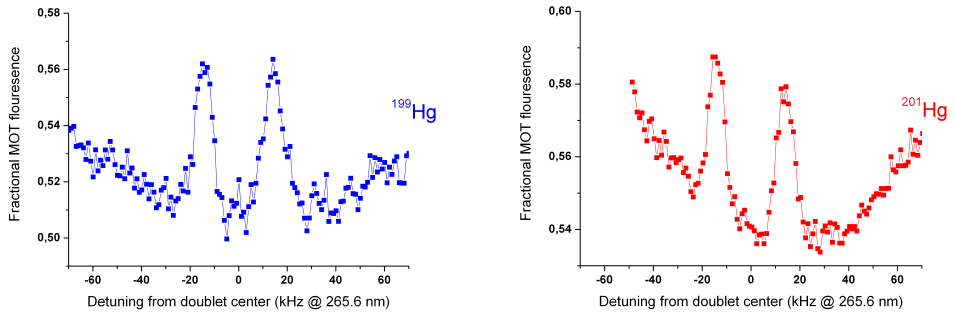

(a) (b)

Figure 6.8: The Doppler-free recoil doublet of the clock transition for the two mercury fermions. The frequency zero is at the average value of the two peak centers. The peaks all have a FWHM of about 9 kHz.

We have managed to see this doublet for both fermions as shown in figure 6.8. Figure 6.9 shows doublets measured with different probe durations and how the width of the peaks increases with the duration. This is due to the atoms being accelerated by gravity during the probing. This effect does not induce a total shift in frequency. For both fermions a HWHM of 4.5 kHz of the peaks could be observed and so far we use this as a (conservative) measure of the uncertainty of the position of each peak. When the MOT's magnetic fields are turned off, which indeed is the case during these measurements, there is still a 2-3 G magnetic field present around the MOT-chamber, mostly due to the un-shielded ion-pump magnet. From table 2.4 and 2.5 in subsection 2.3.2 we see if the magnetic field is no more than 3 G the first order Zeeman effect should be less than 3.3 kHz for ^{199}Hg and 2.0 kHz for ^{199}Hg.

The average of the two peaks gave respectively $\nu(^{199}\text{Hg}) = 1128.575290808.4$ THz with an estimated uncertainty of 5.6 kHz and $\nu(^{201}\text{Hg}) = 1128.569561139.6$

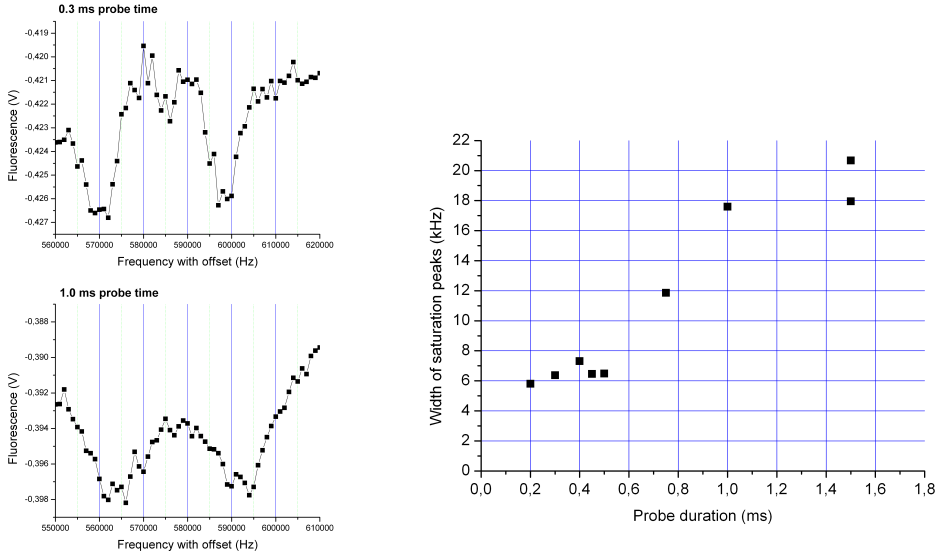

(a) (b)

Figure 6.9: (a) The recoil doublets with respectively 0.3 ms and 1.0 ms of probe time. (b) The $1/e^2$ width of the recoil peaks for different probe durations.

THz with an estimated uncertainty of 4.9 kHz. This is a fractional uncertainty of $5 \cdot 10^{-12}$. The result fits the earlier reported results from [Burns and Adams, 1952] with an improvement of more than four orders of magnitude. From the above the isotope shift between the two fermions is 5.729668 GHz with an uncertainty of 7.4 kHz. All the uncertainties are calculated by taking the square root of the sum of the squared uncertainties involved.

Chapter 7

Conclusion

This thesis has detailed the first experimental results of the first 3 years of the neutral mercury lattice clock project at SYRTE in Paris. Starting from an empty lab one of the world's first magneto-optical traps with neutral mercury was achieved and the first Doppler-free spectroscopy of the mercury clock transition was made (as shown in figure 7.1).

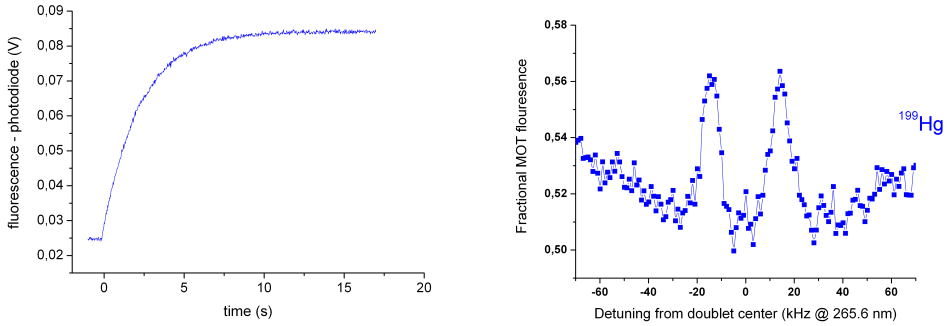

(a) (b)

Figure 7.1: The major results presented in this thesis:(a) The loading of a ^{202}Hg MOT demonstrating the assembling of a neutral mercury MOT and (b) the ^{199}Hg recoil doublet of mercury in free fall, which allowed for the Doppler-free spectroscopy of the neutral mercury fermions.

One of the first achievements was to obtain several hundred mW of laser power at the cooling wavelength at 253.7 nm far into the UV. We have shown that it is possible to obtain up to 800 mW with a twice frequency doubled Yb:YAG disc-laser, although damage to optics sustained at these

low wavelengths causes decreasing power levels over time. The disc-laser itself has proven itself to be a challenge but over the course of several years (including a 10 month pit-stop at its factory) satisfying control over it was exhibited. It can now be locked to the approximately 1.3 MHz Doppler-free mercury cooling transition obtained by saturated spectroscopy of a mercury vapour cell with an estimated linewidth of 27 kHz at 254 nm. This is probably the first time that a high-power Yb:YAG disc-laser frequency noise was characterized and stabilized to that level.

With this cooling light a neutral mercury magneto-optical trap using a 2D-MOT pre-selection scheme has been obtained. This has been done for both mercury fermions ^{199}Hg, ^{201}Hg and for a single boson ^{202}Hg. Life-times of the mercury MOTs of more than 2 seconds have been demonstrated while spectroscopy of the mercury clock transition on the fermions indicate temperatures as low as 36 μK, slightly above the 31 μK cooling transition Doppler temperature. The novel mercury source allowed for adequate control of mercury pressure.

We have performed the first laser spectroscopy of the mercury fermions $^1S_0 - ^3P_0$ clock transition. By probing the clock transition recoil doublet of the cooled atoms in free fall, it was possible to determine the atomic clock frequency of the fermions with an uncertainty of less than 6 kHz corresponding to a relative uncertainty of about $5 \cdot 10^{-12}$ improving previous indirect measurement by at least 4 order magnitudes. The clock probe beam at 265.6 nm was obtained by having a 3 kHz fiber laser at 1062.5 nm locked to an ultra-stable cavity with a 1.8 kHz line width and injected into a slave laser which then was frequency doubled twice.

In the attempt to obtain the narrowest possible probe we have tried to limit the ultra-stable cavity noise to thermal noise and we have done the first serious attempt of using fused silica mirrors on an ultra-stable cavity. Due to thermal stabilization and shielding we have obtained a good mid-term ($\sim$1000 s) stability. The cavity has shown a relative instability of no more than $8 \cdot 10^{-16}$ at one second when comparing with a similar cavity. This is the second best result after the seminal and yet unbeaten work of [Young et al., 1999a] which reported a stability of $3 \cdot 10^{-16}$ at one second with 25 cm long cavity.

The next step for this project is to establish a dipole trap at the magic wavelength and transfer atoms from the MOT to the dipole trap. The power issue for the cooling light has to be taken care of by changing damaged optics

and possibly change the configuration of the second doubling cavity. An enlargement of the 2D-MOT region is also planned to increase the number of atoms in the MOT. Tests of the fiber noise cancellation indicate that fiber noise should not be an issue for the probe beam while tests of the injection lock indicate a possible issue with air flow which can be solved by encasing this part of the experiment in a box.

At this point our project is taking the lead for the realization of a neutral mercury lattice clock being the first to measure the mercury fermion clock frequencies with a relative accuracy in the 10^{-12}. So far it has been demonstrated that neutral mercury can be laser-cooled and trapped under vacuum conditions and the generation of sufficiently powerful and reliable laser-sources for both cooling and probing the clock transition is possible. In parallel, we have shown that it is possible to reach stabilities at 1 second of less than 10^{-15} using a ULE cavity with fused silica mirrors. We consider the cavity largely sufficient for future clock operation.

In the introduction it was mentioned that at some point another atomic species could replace Cs for use as the definition of the second. Neutral mercury could be one of these and the project has so far overcome a number of expected challenges with using this species.

With uncertainties in the low 10^{-17} and instabilities in the mid 10^{-15} at one second the optical single ion clocks has surpassed microwave atomic fountains (see table 1.1). Now the ion clocks has to show liability and stability on the long term to show that optical clocks indeed can be an improvement compared to microwave clocks for practical applications. After only a few years of development, optical lattice clocks have shown great promise with uncertainties as low as $1.5 \cdot 10^{-16}$ and instabilities of $3 \cdot 10^{-15}$ at one second which also surpasses what has been obtained by fountain clocks. We have added mercury to the list of atoms that will be used in an optical lattice clock and even though we have a long road ahead of us we are confident that the mercury optical lattice clock will be among the clocks surpassing the microwave atomic fountains and possibly be among the best performing clocks.

Appendix A

Atomic flux through a flat surface

When considering the flux of atoms through a flat surface (we are only considering atoms moving through from one side) it is easiest to first consider the flux of atoms with a specific velocity v along the direction perpendicular to the surface. If the surface in question has an area A figure A.1 shows that in a (small) time period $\mathrm{d}t$, $\rho_v \cdot Av\mathrm{d}t$ atoms will cross the surface, where ρ_v is the density of atoms having a velocity v perpendicular to the surface. In most cases it can be assumed that the gas of atoms is an ideal gas with a Maxwell-Boltzmann distribution of velocities so that

$$\rho_v = \frac{P}{k_B T}\sqrt{\frac{m}{2\pi k_B T}} e^{-\frac{mv^2}{2k_B T}}, \tag{A.0.1}$$

where P is the pressure of the gas, k_B Boltzmann's constant, T the temperature of the gas of atoms and m the mass of a single atom. Here we used that $\sqrt{m/2\pi k_B T}$ is the normalization factor for the Maxwell-Boltzmann distribution of velocities in one dimension. The flux per area f_v of atoms having a velocity v perpendicular to the flat surface is then

$$f_v = \frac{P}{k_B T}\sqrt{\frac{m}{2\pi k_B T}} \cdot v e^{-\frac{mv^2}{2k_B T}}. \tag{A.0.2}$$

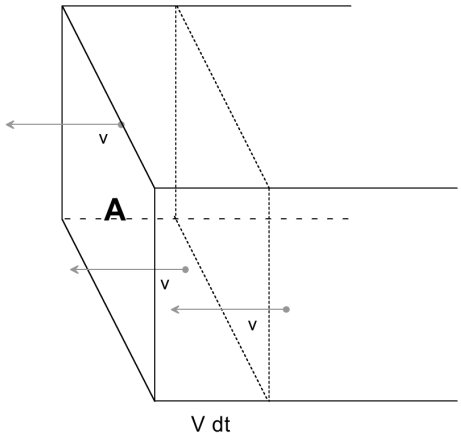

Figure A.1: Imagine the flux of atoms through a surface (of area A) during a small time-period dt when considering only atoms having a certain velocity v perpendicular to the surface.

To obtain the total flux per area f we just have to integrate over all positive velocities[1]:

$$\begin{aligned} f =& \frac{P}{k_B T}\sqrt{\frac{m}{2\pi k_B T}} \cdot \int_0^\infty v e^{-\frac{mv^2}{2k_B T}} \mathrm{d}v \\ =& \frac{P}{k_B T}\sqrt{\frac{m}{2\pi k_B T}} \cdot \frac{k_B T}{m} \\ =& P \cdot \sqrt{\frac{1}{2\pi m k_B T}}. \end{aligned} \tag{A.0.3}$$

[1] We consider atoms moving towards the surface as having a positive velocity so atoms with a negative velocity is moving away from the surface

Appendix B

Homodyne detection

In many experimental systems it is necessary to lock to a peak of a signal measured on the system itself (for example locking a laser's frequency to an atomic transition or locking a cavity resonance to a lasers frequency). One classical method to this is to make a homodyne detection of the peak. I will here give a short introduction to this method.

The principle of this method is to modulate the experimental system such that the measurement of the system crosses the peak we want to lock on and then use the differentiator of the signal as the error-signal used to locked upon.

Figure B.1 shows a general schematic for locking a system by homodyne detection where the electronic controller is what is used to electronically sweep and lock the experimental system (f.ex. an voltage-controlled oscillator to control an acoustic-optic modulator). If the oscillator has a frequency

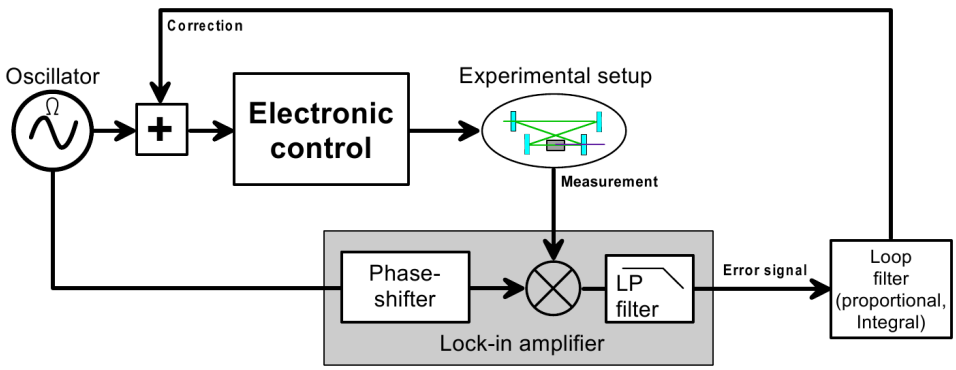

Figure B.1: A general schematic for locking by homodyne detection.

Ω then the signal sent towards the experiment is of the form

$$\nu_0 + A\cos(\Omega t). \tag{B.0.1}$$

If ν is the variable we are measuring and the oscillation amplitude A is much smaller than ν_0 then to first order measurement of the system would yield a signal of the form

$$f(\nu_0 + A\cos(\Omega t)) \simeq f(\nu_0) + A\frac{\mathrm{d}f(\nu_0)}{\mathrm{d}\nu}\cos(\Omega t), \tag{B.0.2}$$

where f is a transfer function of the system and the measurement. The signal sent through the phase shifter is of the form

$$B\cos(\Omega t + \varphi) \tag{B.0.3}$$

with φ is the phase difference between the two signals entering the mixer. The output of the (perfect) mixer has the form

$$Af(\nu_0)\cos(\Omega t) - AB\frac{\mathrm{d}f(\nu_0)}{\mathrm{d}\nu}\big(\cos(2\Omega t + \varphi) + \cos\varphi\big). \tag{B.0.4}$$

A suitable chosen low-pass filter filters the Ω and 2Ω frequency components and we are left with a simple signal of the form

$$C\frac{\mathrm{d}f(\nu_0)}{\mathrm{d}\nu}\cos\varphi \tag{B.0.5}$$

which is zero at the peak value of our measurement and´can be used as an error signal for the proportional and/or integrating locking filter.

It is typical to use a lock-in amplifier which contains a controllable phase-shifter, a mixer and some filtering. The phase shifter is obviously used to make $\cos\varphi \sim 1$ so to maximize the error signal (and to have a correct sign on the correction signal). Notice that the filtering of Ω might be a limit on the locking bandwidth and it is therefore important to choose an modulation frequency high enough (and an equally high frequency LP filter) to not pose a problem regarding the bandwidth. At the same time there might be bandwidth limits on the measurement equipment (such as a photo-diode) that can limit the modulation frequency from above.

Appendix C

Obtaining the frequency noise power spectral density with a spectrum analyzer

Often it is not possible to measure the high frequency (RF) noise with a dynamic signal analyzer. The noise at much higher (Fourier) frequencies can be measured using a (power noise) spectral analyzer but those do not output the (frequency) power spectral density directly by doing digital fast fourier transformation as is done by dynamic signal analyzers. In the following I will shortly derive the equation used to calculate the frequency noise power spectral density from spectrum analyzer measurements of a sinusoidal signal under the assumption that we are measuring far away from the carrier frequency.

We are considering a sinusoidal signal which can be written using complex notation

$$s(t) = Ae^{-i(2\pi\nu_0 t + \delta\varphi(t))}, \tag{C.0.1}$$

where $\delta\varphi(t)$ is the phase fluctuations of the signal (and where we ignore amplitude fluctuations). Figure C.1 shows the typical spectrum (in arbitrary units) measured by a spectrum analyzer around the carrier frequency ν_0 of such a signal. If we assume that

$$\left| \frac{1}{2\pi\nu_0} \frac{\mathrm{d}\delta\varphi}{\mathrm{d}t} \right| \ll 1 \tag{C.0.2}$$

we can write

$$s(t) \simeq Ae^{-i(2\pi\nu_0 t)}(1 - i\delta\varphi(t)). \tag{C.0.3}$$

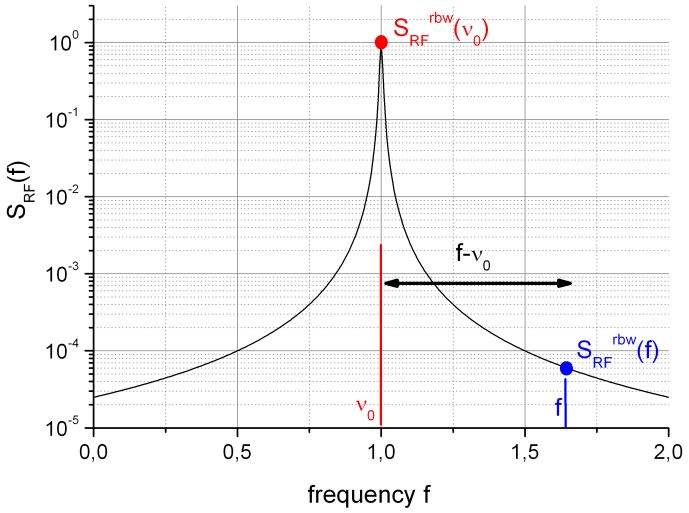

Figure C.1: Imaginary spectrum analyzer output of a periodic wave function with frequency ν_0 in some arbitrary units.

A spectrum analyzer measures the power under a linear filter typically centered on the Fourier-frequency in question. Let $H(f)$ be the transfer function of the filter at the frequency f defined such that $H_{max} = 1$. The filter's resolution bandwidth RBW is then defined as

$$RBW \equiv \int_{-\infty}^{\infty} |H(f)|^2 \mathrm{d}f. \tag{C.0.4}$$

If $S_{s(t)}$ is the one-sided power spectral density of the measured signal $s(t)$ the spectrum analyzer outputs

$$S_{RF}^{rbw}(f_c) = \int_0^{\infty} S_{s(t)}(f)|H(f - f_c)|^2 \mathrm{d}f. \tag{C.0.5}$$

By using a suitable narrow filter the spectrum analyzer scans the spectrum by scanning the filter's central frequency. In this deduction I assume that the filter is narrow enough that the power spectral density can be considered a constant function around the (central) filter frequency f_c when $|f - \nu_0| \ll RBW$ such that

$$S_{RF}^{rbw}(f_c) \approx S_{s(t)}(f_c) \int_0^{\infty} |H(f - f_c)|^2 \mathrm{d}f = S_{s(t)}(f_c) \cdot RBW. \tag{C.0.6}$$

It then becomes a question of estimating the $S_{s(t)}(f_c)$ as a function of $S_{\varphi(t)}$, which is the phase power spectral density of the signal obtained from the frequency power spectral density through

$$S_\nu(f) = f^2 S_{\delta\varphi}(f). \tag{C.0.7}$$

Measurements close to ν_0 should be dominated by the carrier frequency and in that case we can ignore the second part of (C.0.3). In this situation (C.0.6) is not true and the measurement just shows the filter since $S_{s(t)}(f)$ is a delta function. This way we get that $|A|^2 = S_{RF}^{rbw}(\nu_0)$, the measured value at the carrier frequency.

But we are considering frequencies far from the carrier frequency (where $|f - \nu_0| \gg RBW$) such that the carrier frequency and the first part of (C.0.3) can be ignored. If $\widetilde{\delta\varphi}(\nu)$ is the fourier transformation of $\delta\varphi(t)$ we can rewrite $e^{-i2\pi\nu_0 t}\delta\varphi(t)$ as follows

$$\begin{aligned} e^{-i2\pi\nu_0 t}\delta\varphi(t) &= e^{-i2\pi\nu_0 t}\int_0^\infty \widetilde{\delta\varphi}(\nu)\cos(2\pi\nu t)\,\mathrm{d}\nu \\ &= \frac{1}{2}\int_0^\infty \widetilde{\delta\varphi}(\nu)e^{-i2\pi(\nu+\nu_0)t}\,\mathrm{d}\nu + \frac{1}{2}\int_0^\infty \widetilde{\delta\varphi}(\nu')e^{-i2\pi(\nu'-\nu_0)t}\,\mathrm{d}\nu' \\ &= \frac{1}{2}\int_0^\infty \widetilde{\delta\varphi}(\nu-\nu_0)e^{-i2\pi\nu t}\,\mathrm{d}\nu + \frac{1}{2}\int_0^\infty \widetilde{\delta\varphi}(\nu'+\nu_0)e^{-i2\pi\nu' t}\,\mathrm{d}\nu', \end{aligned} \tag{C.0.8}$$

where we use the replacement $\nu \to \nu - \nu_0$ and $\nu' \to \nu' + \nu_0$ in the last equation. In this simplified derivation the spectrum of C.0.8 is estimated by looking at the energy of the function in C.0.8 at the fourier frequency ν in a filter with a bandwidth RBW. The spectrum of the first term can be interpreted as the phase power spectral density $S_{\delta\varphi}(f-\nu_0)$ at the frequency shifted by the carrier frequency. Since we are using a filter where $|f - \nu_0| \gg RBW$ the second term is filtered.

We now have the final formula:

$$S_{RF}^{rbw}(f) \simeq S_{RF}^{rbw}(\nu_0)S_{\delta\varphi}(f-\nu_0)\frac{RBW}{2}. \tag{C.0.9}$$

The rigorous treatment can be found in [Bahoura, 1998].

Appendix D

Publication: Doppler-Free Spectroscopy of the $^1S_0$-$^3P_0$ Optical Clock Transition in Laser-Cooled Fermionic Isotopes of Neutral Mercury

Doppler-Free Spectroscopy of the $^1S_0$-$^3P_0$ Optical Clock Transition in Laser-Cooled Fermionic Isotopes of Neutral Mercury

M. Petersen, R. Chicireanu, S. T. Dawkins, D. V. Magalhães,* C. Mandache,+ Y. Le Coq, A. Clairon, and S. Bize

LNE-SYRTE, Observatoire de Paris, 75014 Paris, France

(Received 17 July 2008; published 29 October 2008)

We report direct laser spectroscopy of the $^1S_0$-$^3P_0$ transition at 265.6 nm in fermionic isotopes of neutral mercury in a magneto-optical trap. Measurements of the frequency against the LNE-SYRTE primary reference using an optical frequency comb yield 1 128 575 290 808.4 ± 5.6 kHz in ^{199}Hg and 1 128 569 561 139.6 ± 5.3 kHz in ^{201}Hg. The uncertainty, allowed by the observation of the Doppler-free recoil doublet, is 4 orders of magnitude lower than previous indirect determinations. Mercury is a promising candidate for future optical lattice clocks due to its low sensitivity to blackbody radiation.

DOI: 10.1103/PhysRevLett.101.183004 PACS numbers: 32.30.Jc, 06.30.Ft, 37.10.−x, 42.62.Fi

The performance of optical atomic clocks is improving at a high pace. Optical clocks are now surpassing atomic fountain clocks based on microwave transitions [1–4]. Some optical transitions are now recognized as secondary representations of the unit of time of the international system of units (SI) opening the way to a new definition of the SI second based on an optical transition in the coming years. Atomic clocks also represent a powerful tool for testing fundamental physical laws. For instance, the stability of natural constants and thereby that of fundamental interactions (electro-weak, strong interaction) can be tested to high levels of precision, providing constraints that are independent of any assumption related to cosmological models [1,5–9]. Such tests provide precious experimental information to help in the search for unified theories of fundamental interactions.

Optical lattice clocks using strontium atoms have now demonstrated uncertainties at the 10^{-16} level [3], a factor of ~4 better than the best atomic fountains but still a factor of ~4 worse than the best optical single ion clock based on Hg^+ [1]. At this level of uncertainty, the blackbody radiation shift is the largest correction and the largest contribution to the strontium clock uncertainty. In future development, the blackbody radiation shift will remain a severe limitation to the accuracy at the 10^{-17} level. An optical clock using ytterbium [10] will have the same limitation since the blackbody shift is no more than a factor of 2 smaller in fractional terms [11]. In contrast, neutral mercury has been recognized as having a low sensitivity to blackbody radiation [12–14] while retaining all other desirable features for an optical lattice clock. Mercury has the potential to achieve uncertainty in the low 10^{-18} and therefore to compete with the best single ion optical clocks [1]. Mercury is also an interesting candidate in the search for variations of natural constants owing to its relatively high sensitivity to variations of the fine structure constant [15]. However, laser cooling of neutral mercury has been pursued and achieved only recently [14,16] due to the challenging requirement of deep-UV laser sources.

In this Letter, we report the first direct laser spectroscopy of the $^1S_0$-$^3P_0$ clock transition at 265.6 nm in the two naturally occurring fermionic isotopes of mercury ^{199}Hg and ^{201}Hg. Spectroscopy is performed on a sample of cold atoms released from a magneto-optical trap (MOT). With this approach, we resolve the Doppler-free recoil doublet allowing for a determination of the transition frequency with an uncertainty well under the Doppler-broadened linewidth. Absolute measurement of the frequency is performed using an optical frequency comb. ^{199}Hg and ^{201}Hg have natural abundances of 17.0 and 13.2%, respectively, and nuclear spins of $1/2$ and $3/2$. Their respective nuclear moments are $+0.5059$ and -0.5602 in units of nuclear magnetons [17]. ^{199}Hg can be considered as more favorable due to its higher abundance and lower nuclear spin. However, these advantages are not sufficient to discard ^{201}Hg as a possible candidate, so we have investigated both isotopes.

Figure 1 shows the low-lying energy levels of mercury. Mercury has an alkaline-earth-like electronic structure similar to those of strontium or ytterbium. In our experiment, laser cooling of mercury is achieved using the $^1S_0$-$^3P_1$ transition at 253.7 nm with a natural linewidth of 1.3 MHz. Cooling light is provided by quadrupling a Yb:YAG thin disk laser delivering up to 7 W of single frequency light at 1014.8 nm. A commercially available doubling stage using a temperature tuned LBO crystal within a bow-tie configuration buildup cavity generates up to 3 W of power at 507.4 nm. A second doubling stage uses a 90°-cut antireflection coated 7 mm long angle tuned BBO, also in a bow-tie configuration. Out-coupling of the second harmonic at 253.7 nm is achieved by using a harmonic separator mirror as one of the buildup cavity mirrors. Up to 800 mW of cw power has been generated with this system. In practice, the system is set to generate 100 to 150 mW in order to avoid the rapid degradation of the harmonic separator observed at higher output power. The frequency of this light is stabilized to the saturated absorption feature observed in a room temperature mercury vapor cell with a

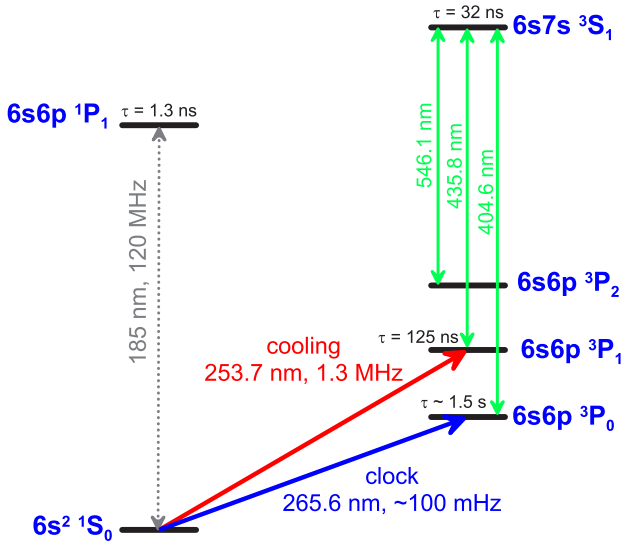

FIG. 1 (color online). Relevant energy levels of mercury. The $^1S_0$-$^3P_1$ transition at 253.7 nm is used for magneto-optical trapping. The clock transition studied in this Letter is the $^1S_0$-$^3P_0$ transition at 265.6 nm. The mentioned natural linewidth of ~100 mHz is for ^{199}Hg based on [23].

1 mm interaction length. The residual jitter is estimated to be less than 100 kHz which is suitably small compared to the 1.3 MHz natural linewidth of the cooling transition.

A 2 dimensional magneto-optical trap (2D-MOT) [18] is used to generate a slow atom beam which in turn is used to load a conventional MOT. A vapor pressure of $\sim 2 \times 10^{-7}$ mbar of mercury is kept in the 2D-MOT chamber by cooling a few grams of mercury held in a copper bowl down to $-55\,^{\circ}$C using a two stage Peltier element inside the vacuum chamber. The 2D-MOT is formed at the intersection of two orthogonal pairs of $\sigma^+ - \sigma^-$ polarized retro-reflected beams with a total power of ~50 mW. The longitudinal and transverse diameters at $1/e^2$ are ~10 mm and ~8 mm. The intersection overlaps with the center of a 2-dimensional quadrupole magnetic field with a gradient of 0.2 mT.mm^{-1} generated by 4 rectangularly shaped coils located outside the vacuum chamber. A 1.5 mm diameter and 10 mm long hole in the 2D-MOT chamber allows the beam of slow atoms confined at the center of the quadrupole field through, while providing high differential pumping between the 2D-MOT and the MOT chambers. The slow atom beam is directed toward the center of the MOT, 70 mm away from the output of the 2D-MOT. The MOT is generated at the intersection of three orthogonal pairs of retro-reflected $\sigma^+ - \sigma^-$ polarized laser beams with a diameter of ~6.6 mm and a power of ~15 mW each. Coils located outside the vacuum chamber generate the magnetic quadrupole field with a gradient of 0.15 mT.mm^{-1} along the strong axis. Our present setup forces the detuning of the 2D-MOT and the MOT to be the same. We find that a red detuning of -5.5 MHz corresponding to -4.3Γ optimizes the number of atoms in the MOT. Detection of the MOT is performed by collecting fluorescent light onto a low noise photodiode. Measurements with the most abundant ^{202}Hg isotope indicate that $\sim 5 \times 10^6$ atoms are captured with a loading time constant of 2.3 s. Further measurements of atom number based on absorption of a weak 253.7 nm probe are in agreement. ^{199}Hg and ^{201}Hg isotopes typically show slightly reduced atom numbers.

As shown in Fig. 2, laser light at 265.6 nm for probing the $^1S_0$-$^3P_0$ clock transition is generated by frequency quadrupling the 1062.5 nm output of a distributed feedback (DFB) laser diode delivering 250 mW of useful light. The first doubling is accomplished with 64% efficiency using a periodically poled KTP crystal and a bowtie buildup cavity, leading to 160 mW at 531.2 nm. The second doubling uses an angle-tuned 90°-cut antireflection coated BBO crystal and delivers up to 7 mW at 265.6 nm. The DFB laser diode is injection locked to an ultrastable laser source. As shown in Fig. 2, this laser source is composed of a Yb-doped DFB fiber laser stabilized to an ultrastable Fabry-Perot cavity. A fraction of the light is sent through an actively phase-stabilized fiber link to stabilize an optical frequency comb generated by a Ti:Sa femtosecond laser whose repetition rate is measured against the LNE-SYRTE flywheel oscillator [19], which is monitored by several primary fountain frequency standards. Repeated measurements of the ultrastable laser source revealed highly predictable behavior, relaxing the need for simultaneous operation of the optical frequency comb with the rest of the experiment at the current level of accuracy. Typically, measurements against the primary frequency reference were performed

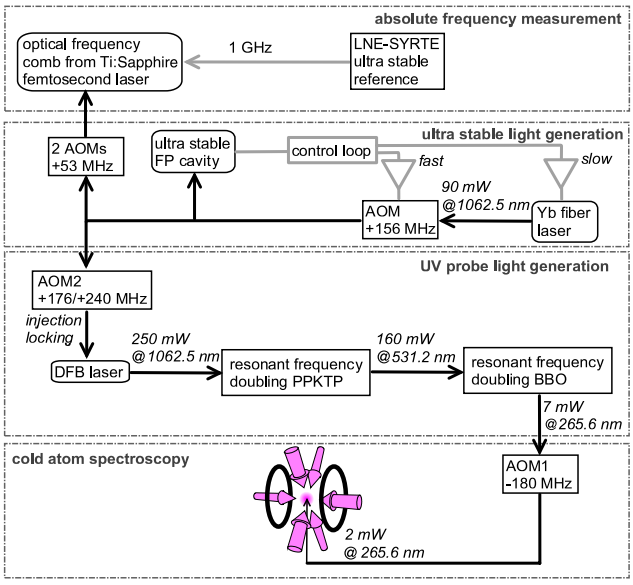

FIG. 2 (color online). Generation of the probe light at 265.6 nm and referencing to the primary frequency reference. AOM2 frequency depends on the isotope.

several times a day which is sufficient to estimate the optical frequency to better than 100 Hz at 1062.5 nm or 4 parts in 10^{13}. In fact, during the initial search for the clock transition, the Yb-doped fiber laser was stabilized to a component of the optical frequency comb, itself locked to the primary reference with a controllable offset to allow for broader scanning of the probe laser.

Spectroscopy of the clock transition is performed according to the scheme proposed and demonstrated with strontium [20] and further used with ytterbium [21]. An upgoing, linearly polarized probe beam crosses the MOT at its center and is either retro-reflected or not. Initially, the search for the clock transition was performed with both the MOT and the probe beam on continuously. Fluorescence of the MOT was monitored as a function of the probe frequency. Excitation of atoms to the untrapped, long-lived $^3P_0$ state by the probe laser and their subsequent fall under gravity induces losses in the MOT. Up to 90% depletion of the MOT has been observed. To suppress the light shift of ~300 kHz induced by the 253.7 nm MOT beams and perform accurate measurements, the following scheme is implemented. Using a mechanical shutter, the 2D-MOT and MOT beams are switched on for an adjustable duration of 20 to 50 ms then off for 5 ms. During the 5 ms, the probe light is pulsed once with adjustable delay and duration using acousto-optical modulator AOM1 in Fig. 2. This cycle is repeated continuously. The atoms are recaptured after the 5 ms since the atomic cloud falls under gravity by only 122 μm and expands by only 296 μm at the highest observed temperature of 84 μK. The MOT reaches a steady state determined by the loading rate during the MOT on time and the losses induced by the excitation to the $^3P_0$ state. The average fluorescence of the MOT is measured while stepping the probe frequency using AOM2 in Fig. 2.

Measurements were first taken with a 1.4×0.24 mm up-going probe beam. The maximum depletion of the MOT is ~50%. The observed peak is Doppler-broadened to a linewidth ranging from 360 to 550 kHz full-width at half maximum, depending on the MOT parameters including the quality of beam alignment. The lowest observed linewidth corresponds to a temperature of 36 μK, which is close to the Doppler temperature of 31 μK related to the natural linewidth of the cooling transition. Further measurements were performed with a retro-reflected probe beam in order to cancel the Doppler shift due to acceleration of the atoms under gravity and to a possible nonvanishing average velocity of the cloud released from the MOT. Comparisons of the frequency with single passed and retro-reflected beams first led to estimating the uncertainty related to the Doppler effect at ~30–40 kHz. Further optimization of the retro-reflected geometry (size and overlap of the returning beam) allowed for the observation of the Doppler-free features expected for a retro-reflected probe. Figure 3 shows a ^{199}Hg spectrum measured with a probe diameter of 280 μm at $1/e^2$ and a power of 2 mW. Two sharp features can be distinguished at the top of the Doppler profile.

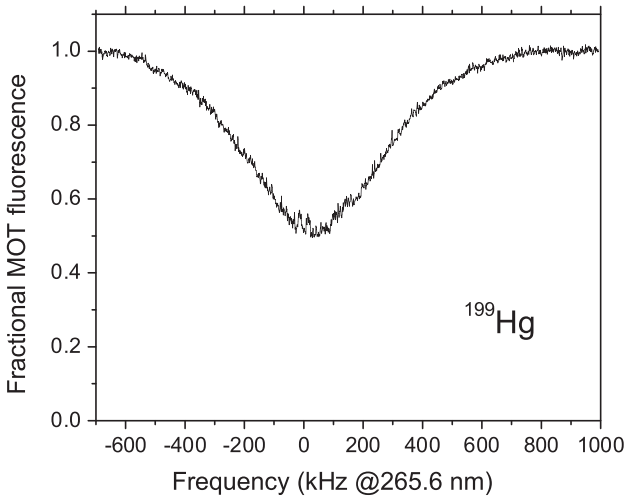

FIG. 3. Spectrum of $^1S_0$-$^3P_0$ transition in ^{199}Hg observed with a retro-reflected probe beam. Sharp Doppler-free features appear at the top of the 580 kHz wide Doppler profile.

The two features, which are better seen on the narrower scans of Fig. 4, are the Doppler-free recoil doublet [22]. The recoil features are shifted by $\pm\nu_{\mathrm{recoil}}$ with respect to the atomic transition frequency ν, where ν_{recoil} is the recoil frequency of the transition equal to $\nu \times (h\nu/2mc^2)$ or 14.2 kHz, where c is the speed of light, h is Planck's constant, and m is the atomic mass. The measured splitting matches $2\nu_{\mathrm{recoil}}$ within the statistical error bar of $\lesssim 1$ kHz.

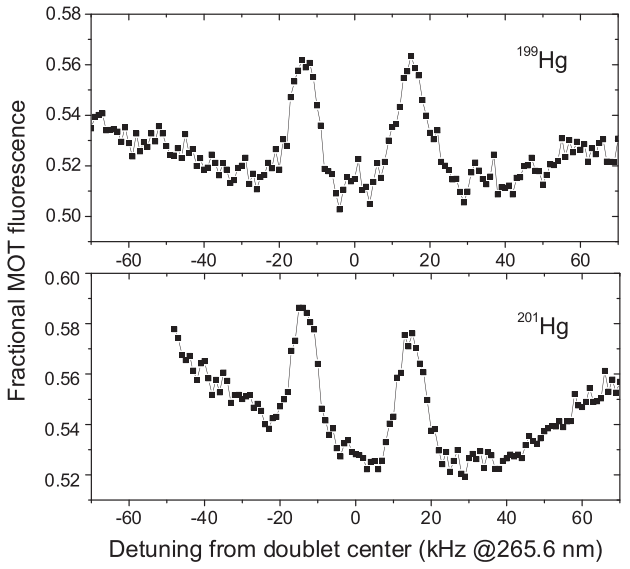

FIG. 4. Recoil doublet observed in the ^{199}Hg (top) and ^{201}Hg (bottom) spectra when a retro-reflected probe beam is used. Data are taken at a rate of one point per second. Spectra have been averaged 4 times.

We have also checked that the center of each component of the recoil doublet is unchanged to less than 1 kHz when the probe time is changed by a factor of 2. Instead, under our experimental conditions, the width of the recoil components is proportional to the interaction time. Indeed, the maximum Rabi frequency that we estimate based on the probe beam power and size, and from the natural linewidth of the clock transition [23] is ~6 kHz. This is smaller than the frequency chirp induced by the fall under the acceleration due to gravity g during the interaction time τ which is $g\tau/\lambda \simeq 18$ kHz for a typical value $\tau = 500$ μs. Note that the recoil doublet was also observed under similar conditions in ^{40}Ca [24]. However, for mercury, the natural linewidth of $^1S_0$-$^3P_0$ transition is 3740 times narrower.

To determine the atomic transition frequency, we take the center of the recoil doublet. An uncertainty equal to the half width at half maximum of the narrowest observed Doppler-free recoil feature is conservatively assigned to this determination. This amounts to a 4.5 kHz uncertainty for both ^{199}Hg and ^{201}Hg. When the MOT field is left on during the probe time, atoms at the edge of the cloud can be exposed to a field of up to 0.2 mT. With the MOT field off, the residual field due to unshielded magnetic sources is ~0.3 mT. A worst case estimation of the shift induced by the first order Zeeman effect in such fields is 3.3 kHz for ^{199}Hg and 2.8 kHz for ^{201}Hg, given the nuclear magnetic moment and the magnetic moment difference between the two clock states [14]. Measurements performed with and without switching off the MOT field agree to within 700 Hz. Ac Stark shift of clock states due to the probe laser is less than 100 Hz. Finally, it is noteworthy that the overall standard deviation of all measurements is less than 1 kHz. The measured frequencies are $\nu(^{199}\mathrm{Hg}) = 1\,128\,575\,290\,808.4 \pm 5.6$ kHz for ^{199}Hg and $\nu(^{201}\mathrm{Hg}) = 1\,128\,569\,561\,139.6 \pm 5.3$ kHz for ^{201}Hg. In fractional terms, the uncertainty is ~5 parts in 10^{12} which improves upon previous indirect determinations [25–27] by more than 4 orders of magnitude. The isotope shift between the two fermionic isotopes is $5\,729\,668.8 \pm 7.7$ kHz. The isotope shift between the best known bosonic isotope ^{198}Hg [25] and ^{199}Hg is $\nu(^{198}\mathrm{Hg}) - \nu(^{199}\mathrm{Hg}) = 699 \pm 12$ MHz with an uncertainty dominated by the ^{198}Hg uncertainty.

To summarize, we have reported the first laser-cooled spectroscopy of $^1S_0$-$^3P_0$ clock transition in fermionic isotopes of mercury. Owing to the observation of the Doppler-free recoil doublet, we have measured the transition frequency with an uncertainty which will make spectroscopy of the clock transition in a lattice trap straightforward. This is an important step towards producing a mercury lattice clock with unprecedented accuracy.

The authors would like to acknowledge support from SYRTE technical services. SYRTE is UMR CNRS 8630 and is associated with UPMC. This work is partly funded by IFRAF and by CNES.

*Also at Instituto de Física de São Carlos, USP-PO Box 369, 13560-970, São Carlos, SP, Brazil.

+Also at National Institute for Laser Physics, Plasmas and Radiation, Plasmas and Nuclear Fusion Laboratory, Bucharest, Magurele, PO Box MG 7, Romania.

[1] T. Rosenband *et al.*, Science **319**, 1808 (2008).
[2] M. M. Boyd *et al.*, Phys. Rev. Lett. **98**, 083002 (2007).
[3] A. D. Ludlow *et al.*, Science **319**, 1805 (2008).
[4] T. Schneider, E. Peik, and C. Tamm, Phys. Rev. Lett. **94**, 230801 (2005).
[5] H. Marion *et al.*, Phys. Rev. Lett. **90**, 150801 (2003).
[6] M. Fischer *et al.*, Phys. Rev. Lett. **92**, 230802 (2004).
[7] S. Blatt *et al.*, Phys. Rev. Lett. **100**, 140801 (2008).
[8] T. M. Fortier *et al.*, Phys. Rev. Lett. **98**, 070801 (2007).
[9] E. Peik *et al.*, Phys. Rev. Lett. **93**, 170801 (2004).
[10] N. Poli *et al.*, Phys. Rev. A **77**, 050501(R) (2008).
[11] S. G. Porsev and A. Derevianko, Phys. Rev. A **74**, 020502 (R) (2006).
[12] V. G. Pal'chikov (private communication).H. Katori *et al.*, *in Proc. of the XIX International Conference on Atomic Physics* (AIP, Rio de Janeiro, Brazil, 2004).
[13] M. Petersen *et al.*, in *Proc. of the 2007 EFTF-FCS Joint Meeting* (IEEE, Geneva, Switzerland, 2007).
[14] H. Hachisu *et al.*, Phys. Rev. Lett. **100**, 053001 (2008).
[15] E. J. Angstmann, V. A. Dzuba, and V. V. Flambaum, Phys. Rev. A **70**, 014102 (2004).
[16] M. Petersen *et al.*, in Proc. of the 62nd Frequency Control Symposium, Honolulu, USA and Proc. of the 22nd European Frequency and Time Forum (IEEE, Toulouse, France, 2008).
[17] J. E Sansonetti and W. C. Martin, Handbook of Basic Atomic Spectroscopic Data, http://physics.nist.gov/PhysRefData/Handbook/index.html.
[18] K. Dieckmann *et al.*, Phys. Rev. A **58**, 3891 (1998).
[19] D. Chambon *et al.*, Rev. Sci. Instrum. **76**, 094704 (2005).
[20] I. Courtillot *et al.*, Phys. Rev. A **68**, 030501(R) (2003).
[21] C. W. Hoyt *et al.*, Phys. Rev. Lett. **95**, 083003 (2005).
[22] J. L. Hall, C. J. Bordé, and K. Uehara, Phys. Rev. Lett. **37**, 1339 (1976).
[23] M. Bigeon, J. Phys. (Orsay, Fr.) **28**, 51 (1967).
[24] T. M. Fortier *et al.*, Phys. Rev. Lett. **97**, 163905 (2006).
[25] E. B. Saloman, J. Phys. Chem. Ref. Data **35**, 1519 (2006).
[26] K. Burns and K. B. Adams, J. Opt. Soc. Am. **42**, 716 (1952).
[27] K. Burns and K. B. Adams, J. Opt. Soc. Am. **42**, 56 (1952).

Bibliography

[Alcock, 1995] Alcock, C. (1995). *Handbook of Chemistry and Physics*, pages 4–121 – 4–122. CRC Press, 76th edition. Edited by David R. Lide.

[Amy-Klein et al., 2005] Amy-Klein, A., Goncharov, A., Guinet, M., Daussy, C., Lopez, O., Shelkovnikov, A., and Chardonnet, C. (2005). Absolute frequency measurement of a sf6 two-photon line by use of a femtosecond optical comb and sum-frequency generation. *Optical Letters*, 30(24):3320–3322.

[Angstmann et al., 2006] Angstmann, E. J., Dzuba, V. A., and Flambaum, V. V. (2006). Frequency shift of hyperfine transitions due to blackbody radiation. *Phys. Rev. A*, 74(023405).

[Arora et al., 2007] Arora, B., Safronova, M. S., and Clark, C. W. (2007). Blackbody-radiation shift in â ^{43}ca^{+} ion optical frequency standard. *Phys. Rev. A*, 76(064501).

[Ashby et al., 2007] Ashby, N., Heavner, T. P., Jefferts, S. R., Parker, T. E., Radnaev, A. G., and Dudin, Y. O. (2007). Testing local position invariance with four cesium-fountain primary frequency standards and four nist hydrogen masers. *Physical Review Letters*, 98(7):070802.

[Bahoura, 1998] Bahoura, M. (1998). *Influence du bruit de phase d'une diode laser sur les performances ultimes de son asservissement en frequence sur une resonance optique*. PhD thesis, l'Université de Paris XI Orsay.

[Baillard et al., 2008] Baillard, X., Fouché, M., Targat, R. L., Westergaard, P., Lecallier, A., Chapelet, F., Abgrall, M., Rovera, G., Laurent, P., Rosenbusch, P., Bize, S., Santarelli1, G., Clairon, A., Lemonde, P.,

Grosche, G., Lipphardt, B., and Schnatz, H. (2008). An optical lattice clock with spin-polarized ^{87}sr atoms. *The European Physical Journal D*, 48:11.

[Baillard et al., 2007] Baillard, X., Fouché, M., Targat, R. L., Westergaard, P. G., Lecallier, A., Coq, Y. L., Rovera, G. D., Bize, S., and Lemonde, P. (2007). Accuracy evaluation of an optical lattice clock with bosonic atoms. *Optics Letters*, 32(13):1812.

[Barber et al., 2006] Barber, Z., Hoyt, C., Oates, C., Hollberg, L., Taichenachev, A., and Yudin, V. I. (2006). Direct excitation of the forbidden clock transition in neutral ^{174}yb atoms confined to an optical lattice. *Phys. Rev. Lett.*, 96(083002).

[Bauch, 2005] Bauch, A. (2005). The ptb primary clocks cs1 and cs2. *Metrologia*, 42(43–54).

[Bauch et al., 1998] Bauch, A., Fischer, B., and Heindorff, T. (1998). Performance of the ptb reconstructed primary clock cs1 and an estimate of its current uncertainty. *Metrologia*, 35(829–845).

[Beloy et al., 2006] Beloy, K., Safronova, U. I., and Derevianko, A. (2006). High-accuracy calculation of the blackbody radiation shift in the ^{1}33cs primary frequency standard. *Phys. Rev. Lett.*, 97(040801).

[Bigeon, 1967] Bigeon, M. C. (1967). Probabilité de transition de la raie $6^1s_0 - 6^3p_0$ du mercure. *Le journal de physique*, 28:51.

[Bitter, 1962] Bitter, F. (1962). Magnetic resonance in radiating or absorbing atoms. *Applied Optics*, 1(1).

[Bize, 2001] Bize, S. (2001). *Tests fondamentaux à l'aide d'horloges à atomes froids de rubidium et de césium*. PhD thesis, l'Université de Paris VI.

[Bize et al., 2005] Bize, S., Laurent, P., Abgrall, M., Marion, H., Maksimovic, I., Cacciapuoti, L., Grünert, J., Vian, C., dos Santos, F. P., Rosenbusch, P., Lemonde, P., Santarelli, G., Wolf, P., Clairon, A., Luiten, A., Tobar, M., and Salomon, C. (2005). Cold atom clocks and applications. *Journal of Physics B: Atomic, Molecular and Optical Physics*, 38:449–468.

[Black, 2001] Black, E. D. (2001). An introduction to pound-drever-hall laser frequency stabilization. *American journal of physics*, 69:79–87.

[Blatt et al., 2008] Blatt, S., Ludlow, A. D., Campbell, G. K., Thomsen, J. W., Zelevinsky, T., Boyd, M. M., Ye, J., Baillard, X., Fouché, M., Targat, R. L., Brusch, A., Lemonde, P., Takamoto, M., Hong, F.-L., Katori, H., and Flambaum, V. V. (2008). New limits on coupling of fundamental constants to gravity using [sup 87]sr optical lattice clocks. *Physical Review Letters*, 100(14):140801.

[Bondu and Debieu, 2007] Bondu, F. and Debieu, O. (2007). Accurate measurement method of fabry-perot cavity parameters via optical transfer function. *Applied Optics*, 46(14):2611.

[Bordé et al., 1984] Bordé, C. J., Salomon, C., Avrillier, S., Lerberghe, A. V., Bréant, C., Bassi, D., and Scoles, G. (1984). Optical ramsey fringes with traveling waves. *Physical review A*, 30(4):1836.

[Boyd et al., 2007] Boyd, M. M., Zelevinsky, T., Ludlow, A. D., Blatt, S., Zanon-Willette, T., Foreman, S. M., and Ye, J. (2007). Nuclear spin effects in optical lattice clocks. *Physical review A*, 76(022510).

[Bransden and Joachain, 1983] Bransden, B. H. and Joachain, C. J. (1983). *Physics of atoms and molecules*. Longman.

[Brusch et al., 2006] Brusch, A., Targat, R. L., Baillard, X., Fouché, M., and Lemonde, P. (2006). Hyperpolarizability effects in a sr optical lattice clock. *Physical review letters*, 96:103003.

[Brush, 2006] Brush, A. (2006). *Horloge á réseau optique á atomes de strontium, et étude des effets d´hyperpolarisabilité dus au pièges laser*. PhD thesis, l'Université de Paris VI.

[Burns and Adams, 1952] Burns, K. and Adams, K. B. (1952). Energy levels and wavelengths of the isotopes of mercury-199 and -200. *Journal of the optical society of America*, 42(716).

[Calonico et al., 2008] Calonico, D., Levi, F., Lorini, L., Calosso, C. E., Bertacco, E. K., Costanzo, G. A., and Godone, A. (2008). New generation of atomic frequency standards at inrim. *Proceedings of the 2008 European Frequency and Time Forum (online)*, (38).

[CGPM, 1969] CGPM (1969). Comptes rendus de la 13e cgpm (1967/68). 103.

[CGPM, 1984] CGPM (1984). Comptes rendus de la 17e cgpm (1983). 97.

[Chambon et al., 2005] Chambon, D., Bize, S., Lours, M., Narbonneau, F., Marion, H., Clairon, A., Santarelli, G., Luiten, A., and Tobar, M. (2005). Design and realization of a flywheel oscillator for advanced time and frequency metrology. *Review of scientific instruments*, 76:094704.

[Chapelet et al., 2007] Chapelet, F., Guena, J., Rovera, D., Laurent, P., Rosenbusch, P., Santarelli, G., Bize, S., Clairon, A., Tobar, M., and Abgrall, M. (2007). Comparisons between 3 fountain clocks at lne-syrte. *Frequency Control Symposium, 2007 Joint with the 21st European Frequency and Time Forum. IEEE International*, pages 467–472.

[Clairon et al., 1991] Clairon, A., Salomon, C., Guellati, S., and Phillips, W. D. (1991). Ramsey resonance in a zacharias fountain. *Europhysics Letters*, 16(2):165–170.

[Condon and Shortley, 1935] Condon, E. U. and Shortley, G. H. (1935). *The Theory of Atomic Spectra*. Cambridge University Press.

[Courtillot et al., 2003] Courtillot, I., Quessada, A., Kovacich, R. P., Brusch, A., Kolker, D., Zondy, J.-J., Rovera, G. D., and Lemonde, P. (2003). Clock transition for a future optical frequency standard with trapped atoms. *Phys. Rev. A*, 68(3):030501.

[Curtis et al., 2008] Curtis, E. A., Barwood, G. P., Ovchinnikov, Y. B., Hill, I. R., and Gill, P. (2008). Development of a neutral strontium lattice trap optical clock at the national physical laboratory. *Proceedings of the 2008 conference on precision electromagnetic measurement digest*, pages 174–175.

[Dehmelt, 1982] Dehmelt, H. G. (1982). Mono-ion oscillator as potential ultimate laser frequency standard. *IEEE Transactions on Instrumentation and Measurement*, 31:83.

[Dicke, 1953] Dicke, R. H. (1953). The effect of collisions upon the doppler width of spectral lines. *Physical Review*, 89(2):472.

[Dieckmann et al., 1998] Dieckmann, K., Spreeuw, R. J. C., Weidemüller, M., and Walraven, J. T. M. (1998). Two-dimensional magneto-optical trap as a source of slow atoms. *Phys. Rev. A*, 58(5):3891–3895.

[Drever et al., 1983] Drever, R. W. P., Hall, J. L., Kowalski, F. V., Hough, J., Ford, G. M., Munley, A. J., and Ward, H. (1983). Laser phase and frequency stabilization using an optical resonator. *Applied physics B*, 31:93–105.

[Essen and Parry, 1957] Essen, L. and Parry, J. V. L. (1957). The caesium resonator as a standard of frequency and time. *Philosophical Transactions of the Royal Society of London*, 250:45–69.

[Fisk, 1997] Fisk, P. T. H. (1997). Trapped-ion and trapped-atom microwave frequency standards. *Reports on progress in physics*, 60:761–817.

[Friebe et al., 2008] Friebe, J., Pape, A., Riedmann, M., Moldenhauer, K., Mehlstäubler, T., Rehbein, N., Lisdat, C., Rasel, E. M., Ertmer, W., Schnatz, H., Lipphardt, B., and Grosche, G. (2008). Absolute frequency measurement of the magnesium intercombination transition [sup 1]s[sub 0] –¿[sup 3]p[sub 1]. *Physical Review A (Atomic, Molecular, and Optical Physics)*, 78(3):033830.

[Giacomo, 1984] Giacomo, P. (1984). News from the bipm. *Metrologia*, 20(1):25.

[Gibble et al., 1992] Gibble, K. E., Kasapi, S., and Chu, S. (1992). Improved magneto-optic trapping in a vapor cell. *Optics Letters*, 17(7).

[Guéna et al., 2007] Guéna, J., Dudle, G., and Thomann, P. (2007). An experimental study of intermodulation effects in an atomic fountain frequency standard. *The European Physical Journal Applied Physics*, 388(183–189).

[Hachisu et al., 2008] Hachisu, H., Miyagishi, K., Porsev, S. G., Derevianko, A., Ovsiannikov, V. D., Palćhikov, V. G., Takamoto, M., and Katori, H. (2008). Trapping of neutral mercury atoms and prospects for optical lattice clocks. *Phys. Rev. Lett.*, 100(053001).

[Hahn and Radecki, 1987] Hahn, S. L. and Radecki, K. W. (1987). Design of an optically pumped silver atomic beam frequency standard. *IEEE Transactions on Instrumentation and Measurement*, 36(2):639.

[Halford, 1971] Halford, D. (1971). Infrared-microwave frequency synthesis design: Some relevant conceptual noise aspects. *Proceedings of the Frequency Standards and Metrology Seminar, Quebec*, pages 431–466.

[Hall et al., 1976] Hall, J. L., Bordé, C. J., and Uehara, K. (1976). Direct optical resolution of the recoil effect using saturated absorption spectroscopy. *Phys. Rev. Lett.*, 37(20):1339–1342.

[Hänsch and Couillaud, 1980] Hänsch, T. and Couillaud, B. (1980). Laser frequency stabilization by polarization spectroscopy of a reflecting reference cavity. *Optics Communications*, 35(3):441.

[Hänsch, 2006] Hänsch, T. W. (2006). Nobel lecture: Passion for precision. *Reviews of Modern Physics*, 78(4):1297.

[Hansen et al., 2008] Hansen, P. L., Therkildsen, K. T., Malossi, N., Jensen, B. B., van Ooijen, E. D., Brusch, A., Müller, J. H., Hald, J., and Thomsen, J. W. (2008). Measurement of the 3s3p [sup 3]p[sub 1] lifetime in magnesium using a magneto-optical trap. *Physical Review A (Atomic, Molecular, and Optical Physics)*, 77(6):062502.

[Hosaka et al., 2005] Hosaka, K., Webster, S. A., Blythe, P. J., Stannard, A., Beaton, D., Margolis, H. S., Lea, S. N., and Gill, P. (2005). An optical frequency standard based on the electric octupole transition in $^{171}\mathrm{yb}^{+}$. *IEEE Transactions on Instrumentation and Measurement*, 54(2):759.

[Itano et al., 1982] Itano, W. M., Lewis, L. L., and Wineland, D. J. (1982). Shift of $s122$ hyperfine splittings due to blackbody radiation. *Phys. Rev. A*, 25(2):1233–1235.

[Jackson, 1999] Jackson, J. D. (1999). *Classical Electrodynamics*. John Wiley & Sons, inc., 3rd edition.

[Jefferts et al., 2007] Jefferts, S. R., Heavner, T. P., Parker, T. E., and Shirley, J. H. (2007). Nist cesium fountains - current status and future prospects. *Proceedings of 2007 SPIE Conference*, 6673:9.

[Jones et al., 2000] Jones, D. J., Diddams, S. A., Ranka, J. K., Stentz, A., Windeler, R. S., Hall, J. L., and Cundiff, S. T. (2000). Carrier-envelope phase control of femtosecond mode-locked lasers and direct optical frequency synthesis. *Science*, 288:635.

[Kasevich et al., 1989] Kasevich, M. A., Riis, E., Chu, S., and DeVoe, R. G. (1989). Rf spectroscopy in an atomic fountain. *Physical review letters*, 63(6).

[Katori, 2002] Katori, H. (2002). Spectroscopy of strontium atoms in the lamb-dicke confinement. *Proceedings of the 6th Symposium on Frequency Standards and Metrology, 2001*, pages 323–330. Edited by P. Gill.

[Katori et al., 2004] Katori, H., Takamoto, M., Kishimoto, T., Fujiki, J., Higashi, R., and Yasuda, M. (2004). Engineering stark potentials for precision measurements: Optical lattice clock and electrodynamic surface trap. *Proceedings of the XIX International Conference on Atomic Physics*, pages 112–122.

[Katori et al., 2003] Katori, H., Takamoto, M., Palćhikov, V. G., and Ovsiannikov, V. D. (2003). Ultrastable optical clock with neutral atoms in an engineered light shift trap. *Physical review letters*, 91(17).

[Kramer et al., 1988] Kramer, G., Weiss, C. O., and Lipphardt, B. (1988). Coherent frequency measurements of the hfs-resolved methane line. *Proceedings of the 4th Frequency Standards and Metrology Symposium*, page 181.

[Lehmann and Barbé, 1963] Lehmann, J.-C. and Barbé, R. (1963). Measure du rapport des moments magnétiques nucleares de ^{199}hg et ^{201}hg. *C.R.Acad.Sc.*, 257:3152.

[Lemonde and Wolf, 2005] Lemonde, P. and Wolf, P. (2005). Optical lattice clock with atoms confined in a shallow trap. *Physical review A*, 72:033409.

[Levi et al., 2004] Levi, F., Lorini, L., Calonico, D., and Godone, A. (2004). Ien-csf1 accuracy evaluation and two-way frequency comparison. *IEEE Transactions on Ultrasonics, Ferroelectrics, and Frequency Control*, 51(10):1216.

[Lide, 1995] Lide, D. R., editor (1995). *CRC Handbook of Chemistry and Physics*. CRC Press.

[Ludlow et al., 2006] Ludlow, A. D., Boyd, M. M., Zelevinsky, T., Foreman, S. M., Blatt, S., Notcutt, M., Ido, T., and Ye, J. (2006). Systematic study of the ^{8}7sr clock transition in an optical lattice. *Phys. Rev. Lett.*, 96(033003).

[Ludlow et al., 2007] Ludlow, A. D., Huang, X., Notcutt, M., Zanon-Willette, T., Foreman, S. M., Boyd, M. M., Blatt, S., and Ye, J. (2007). Compact, thermal-noise-limited optical cavity for diode laser stabilization at 1x10^{-15}. *Optical letters*, 32:641.

[Ludlow et al., 2008] Ludlow, A. D., Zelevinsky, T., Campbell, G. K., Blatt, S., Boyd, M. M., de Miranda, M. H. G., Martin, M. J., Thomsen, J. W., Foreman, S. M., Ye, J., Fortier, T. M., Stalnaker, J. E., Diddams, S. A., Coq, Y. L., Barber, Z. W., Poli, N., Lemke, N. D., Beck, K. M., and Oates, C. W. (2008). Sr lattice clock at 1 x 10^{-16} fractional uncertainty by remote optical evaluation with a ca clock. *Science*, 319:1805.

[Lurio et al., 1962] Lurio, A., Mandel, M., and Novick, R. (1962). Second-order hyperfine and zeeman corrections for an (sl) configuration. *Physical Review*, 126:1758.

[Makdissi and de Clercq, 2001] Makdissi, A. and de Clercq, E. (2001). Evaluation of the accuracy of the optically pumped caesium beam primary frequency standard of the bnm-lptf. *Metrologia*, 38:400–425.

[Margolis et al., 2004] Margolis, H. S., Barwood, G. P., Huang, G., Klein, H. A., Lea, S. N., Szymaniec, K., and Gill, P. (2004). Hertz-level measurement of the optical clock frequency in a single $^{88}sr^{+}$ ion. *Science*, 306:1355.

[Marion et al.,] Marion, H., Pereira Dos Santos, F., Abgrall, M., Zhang, S., Sortais, Y., Bize, S., Maksimovic, I., Calonico, D., Grünert, J., Mandache, C., Lemonde, P., Santarelli, G., Laurent, P., Clairon, A., and Salomon, C. Search for variations of fundamental constants using atomic fountain clocks. *Phys. Rev. Lett.*, 90(15):150801.

[Markowitz et al., 1958] Markowitz, W., Hall, R. G., Essen, L., and Parry, J. V. L. (1958). Frequency of cesium in terms of ephemeris time. *Physical review letters*, 1(3).

[Metcalf and van der Straten, 1999] Metcalf, H. J. and van der Straten, P. (1999). *Laser Cooling and Trapping*. Springer-Verlag.

[Millo et al., 2008] Millo, J., Dawkins, S., Chicireanu, R., Magalhães, D. V., Mandache, C., Holleville, D., Lours, M., Bize, S., and Santarelli, G.

(2008). Ultra-stable optical cavities: Design and experiements at lne-syrte. *EFTF 2008 proceedings.*

[Mitroy et al., 2008] Mitroy, J., Zhang, J. Y., and Bromley, M. W. J. (2008). Long-range interactions of the sr^+ ion. *Phys. Rev. A*, 77:032512.

[Morinaga et al., 1989] Morinaga, A., Riehle, F., Ishikawa, J., and Helmcke, J. (1989). A ca optical frequency standard: Frequency stabilization by means of nonlinear ramsey resonances. *Applied Physics B*, 48:165–171.

[NIST, 2008] NIST (2008). http://physics.nist.gov/physrefdata /handbook/tables/mercurytable1.htm.

[Numata et al., 2004] Numata, K., Kemery, A., and Camp, J. (2004). Thermal-noise limit in the frequency stabilization of lasers with rigid cavities. *Physical Review Letters*, 93(250602).

[Park and Yoon, 2003] Park, C. Y. and Yoon, T. H. (2003). Efficient magneto-optical trapping of yb atoms with a violet laser diode. *Physical review A*, (68):055401.

[Petersen et al., 2008] Petersen, M., Millo, J., Magalhães, D. V., Mandache, C., Dawkins, S. T., Chicireanu, R., Lecoq, Y., Acef, O., Santarelli, G., Clairon, A., and Bize, S. (2008). Magneto-optical trap of neutral mercury for an optical lattice clock. *Proceedings of the 2008 European Frequency and Time Forum*, (143).

[Poitzsch et al., 1996] Poitzsch, M. E., Bergquist, J. C., Itano, W. M., and Wineland, D. J. (1996). Cryogenic linear ion trap for accurate spectroscopy. *Review of Scientific Instruments*, 67:129–134.

[Poli et al., 2008] Poli, N., Barber, Z. W., Lemke, N. D., Oates, C. W., Ma, L. S., Stalnaker, J. E., Fortier, T. M., Diddams, S. A., Hollberg, L., Bergquist, J. C., Brusch, A., Jefferts, S., Heavner, T., and Parker, T. (2008). Frequency evaluation of the doubly forbidden $^1s_0 \rightarrow {}^3p_0$ transition in bosonic ^{174}yb. *Physical review A*, (77):050501.

[Poli et al., 2007] Poli, N., Drullinger, R. E., Tarallo, M. G., Tino, G. M., and Prevedelli, M. (2007). Strontium optical lattice clock with all semiconductor sources. *Frequency Control Symposium, 2007 Joint with the 21st European Frequency and Time Forum. IEEE International*, pages 655–658.

[Porsev and Derevianko, 2006] Porsev, S. G. and Derevianko, A. (2006). Multipolar theory of blackbody radiation shift of atomic energy levels and its implications for optical lattice clocks. *Phys. Rev. A*, 74(020502).

[Porsev et al., 2004] Porsev, S. G., Derevianko, A., and Fortson, E. N. (2004). Possibility of an optical clock using the $61s \rightarrow 63po$ transition in $171, 173yb$ atoms held in an optical lattice. *Phys. Rev. A*, 69(2):021403.

[Radzig and Smirnov, 1985] Radzig, A. A. and Smirnov, B. M. (1985). *Reference Data on Atoms, Molecules, and Ions*. Springer-Verlag.

[Ramsey, 1950] Ramsey, N. F. (1950). A molecular beam resonance method with separated oscillating fields. *Physical Review*, 78(695).

[Ramsey, 1985] Ramsey, N. F. (1985). *Molecular Beams*. Oxford University Press. Paperback edition.

[Rathmann et al., 1968] Rathmann, C. L., Mann, G. H., and Nordberg, M. E. (1968). A new ultralow-expansion, modified fused-silica glass. *Applied Optice*, 7(5):819.

[Riehle et al., 2008] Riehle, F., Vellore, W., Raaj, J. S., Legero, T., Lisdat, C., and Sterr, U. (2008). Spectroscopy of 88sr in an optical lattice for an optical clock. *Proceedings of Modern Problems of Laser Physics, Novosibirsk, 24–30, August, 2008, Russia.*

[Rosenband et al., 2008] Rosenband, T., Hume, D. B., Schmidt, P. O., Chou, C. W., Brusch, A., Lorini, L., Oskay, W. H., Drullinger, R. E., Fortier, T. M., Stalnaker, J. E., Diddams, S. A., Swann, W. C., Newbury, N. R., Itano, W. M., Wineland, D. J., and Bergquist, J. C. (2008). Frequency ratio of al^+ and hg^+ single-ion optical clocks; metrology at the 17th decimal place. *Science*, 319:1808.

[Rosenband et al., 2006] Rosenband, T., Itano, W. M., Schmidt, P. O., Hume, D. B., Koelemeij, J. C. J., Bergquist, J. C., and Wineland, D. J. (2006). Blackbody radiation shift of the $^{27}al^+$ $^1s_0 \rightarrow {}^3p_0$ transition. *ArXiv*, (0611125). arXiv:physics/0611125v2 [physics.atom-ph] (http://arxiv.org/abs/physics/0611125v2).

[Saloman, 2006] Saloman, E. B. (2006). Wavelengths, energy level classifications, and energy levels for the spectrum of neutral mercury. *Journal of Physical and Chemical Reference Data*, 35:1519.

[Santarelli et al., 1998] Santarelli, G., Audoin, C., Makdissi, A., Laurent, P., Dick, G. J., and Clairon, A. (1998). Frequency stability degradation of an oscillator slaved to a periodically interrogated atomic resonator. *IEEE Transactions on Ultrasonics, Ferroelectrics, and Frequency Control*, 45(4):887.

[Santra et al., 2004] Santra, R., Christ, K. V., and Greene, C. H. (2004). Properties of metastable alkaline-earth-metal atoms calculated using an accurate effective core potential. *Physical Review A*, 69:042510.

[Scheid et al., 2007] Scheid, M., Markert, F., Walz, J., Wang, J., Kirchner, M., and Hänsch, T. W. (2007). 750 mw continuous-wave solid-state deep ultraviolet laser source at the 253.7 nm transition in mercury. *Optics Letters*, 32(8):955–957.

[Schmidt et al., 2005] Schmidt, P. O., Rosenband, T., Langer, C., Itano, W. M., Bergquist, J. C., and Wineland, D. J. (2005). Spectroscopy using quantum logic. *Science*, 309:749.

[Schneider et al., 2005] Schneider, T., Peik, E., and Tamm, C. (2005). Sub-hertz optical frequency comparisons between two trapped [sup 171]yb[sup +] ions. *Physical Review Letters*, 94(23):230801.

[Shirley et al., 2001] Shirley, J. H., Lee, W. D., and Drullinger, R. E. (2001). Accuracy evaluation of the primary frequency standard nist-7. *Metrologia*, 38(5):427–458.

[Simon et al., 1998] Simon, E., Laurent, P., and Clairon, A. (1998). Measurement of the stark shift of the cs hyperfine splitting in an atomic fountain. *Phys. Rev. A*, 57(1):436–439.

[Sobelman, 1992] Sobelman, I. I. (1992). *Atomic Spectra and Radiative Transitions*. Springer-Verlag, 2nd edition.

[Szymaniec et al., 2005] Szymaniec, K., Chalupczak, W., Whibberley, P. B., Lea, S. N., and Henderson, D. (2005). Evaluation of the primary frequency standard npl-csf1. *Metrologia*, 42:49–57.

[Taichenachev et al., 2006] Taichenachev, A. V., Yudin, V. I., Oates, C. W., Hoyt, C. W., Barber, Z. W., and Hollberg, L. (2006). Magnetic field-induced spectroscopy of forbidden optical transitions with application to lattice-based optical atomic clocks. *Physical Review Letters*, 96:083001.

[Takamoto et al., 2005] Takamoto, M., Hong, F.-L., Higashi, R., and Katori, H. (2005). An optical lattice clock. *Nature*, 435:321.

[Terrien, 1968] Terrien, J. (1968). News from the international bureau of weights and measures. *Metrologia*, 4(1):43.

[Udem et al., 1999] Udem, T., Reichert, J., Holzwarth, R., and Hänsch, T. W. (1999). Absolute optical frequency measurement of the cesium $d1$ line with a mode-locked laser. *Phys. Rev. Lett.*, 82(18):3568–3571.

[Vanier and Audoin, 1989] Vanier, J. and Audoin, C. (1989). *The Quantum Physics of Atomic Standards*. IOP publishing.

[Vessot et al., 1980] Vessot, R. F. C., Levine, M. W., Mattison, E. M., Blomberg, E. L., Hoffman, T. E., Nystrom, G. U., Farrel, B. F., Decher, R., Eby, P. B., Baugher, C. R., Watts, J. W., Teuber, D. L., and Wills, F. D. (1980). Test of relativistic gravitation with a space-borne hydrogen maser. *Phys. Rev. Lett.*, 45(26):2081–2084.

[von Zanthier et al., 2000] von Zanthier, J., Becker, T., Eichenseer, M., Nevsky, A. Y., Schwedes, C., Peik, E., Walther, H., Holzwarth, R., Reichert, J., Udem, T., Hänsch, T. W., Pokasov, V., Skvortsov, M. N., and Bagayev, S. N. (2000). Absolute frequency measurement of the in^+ clock transition with a mode-locked laser. *Optics Letters*, 25(23):1729.

[Wohlleben et al., 2001] Wohlleben, W., Chevy, F., Madison, K., and Dalibard, J. (2001). An atom faucet. *The European Physical Journal D*, 15:237–244.

[Wolf et al., 2006] Wolf, P., Chapelet, F., Bize, S., and Clairon, A. (2006). Cold atom clock test of lorentz invariance in the matter sector. *Physical Review Letters*, 96(6):060801.

[Yasuda et al., 2007] Yasuda, M., Hong, F. L., Kohno, T., Kurosu, T., Onae, A., and Katori, H. (2007). Present status of the development of the yb optical lattice clock at nmij/aist. *IEEE/LEOS Summer Topical Meetings, 2008 Digest*, pages 145–146.

[Ye et al., 2003] Ye, J., Peng, J.-L., Jones, R. J., Holman, K. W., Hall, J. L., Jones, D. J., Diddams, S. A., Kitching, J., Bize, S., Bergquist, J. C., Hollberg, L. W., Robertsson, L., and Ma, L.-S. (2003). Delivery of

high-stability optical and microwave frequency standards over an optical fiber network. *Journal of Optical Society of America*, (1459).

[Young et al., 1999a] Young, B. C., Cruz, F. C., Itano, W. M., and Bergquist, J. C. (1999a). Visible lasers with subhertz linewidths. *Phys. Rev. Lett.*, 82(19):3799–3802.

[Young et al., 1999b] Young, B. C., Rafac, R. J., Beall, J. A., F. C. Cruz, W. M. I., Wineland, D. J., and Bergquist, J. C. (1999b). Hg^+ optical frequency standard: Recent progress. *ICOLS proceedings*, (61–70).